Synthesis and Characterization of Few Walled Carbon Nanotubes and Studies for Gas Sensor Applications

By

R KAMALA KANNAN

PHYS02200704002

Indira Gandhi Centre for Atomic Research
Kalpakkam-603 102
Tamil Nadu, India

A thesis submitted to the

Board of Studies in Physical Sciences

In partial fulfillment of requirements

For the Degree of

DOCTOR OF PHILOSOPHY

of

HOMI BHABHA NATIONAL INSTITUTE

July, 2012

Homi Bhabha National Institute

Recommendations of the Viva Voce Board

As members of the Viva Voce Board, we certify that we have read the dissertation prepared by **R KAMALA KANNAN** entitled "**Synthesis and Characterization of Few Walled Carbon Nanotubes and Studies for Gas Sensor Applications"** and recommend that it may be accepted as fulfilling the dissertation requirement for the Degree of Doctor of Philosophy.

_____ Date:
Chairman - Dr. Sitaram Dash

_____ Date:
Guide / Convener - Dr. A. K. Tyagi

_____ Date:
Member - Dr. B. V. R. Tata

_____ Date:
Member – Dr. Saroja Sai Baba

_____ Date:
Member – Dr. M. Kamruddin

_____ Date:
External Examiner

Final approval and acceptance of this dissertation is contingent upon the candidate's submission of the final copies of the dissertation to HBNI.

CERTIFICATE

I hereby certify that I have read this dissertation prepared under my direction and recommend that it may be accepted as fulfilling the dissertation requirement.

_____ Date:

Dr. A. K. Tyagi

.

STATEMENT BY AUTHOR

This dissertation has been submitted in partial fulfillment of requirements for an advanced degree at Homi Bhabha National Institute (HBNI) and is deposited in the Library to be made available to borrowers under rules of the HBNI.

Brief quotations from this dissertation are allowable without special permission, provided that accurate acknowledgement of source is made. Requests for permission for extended quotation from or reproduction of this manuscript in whole or in part may be granted by the Competent Authority of HBNI when in his or her judgment the proposed use of the material is in the interests of scholarship. In all other instances, however, permission must be obtained from the author.

R KAMALAKANNAN

DECLARATION

I, hereby declare that the investigation presented in the thesis has been carried out by me. The work is original and has not been submitted earlier as a whole or in part for a degree / diploma at this or any other Institution / University.

R KAMALAKANNAN

THIS THESIS IS DEDICATED TO MY
BELOVED
PARENTS AND SISTERS

ACKNOWLEDGEMENTS

I sincerely acknowledge Dr A K Tyagi and Dr. M Kamruddin under whose guidance and constant support the present work has been carried out and could be completed successfully.

I am deeply grateful to Dr. Ilango for his care, encouragement and valuable suggestions during the tenure of my thesis work.

I thank my lab members who are always with me during professional and personal issues and sustaining the pleasant ambient around me. I learned the fine aspects of the research work in various stages of my thesis work from Mr. Ajikumar, Mr. P A Manoj Kumar and Dr. K Ganesan. I have had a pleasure to work with Dr. Mangamma, Dr. Ramanatha Swamy, Mr. Syamala Rao, Mr. M. Suresh and Mr. Subrata Gosh.

I thank the project colleagues Ms. Priyadharsini, Ms. K Aruna, Ms. S Karthika and Ms. Venkateswari with whom I learned the research work.

I would like to thank all mentors, colleagues of MSG for providing constant support and assistance in experiments and technical discussion. My heartfelt thank to friends and enclave members without whom I wouldn’t have crossed the difficult moments of Ph.D life.

I am very much thankful to the Department of Atomic Energy for providing financial assistance during my Ph.D tenure. I thank Dr. Baldev Raj the former Director of IGCAR for permitting me to pursue research at this premier centre. I am thankful to Dr. M. Sai Baba for his kind advices and for making my stay enjoyable in the enclave.

This work could not have been fulfilled without the encouragement, concern, care and perseverance of my parents, sisters and well-wishers in my extended family.

Contents

Synopsis

Carbon nanotubes (CNTs) have evolved as a technologically important material over many years. The exotic properties exhibited by this nano-material kindled the interest of scientists and engineers to explore their bizarre physical properties and in turn to exploit them for novel applications.

CNTs are one dimensional hollow nanostructure made up of hexagonal rings of carbon atoms, with fullerene capped ends. CNTs can exist as a single tube known as a single walled CNT (SWCNT) or in the form of concentric tubes known as multiwalled CNTs (MWCNTs). The structure is one dimensional with axial symmetry exhibiting a spiral conformation called chairality. The quantum mechanical confinement of electrons around the circumference of the tube determines the metallic or semiconducting nature of the CNT. Irrespective of the chirality, the number of modes available for conduction of electrons governs the transport properties that strongly depend on tube diameter. In view of this, researchers have embarked on the study of few walled CNTs (FWCNTs), a special type of small diameter MWCNT with superb structural perfection. A FWCNT consists of few layers of tubes and have diameter less than 10 nm.

This thesis focuses on synthesis, characterization and applications of CNTs as gas sensors. The choice of FWCNTs in the current study is due to its unique features. A FWCNT has a narrow band gap and is easy to synthesize and scale up compared to SWCNTs. High structural stability under large current flow and a protected inner wall from chemical modifications are important consideration for attractive technological applications. A combination of these properties ensures reduction in failure of electronic devices, compatibility to functionalization and decoration without affecting the integrity of the tubes. In this thesis, we have adapted a comprehensive approach to

understand this wonderful material by going through the three important steps; synthesis, characterization and application.

In essence, this thesis investigates the CNT growth process by CVD using two catalytic support materials using a home built TGA-MS system. An extensive characterization process using SEM, TEM, Raman and FTIR spectra to characterize their physical and chemical nature was undertaken. The electrical transport properties of the CNT network were studied to understand the conduction mechanism collectively determined by the constituent entities that may belong to either metallic or semiconducting materials. This thesis also attempts to address, the impact of structural defects in the electronic transport properties. This is an important study in the context of devices and sensors based on CNTs

Gas sensors based on CNTs are found to respond to a variety of gases like NO_2, N_2O, CH_4, NH_3, H_2 and ethanol. However, their poor response and lack of ability to distinguish among gases leaves these sensors barely usable. This motivates functionalization of CNT to realize hybrid material with enhanced properties as gas sensing hybrid material. FWCNT based SnO_2 and Pd decorated hybrid materials were synthesized and their response to gases has been evaluated. While the former was tested for its selective detection based on temperature for ammonia and ethanol, the later was found to show better response, than bare CNTs even at room temperature, in the detection of H_2. The sensors are devised by spin coating on an interdigted electrode with a hybrid material of choice. In addition, the field emission properties were also studied and analyzed using the F-N equation.

The thesis is organized into seven chapters and covers topics on synthesis of CNTs, structural studies, transport properties and their applications as a gas sensor. The details of the chapters are as given below:

Chapter-1 introduces the basic concepts on the nomenclature of CNTs and gives a necessary literature survey relevant to this thesis.

Chapter-2 provides the details on the in-house developed CVD setup for CNT synthesis and the gas sensor test station. The salient feature of these setups and limitations are discussed in detail.

Chapter-3 gives a brief description on analytical techniques as well as the equipment/techniques related to characterization of CNTs.

Chapter-4 deals with the synthesis of FWCNTs, MWCNTs and B-CNTs with varying template, catalyst and catalyst combination using methane as carbon source. The purification of Fe-Mo/MgO grown few walled CNTs was studied . TGA was used as a primary characterization technique.

Chapter-5 is divided into two parts, wherein the first part deals with optical properties of the CNTs using Raman and FTIR studies. In addition, the structural properties and intercalation into the CNTs walls are also discussed. In the second part of this chapter transport properties of the CNT random network is studied. The effect of structural defects on the transport property is explained and the conduction mechanism is modeled using a combination of FIT and VRH mechanisms.

Chapter-6 discusses the properties of gas sensors based on a FWCNT random network. This chapter also deals with Pd and SnO_2 decorated FWCNTs for gas sensing properties. Furthermore, sensors were studied for their temperature dependent transport properties and I-V characteristics to understand their field dependent sensing properties.

Chapter-7 summarizes the important results and conclusions. A brief outline on the future scope of the work is also discussed.

List of figures

List of Tables

Chapter-1 Introduction

1.1 Introduction

Studies on nano-materials have been considered as a significant field of interest in material science for the past two decades. Nanoscience and nanotechnology has developed over these years for manufacturing nanomaterials for novel applications. Today, nanoscience and nanotechnology constitute very active and promising multidisciplinary research areas, bridging scientists and engineers in several fields like physics, chemistry, materials science, electronics, biology and medicine. Herein, carbon nanotubes (CNTs) are an intriguing new class of nanomaterials with extraordinary electrical properties originating from their quasi 1-dimensional structure. The dimensions of the nanotubes are of the order of the Fermi wavelength of the electrons and hence this object can be viewed as a quantum mechanical entity that obeys the rules of quantum mechanics. These microscopic features of atomic arrangement in CNTs manifest in novel structural and electronic properties that are completely different from their bulk properties. These novel properties can be harnessed in potential applications such as in room temperature gas sensing, low resistance metal interconnects, optically transparent conducting films for displays, high surface area catalytic supports, etc. However, exploration of this material for applications to revolutionize our day to day life requires intense research in bridging the gaps in understanding of their synthesis and characterization at an industrial scale. This motivates the current study to address some of the specific aspect in CNT synthesis, transport properties and applications in gas sensors.

Carbon is one of the most interesting materials that display a wide variation in its properties depending on the atomic arrangements giving rise to different allotropes.

Carbon has six electrons that and occupy the $1s^2$, $2s^2$ and $2p^2$orbitals of. The core $1s^2$ electrons are strongly bound whilst the remaining weakly bound four valence electrons are able to quantum mechanically `mix' through orbital hybridization to generate sp^1, sp^2 and sp^3 bonds. In ambient conditions graphite and diamond are the well known thermodynamically stable forms of carbon allotropes. The advent of electron microscopy has made it possible to observe other novel carbon allotropes, such as hexagonal diamond, nano-diamond, carbon-foams, fullerenes, nanowires and nanotubes.

1.1.1 Historical development of Carbon nanotubes

Carbon filaments, now believed to be nanotubes, were first observed by Radushkevich and Lukyanovich in 1952 [1]. Subsequently in the year 1958, Hillert and Lange [2] reported the concentric and bamboo textures of carbon filaments. Later in 1960 Bollmann and Spreadborough [3] demonstrated the synthesis of a rolled graphite sheet. Followed by these discoveries, Oberlin et al. [4] reported in 1976 the chemical vapor deposition (CVD) growth of carbon nanofibers (CNFs) by benzene decomposition. Fullerenes were discovered by Kroto et al. in 1985 [5]. The most famous of this class of molecules is the spherical Buckyball C60, having an atomic structure similar to a soccer ball connecting 12 heptagonal and 20 hexagonal leather patches. After this discovery, it became evident that sp^2-hybridized graphene layers exist not only in planar honeycomb sheets like graphite but also in spherically curved and closed cages. Later, in 1991, Sumio Iijima synthesized and studied a cylindrical form of the buckyball, known as a carbon nanotube. He reported double-walled carbon nanotubes (DWCNTs) and multiwalled carbon nanotubes (MWCNTs) [6] and explained their crystal structures. Two years later SWCNTs were independently synthesized by Iijima and Ichihashi [7] and Bethune et al [8]. Following by these mile

Property	Comparison
Carrier mobility: 79000 cm^2/Vs (at RT) [9]	> Hole mobility in Si
Maximum electrical current density: > 10^9 A/cm^2 [10]	100 times greater than copper wires
Thermal conductivity: 6600 W m^{-1} K^{-1} [11]	> Diamond
Tensile strength: 150 GPa [12]	100 times the strength of steel
Young's modulus: 1 TPa [13]	> Diamond

Table 1.1: Comparison of exotic properties of CNTs

stone discoveries, their extraordinary properties (table-1.1) were harnessed to give a wide range of practical applications including their use as chemical sensors [14-16], in hydrogen storage [17], in field emission materials [18], catalyst supports [19], in electronic devices [20], and as nanotweezers [21]. Today many variants of CNT and related structures are studied and being reported in detail. A brief discussion of CNTs follows.

1.1.2 Carbon nanotubes and related structures

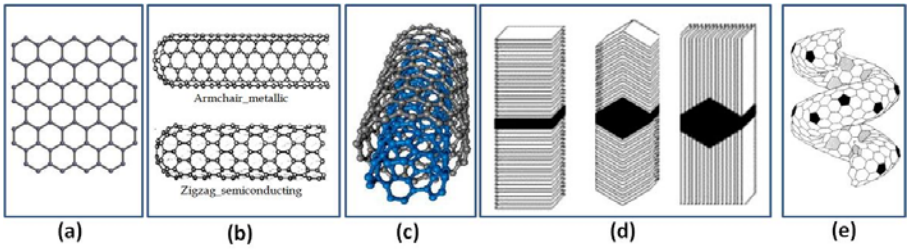

Figure 1.1: carbon nanostructure (a) graphene, (b) SWCNT, (c) MWCNT, (d) platelet, fishbone & ribbon nanofibers and (e) helical CNT [22-24].

A carbon nanotube can be described as a strip of graphene sheet that is rolled into a seamless cylinder and capped with half a buckyball at both ends. The sidewall of the SWCNTs consists of sp^2 hybridized carbon atoms that exhibit similar bonding and structure as graphite. Broadly, carbon nanotubes can be divided into two

categories according to the number of layers of graphene sheets present in a carbon nanotube. SWCNTs are made up of a single layer of carbon atoms while MWCNTs consist of concentric tubes wrapped one inside another. Apart from these two divisions there is a special type of small diameter MWCNT, such as Few-Walled carbon nanotube (FWCNT), which contains a few layers of graphene sheets and with a diameter below 10 nm. FWCNTs have acquired great importance due to their unique structures and distinguished properties compared to either SWCNTs or larger diameter MWCNTs [25-27]

Apart from cylindrical CNTs, other geometrical arrangements of graphite sheets have also been reported (fig.-1.1) [22-24]. For example, in a fishbone nanofiber the graphite sheets are stacked at an angle to the fiber axis. In a platelet nanofiber the graphite sheets are perpendicular to the fiber axis. Curvature created by introduction of pentagonal and heptagonal (5-7) defects in the graphene lattice produces a new class of CNTs named as helical CNT and spiral CNT. All these carbonaceous materials have very different properties owing to their different geometrical structures.

1.1.3 Geometrical structure of CNTs

The properties of CNTs are determined by their atomic structures. Each SWCNT or a single layer of MWCNTs is specified by the chiral vector C_h, as shown in fig.-1.2a,

$$C_h = n_{a1} + m_{a2} \equiv (n, m) \tag{1.1}$$

This is often described by the pair of indices (n, m) which denote the number of unit vectors n_{a1} and m_{a2} in the hexagonal honeycomb lattice of a 2-D graphene sheet contained in the vector C_h. As shown in fig.-1.1, the chiral angle θ, made by the chiral vector C_h, is given by

$$\theta = \tan^{-1}\left[{}^{3m}/_{(m+2n)}\right] \qquad (1.2)$$

For θ equal to 0^o, 30^o and $0<\theta<30^o$ the nanotubes are called zigzag, armchair and chiral, respectively. The nanotube diameter d can be determined by (n,m) as

$$d = {}^{|C_h|}/_{\pi} = \sqrt{\left[\ 3a_{C-C}\ (m^2 + mn + n^2)^{1/2}/_{\pi}\right]} \qquad (1.3)$$

where, $a_{C\text{-}C}$ is the nearest-neighbor C-C distance (1.421 Å in graphite), and $|C_h|$ is the length of the chiral vector C_h.

The curvature in the CNTs leads to strain in the lattice. Hence, an increase in carbon-carbon distance in smaller diameter CNTs is observed, when compared to graphite. Similarly, in MWCNTs inner tubes are more strained than outer tubes. This phenomenon significantly influences the electronic properties of CNTs.

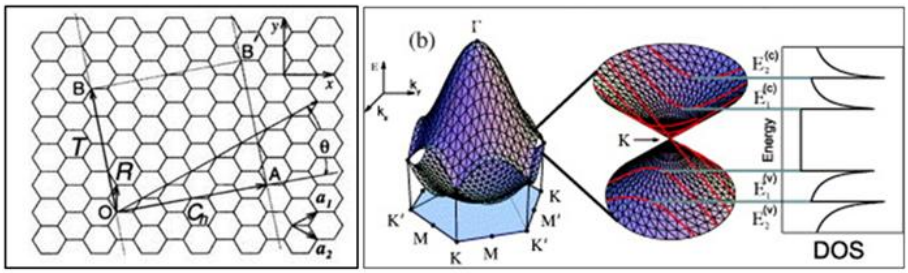

(a) (b)

Figure 1.2: (a) Geometrical scheme for generating CNTs from a graphene sheet (b) constant energy contour for the conduction, valance band of graphene. Further it relates the degeneracy at K point with allowed modes (red line) and corresponding density of states [28].

1.1.4 Electronic structure of CNTs

The basic electronic structure of a SWCNT or the shell of a MWCNT can be readily deduced in 2D graphene by viewing it as a quantum confinement in a 1D

electronic state. Graphene is a semimetal with valence and conduction bands degenerate only at six corners (K) of its hexagonal first Brillouin zone (fig.-1.2). The Fermi surface of a graphene sheet is thus reduced to these six points. In a SWCNT, the wave vector k is quantized along the circumferential direction due to a periodic boundary condition: $k * C_h = 2\pi q$, where q is an integer and C_h is the chiral roll-up vector. Therefore, only a particular set of states, which are parallel to the corresponding tube axis with a spacing of 2/d, is allowed, where d is the diameter of the SWCNT. On the basis of this simple scheme, if one of the allowed wave vectors passes through a K point of the graphene sheet, the SWCNT should either behave as metallic, or it should be semiconducting. Here, the band gap (E_g) of a semiconducting SWCNT is strongly dependent on its diameter. This dependence can be expressed as Eg= 0.9eV/d. Based on the periodic boundary condition, SWCNTs can be generally expected to behave as metals when (n-m)/3 is an integer, and otherwise it behaves like a semiconductor. As a matter of fact, all armchair SWCNTs are truly metallic conductors as (n – n)/3 = 0. In the case of zigzag CNTs where (n – m)/3 is an integer predicted to be semi-metallic.

Zigzag nanotubes experience a shift in the Fermi level due to finite curvature effects because of their tubular construction. This results in the formation of small band gaps and hence, introduces the semiconducting characteristics. These band gaps are very small, and are inversely proportional to the square of the tube radius. Bundled armchair SWCNTs also exhibit “pseudo gaps” to modify their electrical transport prosperities. Adsorption of molecules and functionalization also significantly changes the electronic structure of the CNTs. Hence, from the above discussion it is evident that the electronic property of the CNTs is highly sensitive to external parameters.

CVD grown samples by and large contains CNTs with a wide range of distributions in tube diameter with varying chirality. In addition tubes may also contain defects on the walls along with impurities in the form of carbonaceous and non-carbonaceous materials. Raman spectroscopy provides crucial information in detecting these diameters and serves as an indispensible technique to investigate CNTs. In the following section a brief discussion is presented grow show how Raman spectroscopy study of CNTs can generate information on the intrinsic property of CNTs.

1.1.5 Raman spectroscopy of CNTs

Raman spectroscopy has historically played an important role in the structural characterization of graphitic materials. It has been widely used in the last four decades to characterize crystalline to amorphous carbon systems based on their sp^2 and sp^3 hybridization states. Basic structural properties, such as inplane crystallite size and out-of-plane stacking order have been shown to strongly affect the Raman spectra of graphite.

By virtue of one dimensional confinement of electronic and phononic states in CNTs, its density of states results in a Von-Hove singularity (fig.-1.2b). Indeed these features in electronic density of states bear unique signatures in Raman spectra. Based on group theory, the allowed vibrational modes for a SWCNT gives rise to radial breathing mode (RBM) and the popularly known G-band similar to graphite. Here, RBM originates from 'A' symmetry with all the carbon atoms moving in-phase in the radial direction and G-band from degenerating 'E' symmetry with neighboring atoms moving in opposite directions along the surface of the tube as seen in 2D graphite as shown in fig.-1.3a. Raman modes and their origin of symmetry are given in table-1.2.

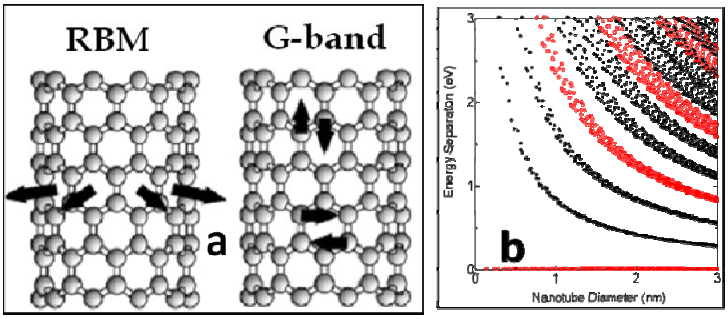

Figure 1.3: Kataura plot showing the different resonance excitations as a function of different energy lasers and diameters. Red and black symbols correspond to metallic and semiconducting tubes, respectively [29].

Notation	Frequency (cm)	Symmetry	Type of mode
RBM	α /d	A	In phase radial displacements
D-band	1350	A	Defect-induced, dispersive
G-band	1550–1605	A, E_1 , E_2	Graphite-related optical mode
G'-band	2700	–	Overtone of D-band, highly dispersive

Table 1.2: Raman shifts corresponding to symmetry related modes for CNTs.

Both the RBM and G bands are sensitive to geometrical structure (n,m) of the nanotube. It can be shown that the RBM Frequency (ω_{RBM}) is independent of chiral angle θ and linearly depend on the reciprocal of the nanotube diameter (d) in accordance with the relation $\omega_{RBM} = \alpha /d$ [30-31]. Here, α can be theoretically calculated and can be experimentally verified. Further, it is possible to find the geometrical structure (n m) of a nanotube from a Kataura plot [29] as shown in fig.-1.3b. Here, d can be evaluated from ω_{RBM} and the transition energy E_{ii} determined by measuring the Stokes and anti-Stokes signals with the aid of a tunable laser.

Further the symmetry breaking in the radial and axial direction of CNTs gives rise to a multi-peak feature in tangential G mode. These peaks contains chiral

information. From the line shape of this mode the nature of the CNTs can be differentiated as a metal or semiconductor.

Loss of translational symmetry by defects activates other intense Raman modes called D and G' bands. Here, the former is attributed to an 'A' symmetry mode and the latter is the second harmonic of the D band [28, 32]. Defects can exist in the form of in-plane substitutional hetero-atoms, vacancies, grain boundaries and finite size effects. Based on theoretical calculations, for an infinite defect free SWCNT, the D band virtually shows zero intensity [33].

Unlike SWCNTs, in MWCNTs the characteristic signature of the RBM is not very distinct. The RBM signal from larger diameter tubes are normally weak due to the ensemble average of the overlapping peaks that originate from the multiwall. Similarly, splitting of the G band in MWCNTs is both small in intensity and smeared out due to the effect of the diameter distribution between individual MWCNTs. Thus the G-band feature predominantly exhibits a weakly asymmetric characteristic line shape, with a peak close to the graphite frequency of 1582 cm^{-1} [28].

In the case of FWCNTs, RBM and multiple G- band splitting can be observed as found in SWCNTs. These features are weak due to the interaction between walls and the relatively higher diameter than SWCNTs. [34]. The present study, exploits this feature to establish the correlation between structure and transport properties through Raman spectroscopy.

1.2 Transport properties of CNTs

A wide range of interesting transport properties are observed in CNT materials, since a small variation in tube structure (including defects and functionalization of tubes), extent of tube junctions and scattering centers, tube-tube interactions, number of walls, metallic/ semiconducting nature etc., can

greatly influence the transport, which can vary from ballistic to diffusive. The transport behavior can exhibit different aspects depending on the sample being investigated, which could be an isolated SWCNT, a MWCNT or a network of CNTs.

1.2.1 Isolated CNTs

As the size of a conductor is decreased in a mesoscopic system, Ohm's law is no longer strictly valid and size dependent phenomena arise. In general the electron mean free path, Lm, determines the transport regime: if Lm is longer than the sample length L, the electrons are ballistic. Otherwise transport can show either diffusive (power law, variable range hopping (VRH)) or classical Ohmic behavior, depending on whether elastic or inelastic scattering processes contribute to Lm.

It is reported that transport properties in an isolated SWCNT is ballistic as found in a one-dimensional quantum wire. With an ideal electrical contact, electron transport in a SWCNT will manifest as two units of quantum conductance $G = 2G_0 = 4e^2/h$ (resistance $R = h/4e^2 = 6.45$ kV) in the system. Here, e is the electronic charge, h is the Planck's constant and the factor 2 comes from available two channels in electronic sub bands,

In MWCNTs, both ballistic and diffusive transport properties have been reported [35-40]. Interaction between the walls in the larger diameter tubes affects the conducting property of the MWCNTs. In addition, the complexity adds to the experimental verification such that, to make contact to all co-axial tubes in the MWCNT. In the conventional two probe or four probe technique, contacts are normally from the outer most wall of the MWCNTs and hence the observed conductance is found similar ($\sim 2\ G_0$) to that of a SWCNT [41]. These transport properties which are associated with individual CNTs determine the behavior of an ensemble of CNTs in a network transport.

1.2.2 CNT network

Synthesis of CNTs by a thermal CVD method normally yields a mixture of metallic and semiconducting nanotubes of different diameters. Fuhrer et al. [42] have shown that the intersection of two SWCNTs both with a semiconducting or metallic nature form a good electrical contact with conductance 0.1 e^2/h. In contrast, the intersection of a metallic and a semiconducting SWCNT forms a Schottky barrier with a barrier height approximately equal to 1/2 the band gap of the SWCNT nanotube. A network of randomly interconnected CNTs is expected to be electrically continuous with properties that depend on the interconnections and the inherent properties. The presence of defects in the CNT, and impurities in the network, may affect both the interconnections in the nanotube and the properties of individual tubes themselves. Doping of the nanotubes within the network can significantly alter the conductance of the network through a modulation of the charge carrier density and/or nanotube interconnection barrier [43-44].

The conductivity of carbon nanotube networks has been widely observed to be diffusive. Hecht et al. [45] have shown that a power law dependence on the length of CNTs and an inverse power law dependence on the CNT diameter, highlights the critical role of constituent carbon nanotube elements in the network. In a bundle or a rope of CNTs, metallic conduction $d\rho/dT>0$ may be observed above room temperature. However, temperature dependent transport properties show nonmetallic behavior ($d\rho/dT<0$) at a sufficiently low temperature [46-47]. Theoretical and experimental work have revealed that metallic SWCNTs in the bundle will open up a small energy gap or pseudo-gap of ~0.1 eV owing to intertube interactions in the bundle [48-49].

Heterogeneities found in metallic and semiconducting tubes, such as inherent defects, tube to tube contacts and conduction through localized states, among the CNTs in a network allow them to be considered as a disordered semiconductor. Conduction in a CNT network termed hopping occurs by phonon-assisted tunneling between electronic localized states centered at different positions. As the thermal energy, k_BT decreases with temperature, there are fewer nearby states with accessible energies, so the mean range of hopping increases. This leads to the following expression for the conductivity,

$$\sigma = \sigma_0 exp\left[-\left(\frac{T_0}{T}\right)^{1+d}\right] \tag{1.4}$$

where, d denotes the dimensionality of hopping. If the electronic wave function decays with distance r as $\exp(-r/L_{loc})$, where L_{loc} is the localization length, a constant T_0 is given approximately by $k_BT_0 \sim 16/(N(E_F)L^3_{loc})$, where $N(E_F)$ is the density of localized states at the Fermi level.

At sufficiently high temperatures, the conductivity follows the simple activated form given by eqn-1.4 with $\gamma=1+d = 1$. This behavior is similar to a thermal excitation of electrons into a conduction band in a crystalline semiconductor. Hence, enhanced conduction would be approximately proportional to the number of electrons excited across the semiconductor gap.

An electrical conductivity study of a wide variety of CNT networks shows some discrepancy over the VRH conduction mechanism. In particular, poor temperature dependence and non-zero conductance in the absolute zero-temperature limit do not strictly follow the hopping conduction mechanism. Sheng et al., [50] proposed a conduction mechanism based on fluctuation induced tunneling (FIT)

which describes the conducting behaviour of nanotube networks. Here, tunneling of a charge carrier across a thin barrier is thermally assisted and takes the form,

$$\sigma(T) = \sigma_t exp\left[-\left(\frac{T_t}{T+T_s}\right)\right] \quad (1.5)$$

where, σ(T) is the temperature dependent conductance in the network. the parameter T_t represents the temperature at which the thermal voltage fluctuations become large enough to raise the energy of electronic states to the top of the barrier. The ratio T_t/T_s determines the tunneling in the absence of fluctuations and the conductivity σ(0) is in the limit of absolute zero temperature. The prefactor σ_t is approximated to be independent of temperature.

From all the above studies, one could conclude that the transport property of the CNT network cannot be predicted by a single mechanism. Hence, the temperature dependence of conductance can be expressed in the combined form of metallic conduction, VRH and Fluctuation induced tunneling (FIT) is given by,

$$\sigma(T) = \sigma_m exp\left(\frac{T_m}{T}\right) + \sigma_0 exp\left[-\left(\frac{T_0}{T}\right)^{1+d}\right] + \sigma_t exp\left[-\left(\frac{T_t}{T+T_s}\right)\right] \quad (1.6)$$

In this thesis, the intricate relation between the structural defects of CNTs on the transport mechanism is examined for FWCNTs. Further, the study is extended to explore transport properties of the metal and metal oxide decorated FWCNTs hybrid materials to study for their novel properties

1.3 Synthesis of CNTs

The synthesis of carbon nanotubes with controlled diameter, chirality, number of graphite layers, length and quality has been the key and crucial part of carbon nanotube research since the unique chemical and physical properties of CNTs are determined by the structure of CNTs.

Arc discharge, laser ablation and chemical vapor deposition (CVD) are the three well known methods used for the preparation of CNTs, while the other methods, such as plasma enhanced CVD (PECVD) and hydrothermal methods have also employed [5, 51-54]. Arc discharge and laser ablation methods have been developed to produce both high quality SWCNTs and MWCNTs. In particular, SWCNTs produced by the arc discharge method show an impressively narrow distribution in diameter averaging about 1.4 nm [55]. However, these methods can only produce randomly mixed and tangled nanotubes with byproducts, such as fullerenes, graphitic polyhedra with enclosed catalytic metal particles and amorphous carbon in the form of particles or as a coating on the sidewalls of the carbon nanotubes. This preparation method provides only a limitted control over dimensions (length and diameter) of the carbon nanotubes. Most importantly, the cost associated with these methods is relatively high and the experimental setup cannot easily be scaled up for mass production of carbon nanotubes. To overcome these difficulties alternative possibilities have been explored and CVD has been found to be a promising technique to circumvent the problems.

The CVD method has long been used since the 1970s to produce carbon fibers [56] and the method has been successfully been modified to meet the requirements to the synthesis of CNTs. Compared with arc discharge and laser ablation methods, the CVD method can produce CNTs not only in bulk quantity in powder form, but also on flat substrate surfaces. At present, compatible techniques are available to integrate the CNTs into nanoscale electronics and optical devices. CVD method can also give the handle to control the growth of CNTs by tuning a variety of parameters in the CVD process such as temperature, carbon feed and catalyst. This method is also the most efficient and economical for large scale production of CNTs. So far, the major

problem encountered in this method is the high defect density in CNT sidewalls compared with those from arc discharge and laser ablation methods. This may probably be due to the relatively lower reaction temperature used that is normally below 1100 ^{o}C. It is possible to overcome drawbacks associated with CVD growth through potential application of post growth treatments to significantly enhance the quality of the tubes. In this thesis, the CVD method is exploited to synthesize the MWCNTs and mild acid treatments were explored to make high quality FWCNTs.

1.3.1 Growth mechanism of CNTs by CVD

Many mechanisms have been proposed to explain the CNT growth in the CVD process which strongly depends on the synthesis parameters. The most, widely accepted mechanism for supported catalytic nanoparticles is 'dissociation-diffusion-precipitation' [57]. In this model, the carbon source is dissociated on the surface of the catalytic nanoparticles which subsequently dissolve in the carbon produced by the dissociation reaction and once super saturated; carbon precipitates out and crystallizes in the form of a cylindrical network. Here, catalytic properties of the nanoparticles are largely associated with the particle size, catalyst combination, catalyst support interaction, temperature and precursor used.

Temperature and concentration gradients were considered to be the main driving forces for continued CNT growth dynamics [58]. Further, depending on the catalyst-solid support interaction carbon precipitates on the top or the bottom of the catalyst nanoparticles. The former growth mechanism is called tip growth and latter base growth. A schematic diagram of the growth process is shown in fig.-1.4a, b, c.

Although, this mechanism is widely accepted, there are several issues still open to debate. These include: (1) It is not obvious that, during CNT growth, the metal is in the solid or liquid state (2) whether the carbon diffusion in metal is volume

diffusion or surface diffusion and (3) the actual catalyst for CNT growth is the pure metal or metal carbide.

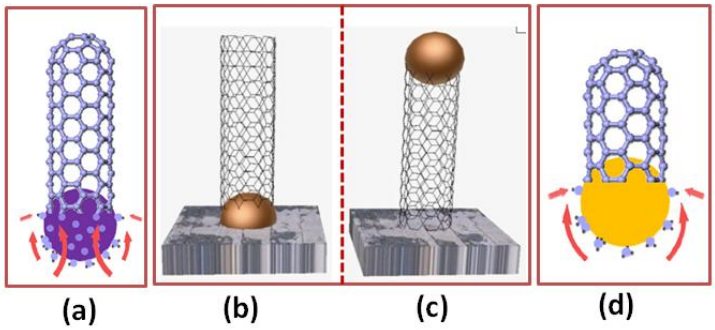

Figure 1.4: VLS growth mechanism (a) bulk diffusion of molecule (b) base growth (c) tip growth and (d) VSS mechanism.

In 1984, Tibbetts et al., [59] assumed a liquid state for the catalyst and proposed a vapor-liquid-solid (VLS) model for CNT growth. Here, they considered abrupt reduction in melting point of the metal when it was in the form of nanoparticles. Experimental observations such as the change in the catalyst shape and encapsulation of the catalyst by capillary action supported a model requiring a liquid state for the active catalyst. However, the mechanism could not explain the growth of MWCNT on bigger particles. Further, in the case of SWCNTs, it is very hard to imagine a significant temperature gradient within a particle of 1-2 nm. Hence, the SWCNT growth is considered to be driven only by the carbon concentration gradient during the process. [60].

Recently, metal free CNT growth was reported by Chen et al., [61] and the growth mechanism was monitored using in-situ resonance Raman spectroscopy and X-ray photoelectron spectroscopy. The results suggest that, SWCNT nucleation and growth occur by carbon diffusion on solid SiO_2 particles, and agrees with a vapor-solid-solid (VSS) model. An alternative growth mechanism based on the self-assembly of acetylene into poly-aromatic fragments has recently been proposed. In

this "polymerization" like model, the CNT growth proceeds by the addition of new small polyines or graphene-like fragments built from unsaturated molecules [62-64]. Using this model A Magrez et al., [65] demonstrated that super growth of aligned CNTs by controlling the acidity of the catalyst support. This model opens up the new possibility of CNT growth on a required support material for technologically important applications.

1.4 CNT based Gas sensors

Nanomaterials with extremely high surface-to-volume ratio and with a hollow structure are ideal for gas molecule adsorption and storage. Therefore, gas sensors based on nanomaterials, such as nanotubes, nanowires, nanofibers, and nanoparticles, have been widely investigated. In this regard, CNTs are ideally suited for gas sensors due to their large surface area, excellent electrical transport and facile charge transfer characteristics at room temperature. However, CNTs have certain limitations such as low sensitivity and a long recovery time. Two common ways to improve CNTs are by operating them at elevated temperatures or by loading them with metal (Au , Pt and Pd) or metal oxide (SnO_2, TiO_2, and SiO_2) nanoparticles [66-67]. Further additions of metal and metal oxide provide mechanically and chemically robust and stable sensors which can operate at higher temperature and in harsher environments. Understanding of the gas sensing mechanism in these CNT based chemiresistive sensors will provide opportunities for constructing novel sensors. The key mechanisms involved in CNT and network of CNTs are grouped together and discussed below,

- 'Fermi level shift from charge transfer by adsorbed molecules'

CNTs can be regarded as graphene sheets that have three σ- bonds and one out of plane π- bond. Due to the distortion of the electron clouds of CNTs from a uniform distribution in graphite to an asymmetric distribution around cylindrical nanotube

generate a rich π-electron conjugation form outside the CNTs, making them extremely sensitive to charge transfer and chemical doping effects by various molecules [68]. For example, interaction of CNTs with electron-withdrawing molecules (e.g. NO_2, O_2) or electron-donating molecules (e.g. NH_3) creates changes in electrical conduction which is closely associated with a Fermi level shift.

A single CNT or networks of CNTs have been used to studying various gas molecules. Kong et al,[15] demonstrated the first CNT based gas sensor using SWCNTs as the channel in a FET configuration. On the other hand, the change of resistance in CNTs under gas exposure can also be detected by two terminal resistors with dc voltage.

- 'Adsorbed analyte molecule may act as a scattering center for charge carriers'

A significant change in the conductivity is observed for inert gases like He and N_2. The weak charge transfer characteristics of these gases can be explained through a change in the electron and hole free carrier lifetimes. These large changes in the carrier lifetime can be caused either by the increased carrier scattering from dynamic defect states associated with momentarily adsorbed gas or by nonthermal, localized SWCNT phonons generated by collision of the gas molecules with the tube wall [69].

- 'Variation of Schottky barrier created by metal-CNT contact'

Adsorption of gas molecules at the metal-CNT interface can create a variation in the Schottky barrier height. By suitably changing the metal electrode one can change the sensitivity of the gas sensor [70].

- 'Intertube charge conduction modified by gas molecule adsorption'

In a CNT bundle the binding energy of adsorbed gas molecules onto the external surface of a CNT the bundle, the groove formed at the contact between adjacent tubes, the interior pore of individual tubes and the interstitial channel formed

between three adjacent tubes within the bundle will be differed. Apart from this, adsorbed molecules on the junction between the CNTs also change the conduction properties in the network. All these processes affect the resistance of the network by altering the tunneling probabilities due to hopping via CNTs molecular orbitals [71].

1.5 Scope of the current work

Studies on synthesis, characterization and application of CNTs have been extensively reported in the literature for the past few decades. However, it is a long way to go in taking this material from the laboratory scale to industrial applications. These scenarios clearly make it obvious that there are a number of issues yet to be addressed. While various CNT growth mechanisms have been reported, there exists a lack of comprehensive understanding of these issues. While the controlled synthesis is possible at laboratory scale, the productions of CNTs in large scale with specific features are still elusive and challenging. This provides a motivation for the current work, i.e., to address the issues related to CNT synthesis by varying a combination of CVD parameters and catalytic supports. The catalytic particle size, porosity and loading considerations have been studied and the optimum parameters for the synthesis of FWCNT have been reported. An important aspect of methane cracking during the CVD process is identified either as due to catalytic or thermal decomposition. This crucial information explains the different role of a catalytic support material in combination with catalyst.

This thesis focuses on the synthesis of FWCNTs owing to their unique features with a narrow band gap and easy scalability for large scale production. A narrow distribution in tube diameter is an essential requirement in the synthesis of FWCNTs. In general the FWCNT diameters are below 10 nm. In this thesis an innovative recipe is proposed based on a catalyst combination (Fe and Mo) and

catalytic support (MgO). The simple combination of MgO and Fe results in MWCNTs whereas addition of Mo is narrows down the distribution in the tube diameters. Subsequent to growth, purification plays an important role as the product contains a variety of carbonaceous material and catalyst nanoparticles as impurities. The major consideration in the purification process is to aim for CNTs with high purity with superior structural qualities. In this thesis, soft chemical purification methods are used and evaluated the purity and integrity of the CNTs were determined by TGA and Raman spectroscopy respectively. The prescribed purification recipe demonstrated purity as high as 99.5% with a maximum structural integrity (I_D/I_G~0.13).

From the application perspective of CNTs, their temperature dependent electrical transport properties have been studied. The intricate relationship of the structural defects and the conduction mechanism is analyzed. The temperature dependant variation in the electrical transport property is modeled with a combination of FIT and VRH mechanisms. The temperature dependant contribution of these two different conduction process is evaluated. These studies aid in the understanding of this CNT material in sensor applications.

The ultimate utility of these materials have been investigated in the field of gas sensors. The large surface area and charge transfer capabilities make this material an ideal candidate. CVD grown FWCNTs are used as sensor materials for the detection of N_2O, NO_2, CH_4, NH_3, H_2 and ethanol. Further, to improve the selectivity and sensitivity functionalization of the CNTs was carried out using SnO_2 and Pd. Functionalization enables these hybrid materials to operate at room temperatures. As an alternative approach for detection of gases the field emission properties of CNTs are also studied using Fowler-Nordheim analysis.

1.6 References

[1] L. V. Radushkevich and V. M. Lukyanovich, "About the carbon structure, synthesised during thermal decomposition of CO on metal contacts " *Soviet Journal of Physical Chemistry,* vol. 26, p. 88, 1952.

[2] M. Hillert and N. Lange, "The structure of graphite filaments," *Zeitschrift für Kristallographie,* vol. 111, p. 24, 1959.

[3] W. Bollmann and J. Spreadborough, "Action of graphite as a lubricant," *Nature,* vol. 186, p. 29, 1960.

[4] A. Oberlin*, et al.*, "Filamentous growth of carbon through benzene decomposition," *Journal of Crystal Growth,* vol. 32, p. 335, 1976.

[5] H. Kroto*, et al.*, "C60: Buckminsterfullerene," *Nature* vol. 318, p. 162, 1985.

[6] S. Iijima, "Helical microtubules of graphitic carbon," *Nature,* vol. 354, p. 56, 1991.

[7] S. Iijima and T. Ichihashi, "Single-shell carbon nanotubes of 1-nm diameter," vol. 363, p. 603, 1993.

[8] D. Bethune*, et al.*, "Cobalt-catalysed growth of carbon nanotubes with single-atomic-layer walls," vol. 363, p. 605, 1993.

[9] T. Dürkop*, et al.*, "Extraordinary mobility in semiconducting carbon nanotubes," *Nano Letters,* vol. 4, p. 35, 2004.

[10] B. Wei*, et al.*, "Reliability and current carrying capacity of carbon nanotubes," *Applied Physics Letters,* vol. 79, p. 1172, 2001.

[11] J. Hone*, et al.*, "Thermal properties of carbon nanotubes and nanotube-based materials," *Applied Physics A: Materials Science & Processing,* vol. 74, p. 339, 2002.

[12] B. Demczyk*, et al.*, "Direct mechanical measurement of the tensile strength and elastic modulus of multiwalled carbon nanotubes," *Materials Science and Engineering: A,* vol. 334, p. 173, 2002.

[13] A. Krishnan*, et al.*, "Young's modulus of single-walled nanotubes," *Physical Review B,* vol. 58, p. 14013, 1998.

[14] J. Kong*, et al.*, "Functionalized carbon nanotubes for molecular hydrogen sensors," *Advanced Materials,* vol. 13, p. 1384, 2001.

[15] J. Kong*, et al.*, "Nanotube molecular wires as chemical sensors," *Science,* vol. 287, p. 622, 2000.

[16] P. G. Collins*, et al.*, "Extreme oxygen sensitivity of electronic properties of carbon nanotubes," *Science,* vol. 287, p. 1801, 2000.

[17] A. C. Dillon*, et al.*, "Storage of hydrogen in single-walled carbon nanotubes," *Nature,* vol. 386, p. 377, 1997.

[18] S. J. Tans*, et al.*, "Room-temperature transistor based on a single carbon nanotube," *Nature,* vol. 393, p. 49, 1998.

[19] J. Planeix*, et al.*, "Application of carbon nanotubes as supports in heterogeneous catalysis," *Journal of the American Chemical Society,* vol. 116, p. 7935, 1994.

[20] S. Saito, "Carbon nanotubes for next-generation electronics devices," *Science,* vol. 278, p. 77, 1997.

[21] P. Kim and C. M. Lieber, "Nanotube Nanotweezers," *Science,* vol. 286, p. 2148, December 10, 1999 1999.

[22] P. Serp*, et al.*, "Carbon nanotubes and nanofibers in catalysis," *Applied Catalysis A: General,* vol. 253, p. 337, 2003.

[23] S. Itoh*, et al.*, "Helically coiled cage forms of graphitic carbon," *Physical Review B,* vol. 48, p. 5643, 1993.

[24] S. Amelinckx*, et al.*, "A formation mechanism for catalytically grown helix-shaped graphite nanotubes," *Science,* vol. 265, p. 635, 1994.

[25] A. Javey*, et al.*, "Electrical properties and devices of large-diameter single-walled carbon nanotubes," *Applied Physics Letters,* vol. 80, p. 1064, 2002.

[26] R. Kamalakannan*, et al.*, "The role of structural defects on the transport properties of a few-walled carbon nanotube networks," *Applied Physics Letters,* vol. 98, p. 192105, 2011.

[27] T. Shimada*, et al.*, "Double-wall carbon nanotube field-effect transistors: Ambipolar transport characteristics," *Applied Physics Letters,* vol. 84, p. 2412, 2004.

[28] M. S. Dresselhaus*, et al.*, "Raman spectroscopy of carbon nanotubes," *Physics Reports,* vol. 409, p. 47, 2005.

[29] H. Kataura*, et al.*, "Optical properties of single-wall carbon nanotubes," *Synthetic Metals,* vol. 103, p. 2555, 1999.

[30] A. Jorio*, et al.*, "Structural (n, m) determination of isolated single-wall carbon nanotubes by resonant Raman scattering," *Physical Review Letters,* vol. 86, p. 1118, 2001.

[31] A. G. S. Filho*, et al.*, "Raman spectroscopy for probing chemically/physically induced phenomena in carbon nanotubes," *Nanotechnology,* vol. 14, p. 1130, 2003.

[32] A. C. Dillon*, et al.*, "Systematic inclusion of defects in pure carbon single-wall nanotubes and their effect on the Raman D-band," *Chemical Physics Letters,* vol. 401, p. 522, 2005.

[33] R. Saito*, et al.*, "Raman intensity of single-wall carbon nanotubes," *Physical Review B,* vol. 57, p. 4145, 1998.

[34] X. Zhao*, et al.*, "Multiple splitting of G-band modes from individual multiwalled carbon nanotubes," *Applied Physics Letters,* vol. 81, p. 2550, 2002.

[35] L. Langer*, et al.*, "Quantum Transport in a Multiwalled Carbon Nanotube," *Physical Review Letters,* vol. 76, p. 479, 1996.

[36] H. Dai*, et al.*, "Probing Electrical Transport in Nanomaterials: Conductivity of Individual Carbon Nanotubes," *Science,* vol. 272, p. 523, 1996.

[37] P. Collins and P. Avouris, "Multishell conduction in multiwalled carbon nanotubes," *Applied Physics A: Materials Science & Processing,* vol. 74, p. 329, 2002.

[38] P. Poncharal*, et al.*, "Room temperature ballistic conduction in carbon nanotubes," *The Journal of Physical Chemistry B,* vol. 106, p. 12104, 2002.

[39] C. Berger*, et al.*, "Ballistic conduction in multiwalled carbon nanotubes," *Journal of Nanoscience and Nanotechnology,* vol. 1, p. 171, 2003.

[40] A. Urbina*, et al.*, "Quantum Conductance Steps in Solutions of Multiwalled Carbon Nanotubes," *Physical Review Letters,* vol. 90, p. 106603, 2003.

[41] H. J. Li*, et al.*, "Multichannel Ballistic Transport in Multiwall Carbon Nanotubes," *Physical Review Letters,* vol. 95, p. 086601, 2005.

[42] M. S. Fuhrer*, et al.*, "Crossed Nanotube Junctions," *Science,* vol. 288, p. 494, 2000.

[43] J. Li*, et al.*, "Carbon nanotube sensors for gas and organic vapor detection," *Nano Letters,* vol. 3, p. 929, 2003.

[44] M. Penza*, et al.*, "Functional characterization of carbon nanotube networked films functionalized with tuned loading of Au nanoclusters for gas sensing applications," *Sensors and Actuators B: Chemical,* vol. 140, p. 176, 2009.

[45] D. Hecht*, et al.*, "Conductivity scaling with bundle length and diameter in single walled carbon nanotube networks," *Applied Physics Letters,* vol. 89, p. 133112, 2006.

[46] J. E. Fischer*, et al.*, "Metallic resistivity in crystalline ropes of single-wall carbon nanotubes," *Physical Review B,* vol. 55, p. R4921, 1997.

[47] J. Hone*, et al.*, "Thermoelectric Power of Single-Walled Carbon Nanotubes," *Physical Review Letters,* vol. 80, p. 1042, 1998.

[48] P. Delaney*, et al.*, "Broken symmetry and pseudogaps in ropes of carbon nanotubes," *Nature,* vol. 391, p. 466, 1998.

[49] M. Ouyang*, et al.*, "Energy Gaps in "Metallic" Single-Walled Carbon Nanotubes," *Science,* vol. 292, p. 702, 2001.

[50] P. Sheng*, et al.*, "Fluctuation-Induced Tunneling Conduction in Carbon-Polyvinylchloride Composites," *Physical Review Letters,* vol. 40, p. 1197, 1978.

[51] T. Guo*, et al.*, "Self-assembly of tubular fullerenes," *The Journal of Physical Chemistry,* vol. 99, p. 10694, 1995.

[52] Ç. Öncel and Y. Yürüm, "Carbon nanotube synthesis via the catalytic CVD method: A review on the effect of reaction parameters," *Fullerenes, Nanotubes, and Carbon Nonstructures,* vol. 14, p. 17, 2006.

[53] M. Meyyappan*, et al.*, "Carbon nanotube growth by PECVD: a review," *Plasma Sources Science and Technology,* vol. 12, p. 205, 2003.

[54] J. Prasek*, et al.*, "Methods for carbon nanotubes synthesis - review," *J. Mater. Chem.,* vol. 21, p. 15872, 2011.

[55] C. Rao*, et al.*, "Nanotubes," *ChemPhysChem,* vol. 2, p. 78, 2001.

[56] P. A. Tesner*, et al.*, "Formation of carbon fibers from acetylene," *Carbon,* vol. 8, p. 435, 1970.

[57] M. Kumar and Y. Ando, "Chemical vapor deposition of carbon nanotubes: a review on growth mechanism and mass production," *Journal of nanoscience and nanotechnology,* vol. 10, pp. 3739-3758, 2010.

[58] R. T. K. Baker, "Catalytic growth of carbon filaments," *Carbon,* vol. 27, p. 315, 1989.

[59] G. G. Tibbetts, "Why are carbon filaments tubular?," *Journal of Crystal Growth,* vol. 66, p. 632, 1984.

[60] F. Ding*, et al.*, "Molecular dynamics study of SWNT growth on catalyst particles without temperature gradients," *Computational Materials Science,* vol. 35, p. 243, 2006.

[61] Y. Chen and J. Zhang, "Diameter controlled growth of single-walled carbon nanotubes from SiO2 nanoparticles," *Carbon,* vol. 49, p. 3316, 2011.

[62] G. Eres*, et al.*, "Model for self-assembly of carbon nanotubes from acetylene based on real-time studies of vertically aligned growth kinetics," *The Journal of Physical Chemistry C,* vol. 113, p. 15484, 2009.

[63] G. Eres*, et al.*, "Molecular beam-controlled nucleation and growth of vertically aligned single-wall carbon nanotube arrays," *The Journal of Physical Chemistry B,* vol. 109, p. 16684, 2005.

[64] Y. Yao*, et al.*, "“Cloning” of Single-Walled Carbon Nanotubes via Open-End Growth Mechanism," *Nano Letters,* vol. 9, p. 1673, 2009.

[65] A. S. Magrez, R*, et al.*, "Striking influence of the catalyst support and its acid-base properties: new insight into the growth mechanism of carbon nanotubes," vol. 5, p. 3428, 2012.

[66] H.-Q. Nguyen and J.-S. Huh, "Behavior of single-walled carbon nanotube-based gas sensors at various temperatures of treatment and operation," *Sensors and Actuators B: Chemical,* vol. 117, p. 426, 2006.

[67] E. H. Espinosa*, et al.*, "Hybrid metal oxide and multiwall carbon nanotube films for low temperature gas sensing," *Sensors and Actuators B: Chemical,* vol. 127, p. 137, 2007.

[68] Y. Wang and J. T. W. Yeow, "A review of carbon nanotubes-based gas sensors," *Journal of Sensors,* vol. 2009, p. 1, 2009.

[69] G. U. Sumanasekera*, et al.*, "Effects of Gas Adsorption and Collisions on Electrical Transport in Single-Walled Carbon Nanotubes," *Physical Review Letters,* vol. 85, p. 1096, 2000.

[70] J. H. Lee*, et al.*, "Bias modulated highly sensitive NO_2 gas detection using carbon nanotubes," *Sensors and Actuators B: Chemical,* vol. 129, p. 628, 2008.

[71] D. J. Mowbray*, et al.*, "Influence of O_2 and N_2 on the conductivity of carbon nanotube networks," *Physical Review B,* vol. 79, p. 195431, 2009.

Chapter-2 Development and fabrication of thermal CVD and gas sensor test facility

2.1 Introduction

This chapter provides the details on design and development of an in house fabricated thermal CVD set up for controlled synthesize of CNTs and also a gas sensor test facility for studying the response of the sensor to ppm levels of analyte gas. The salient features of these setups are given in detail. Further, the experimental methods for sensor fabrication and testing that involved spin coating, DC sputtering and sensor signal measurements are also discussed briefly.

2.2 Thermal CVD

In a typical CVD process chemical reactions take place on the surface of the required substrate. Here, gaseous reactants on or near the vicinity of a heated substrate surface produce a required solid material [1-2]. A Horizontal tube reactor configuration has been employed in the present CVD system. It belongs to the hot wall CVD family since during operation the reactor wall and cavity are heated up along with the precursor gas and sample. In this thesis, catalytic growth of CNTs is performed by CVD of methane. The catalyst-support combination is taken in an alumina boat, placed inside a quartz tube reactor positioned at the constant temperature zone of the resistively heated furnace. In the process Ar is used as carrier gas and NH_3 is used for reduction of the catalyst. Catalytic decomposition of the methane gas and CNT growth are achieved on the freshly formed active catalyst. During the CNT growth stage, methane is decomposed catalytically to give $2C+H_2$ and this carbon acts as carbon source for the formation of the nanostructures. Optimization of controllable parameters such as temperature, pressure, gas mixer ratio

and flow rate are necessary for the optimal growth of desired CNT structures. A brief introduction to the general CVD apparatus followed by details of the system used in the present work is discussed in the following section.

2.2.1 Basic components of a CVD apparatus

The CVD system comprised of the following basic components:

- Energy source – Provides the energy/heat that is required to get the precursors to decompose and react. It is a resistively heated horizontal reactor with a cylindrical hot cavity.
- Reactor chamber – It is a hot wall cylindrical quartz tube with provision for sample insertion and in the desired constant temperature zone.
- Gas delivery system – This provides the controlled supply of precursors to the reactor chamber. It includes mass flow controllers for mixing the source and carrier gas in desired ratio.
- Vacuum system – It is a system for the removal of all the gaseous species from the reaction chamber prior to the CVD process. This is required to maintain the purity and the ratio of the gas mixer during the growth process.
- Exhaust system – System for removal of volatile by-products and unconsumed reactants from the reaction chamber.
- Process control equipment – Gauges, controls etc to monitor and control the process parameters such as pressure, flow, temperature and time.

2.2.2 Energy source: CVD furnace

A tubular furnace with quartz tube reactor is used as a CVD system. The furnace has a tubular inner diameter of 40 mm and length of 50 cm. Heating was achieved by a super kanthal wire wound resistive heated furnace, which can be operated up to 1200^{o}C in an ambient atmosphere. Temperature of the furnace is

controlled by an eurotherm-906S PID controller coupled to an Eurocube 425A thyristor based power control. The PID controller has the capability to both auto tune and adaptive tune facility to precisely control the temperature. A k-type thermocouple is placed vertical to the tube axis at the center of the furnace. This is used as the control thermocouple to provide the feedback signal to the eurotherm controller for driving the thyristor output to the furnace. For calibration, a temperature profile along the tube axis of the furnace was measured by an external thermocouple when the furnace temperature is set at 800^{o}C and 900 ^{o}C and is shown in fig.-2.1. Here, the temperature variation of the hot zone is ±4 ^{o}C across 10 cm, as shown by the dotted line. The sample is usually placed within the central 3 cm of this hot zone where the temperature variation is less than ±0.5 ^{o}C

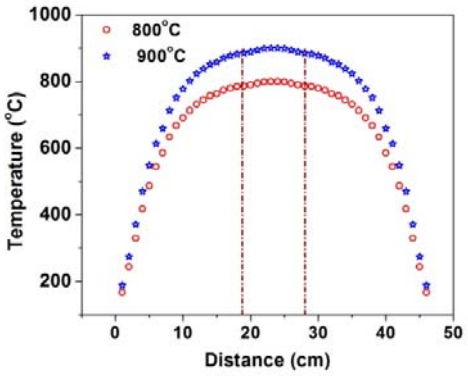

Figure 2.1: Temperature profile along the tubular axis of the furnace for 800^{o}C and 900^{o}C

2.2.3 Quartz tube reactor chamber

The details of the fabricated quartz tube reactor are shown in fig.-2.2. A quartz tube of 800 mm length, 5 mm thick and 35.5 mm outer diameter is chosen for the reactor chamber. One end of this tube is fused to a 10 mm diameter tube. This smaller side of the reactor serves as an outlet and the other end is the inlet for the gas. A SS KF-40 tubulation with 40 mm outer diameter (fig.-2.3 a&b) is inserted at the

larger opening side and fixed using torr-seal. A KF-40 SS flange with suitable holes as shown in fig.-2.3 c&d is used to blank it. Center bore was welded with a 6 mm

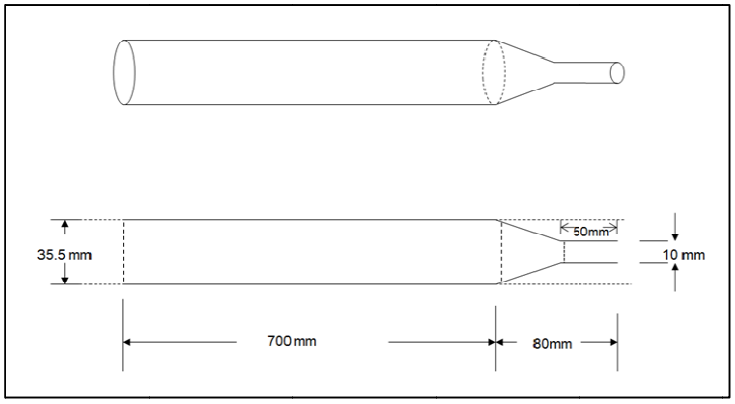

Figure 2.2: Schematic diagram of quartz tube reactor.

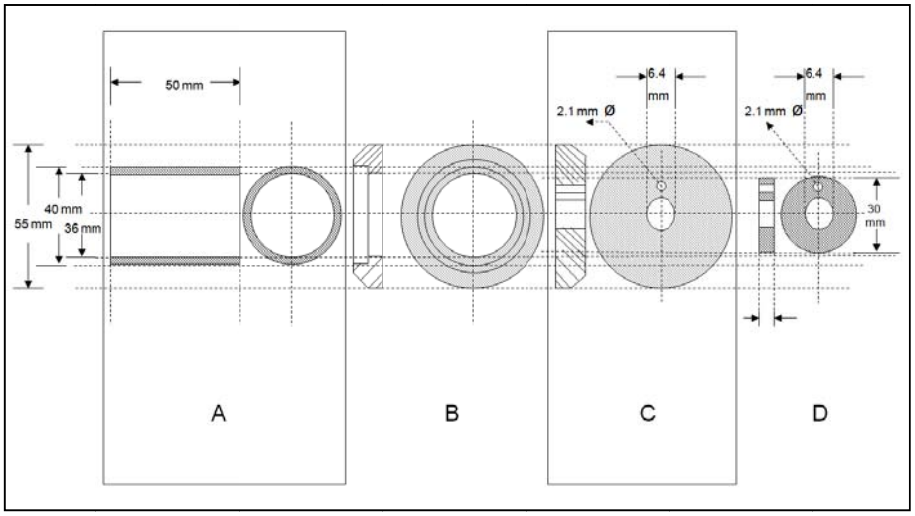

Figure 2.3: Block diagram of the flange assembly. (A) SS tube (B) flange with bore, (C) and (D) blank flange with 6.4 mm bore for gas inlet and 2.1 mm bore for thermocouple connections, respectively.

tube for the gas inlet. A k-type thermocouple is inserted through a 2.1 mm bore, with its sensing tip placed at the center of the quartz tube reactor and as close as possible to the sample position. Sealing between the flanges is achieved by a Vitan O-ring held

by a swing-away clamp. This inlet is connected via a gas assembly through SS tubing with double SS retainer ring and ferrule joints. To the other end a similar arrangement but of a smaller size (KF-16) is provided. A swagelock T-joint is used to connect a diaphragm gauge and a needle valve to control the pressure. The other end of the valve is directly connected to the exhaust or through a rotary pump depending on the requirement.

2.2.4 Gas delivery system

The gas inlet side of the TGA system is provided with a bank of four mass flow meters (20 – 1000 sccm, 1679A, M/s. MKS Instruments Inc., USA), with a multi gas controller (647 B, M/s. MKS Instruments Inc., USA), a gas blender and a Baratron pressure transducer (127 A, M/s. MKS Instruments Inc., USA), to provide a desired gas mixture of required composition to flow past the specimen.

Figure 2.4: Photograph of the in house fabricated CVD system.

2.3 Gas sensor test facility

Figure- 2.5 shows a schematic of the gas sensor test station designed and locally fabricated. The unit looks similar to the CVD set up but with a modified quartz chamber, gas assembly, in-situ heater, electrical connections and computer interface for monitoring the sensor signal. In this sensor set up, a prepared sensor wafer is connected with electrical wires using silver paste and carefully loaded into the quartz tube. The ratio of the carrier and analyte gas was controlled by a mass flow controller (MFC) and this controlled gas is sent into the quartz tube. The resistance data are recorded using a HP 34401A multimeter interfaced to a computer through suitable software. At the end of each experimental run, the system was evacuated and the all valves are closed. This was employed to avoid any contamination of the sensor. A brief discussion on the components of this gas sensor test facility is given in the next section.

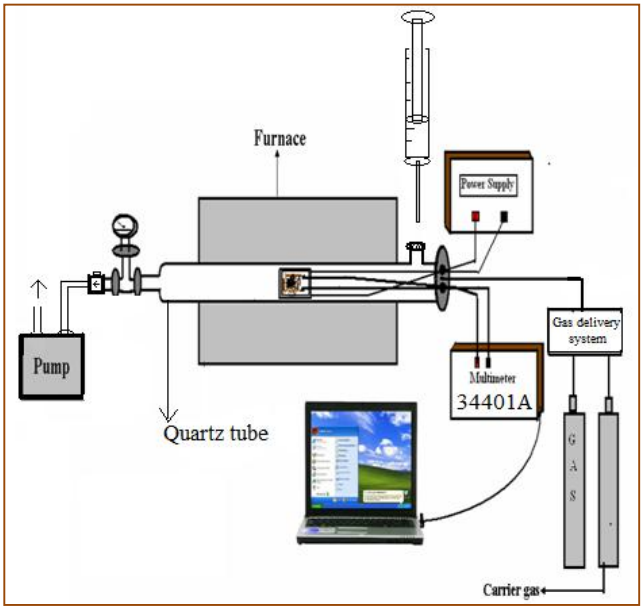

Figure 2.5: Schematic of the gas sensor test station.

2.3.1 Gas delivery system

The gas delivery system discussed in section 2.2.4 is suitably modified to send a gas mixture with ppm level of analyte. The mixing scheme is shown in fig.-2.6. Here, the analyte gas is mixed in two stages (S-1 and S-2). In S-1 the analyte gas (MFC-1) is mixed with carrier gas (MFC-2) and stored in Mix-1.Here, the analyte gas in the mixer is in percentage level. In stage two a specific amount of the mixed gas from Mix-1 is sent through MFC-3 and is further diluted by carrier gas from MFC-4 such that one can generate ppm level of the analyte gas in the carrier gas in two stages. This scheme can be extended further to dilute the gas to achieve a ppb level of analyte.

A vacuum pump is connected with Mix-1 to evacuate it each time before filling to avoid the presence of residual gases. All MFCs are connected with one way valves, to avoid the back flow of gases. Further to achieve a specified mixing ratio the MFCs are always maintained at a positive pressure between the gas inlet and outlet.

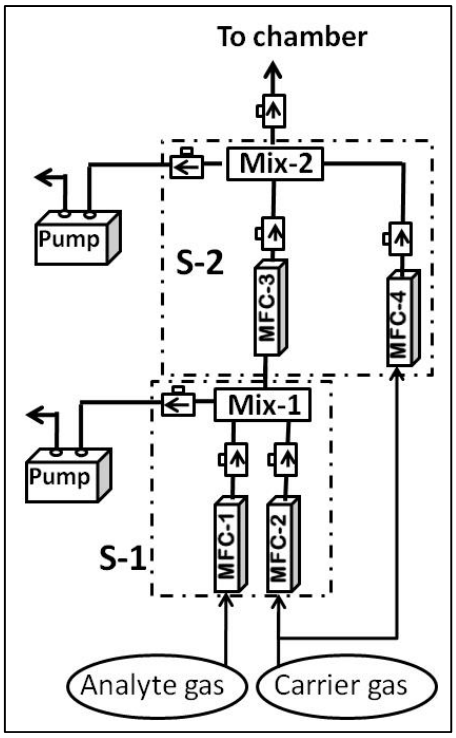

Figure 2.6: Gas delivery system with two mixing stages for producing ppm levels of a gas mixture.

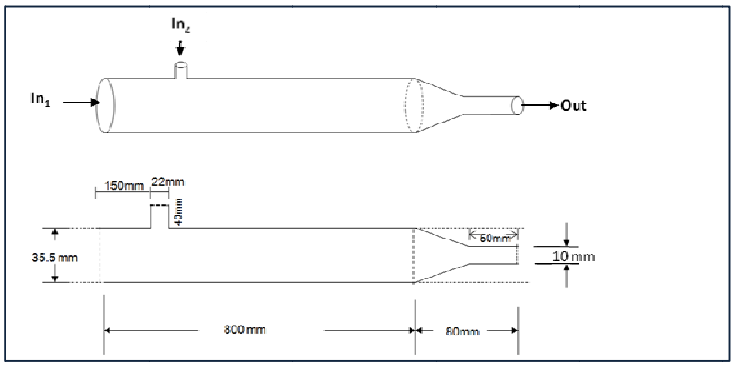

Figure 2.7: Schematic diagram for a quartz tube gas sensor test chamber.

2.3.2 Quartz tube assembly

This is the heart of the system consisting of a quartz tube with two inlet (In_1 & In_2) and an outlet (Out) as shown in fig.-2.7. Here In_1 and Out are connected with KF-40 and KF-16 SS fittings respectively, as discussed in section 2.2.3 for the CVD reactor. Here, the KF-40 flange consists of a vacuum compatible electrical feed through. Six electrical connections are given through this port. These electrical connections are shared between a sensor device, a in-situ heater and a thermocouple. Hence, the present setup can be used for both two and three probe devices for chemiresistor and FET, respectively. In_2 was sealed in a silicon rubber septum. For use as a dynamic gas sensor study, the gas is send through In_1 from gas delivery system. For use as a static gas sensor the gas was injected through a septum using a microlitter syringe through In_2. Here, the mixing ratio is calculated by knowledge of the volume of the quartz tube and the injected gas.

To test the sensors at different temperatures and also to regenerate them after exposure, a compact, low thermal inertia heater is required. Hence, a 22*22 mm compact resistive heater is made using a kanthal wire wounded in parallelly placed twin pore alumina tubes. Two ends of the wire were used for the external power supply (fig.-2.8). The heater is calibrated with a k type thermocouple for applied

voltages. In fig.-2.9 the current and temperature is plotted with respect to an applied voltage.

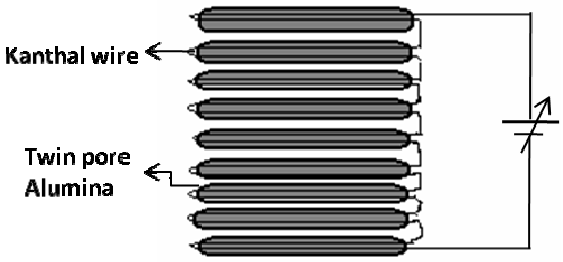

Figure 2.8: In situ resistive heater wounded in a twin pore alumina assembly.

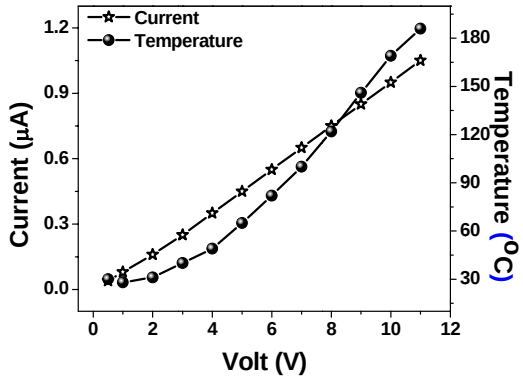

Figure 2.9: Voltage dependent current and corresponding temperature of the heater.

2.4 Device fabrication

The sensor device was prepared on a crystalline alumina substrate of dimension 18*18 mm. The required interdigitated electrode pattern is deposited using dc sputtering of gold by a shadow mask technique. The distance between two inter digitated electrode fingers is 1 mm and the width of each electrode is 0.7 mm. CNTs were dispersed in isopropyl alcohol and spin coated onto this assembly to create a CNT network between the electrodes. The respective techniques are discussed below. The in-situ heater is used as a mounting stage for sensor device and is shown in fig.-2.10.

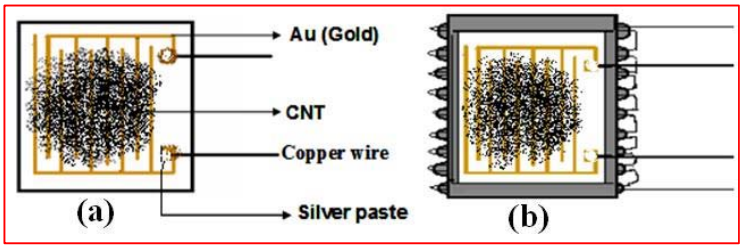

Figure 2.10: Schematic diagram for device fabricated on an alumina template. (a) CNTs are spin coated on gold electrodes and (b) device mounted on the in-situ heater.

2.4.1 Electrode fabrication by DC-Sputtering

Electrode patterns were coated by DC sputtering of gold. A brief description of the instrument detail and deposition procedures is discussed here.

The principle of the coating process involves bombarding a donor material with ionized gas molecules driven by a high applied potential at low pressure. The displacements of atoms from the target are ejected as a result of momentum transfer between the incident ions and the target. These high energy atoms adhere to the recipient material at the anode and create a thin film on its surface [3].

The schematic diagram of the DC sputtering system is shown in fig.-2.11. Here, a 1.5" diameter circular gold disc is used as a target. The whole chamber is grounded. The system is attached to a diffusion pump backed with a rotary pump to create a vacuum. During the coating a target is fixed at the cathode and the substrate with a mask is kept at the anode (ground). A working pressure in the range of 10^{-3} mbar is maintained with flow of argon gas. A voltage of 1000V is applied for sputtering. The Ar ion plasma is accelerated toward cathode, hits the target and transfers its energy to sputter gold atoms that deposit onto the substrate surface. Typically a gold electrode of 200 nm thickness and having dimensions corresponding

to the window present in the shadow mask get coated in 10 min. On to this electrode the substrate, sensor materials are coated by spin coating.

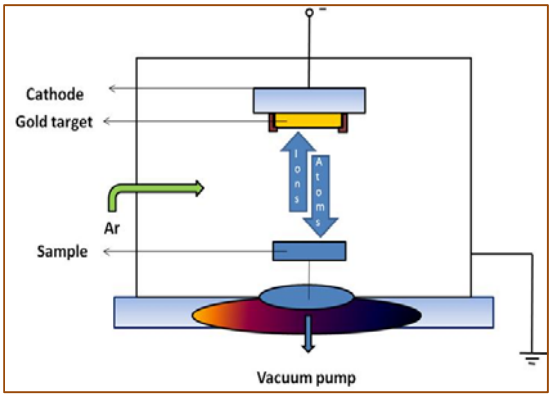

Figure 2.11: Schematic diagram of DC sputtering unit

2.4.2 Spin Coating

Spin coating has been in use for several decades for the application of thin films [4]. A typical process involves droping a small volume of solution onto the center of a substrate and then spinning the substrate at high speed (typically around 3000 rpm). Centrifugal acceleration will cause most of the solution to spread to, and eventually off, the edge of the substrate, leaving a thin film of solution on the surface.

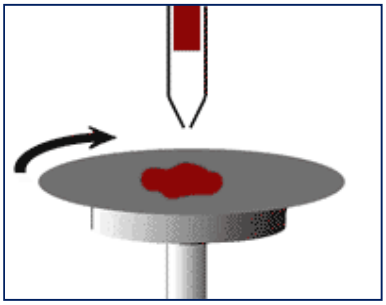

Figure 2.12: Schematic diagram of spin coating unit

A typical spin process consists of a dispensing step in which the CNTs are dispersed in isopropyl alcohol and deposited onto the substrate surface (fig.-2.12). Typically 200 RPM is used to coat the sample on the template. After the dispensing step it is common to accelerate to a relatively high speed (500-2000 RPM) to thin the

fluid to near its final desired thickness. This step can take from 10 seconds to several minutes. The combination of spin speed and time selected for this step will generally define the final film thickness. In general, higher spin speeds and longer spin times create thinner films. Further, the coating thickness is also varied with the number of coating steps with a final drying step to eliminate excess solvents getting into the resulting film.

After achievement of desired thickness, the device is mounted on the sensor stage and all electrical connections are connected. After, annealing at inert atmosphere the device is ready for measurement.

2.5 Measurement of the sensor signal

The electrodes in the sensor are connected with Cu wire using silver paste for external electrical signal processing. The chemiresistive sensor signal output was measured as follows:

- In the first method, the two leads taken out from the device were directly connected to the computer interfaced multimeter (HP, 34401A). Resistance was measured with respect to time using on MS-Office excel add-in.
- In the second method, a specific external voltage (100 mV to 1V) is applied between the electrodes through a constant voltage source and the current was measured in series through the multimeter.
- In the third method, the simultaneous measurement of resistance and temperature with respect to time was carried out by using data acquisition/ switch unit (Agilent 34970A). Here, the output from the device and closely attached k-type thermocouple is connected to the two channels of the data

acquisition unit. Then the signal was collected through a GPIB interface using the LABVIEW program.

2.6 Summary

A hot wall thermal CVD system has been fabricated for CNT synthesis. It consists of a tubular furnace encasing a quartz tube reactor. Gas flow is controlled by MFCs, temperature is controlled by a PID temperature controller and the thyristor arrangement and pressure can be changed by use of an external pumping system to create a high vacuum.

A sensor test facility was fabricated in house. Gas mixing with ppm analyte level was discussed. A sensor device was fabricated on a alumina template. A device made up of a gold electrode was drawn by a shadow mask technique. CNTs were spin coated between electrodes to create an active network. All external connections are made of Cu wire. Inside the quartz reaction chamber, the wires were covered with alumina beads. The data acquisition was achieved through a multimeter, data logger interfaced with a computer.

2.7 References

[1] J. H. Park and T. Sudarshan, *Chemical vapor deposition* vol. 2: Asm Intl, 2001.

[2] H. O. Pierson, *Handbook of chemical vapor depostion (CVD): principles, technology, and applications*: William Andrew, 1999.

[3] K. Reichelt and X. Jiang, "The preparation of thin films by physical vapour deposition methods," *Thin Solid Films*, vol. 191, p. 91, 1990.

[4] L. Scriven, *Physics and applications of dip coating and spin coating* vol. 121: Cambridge Univ Press, 1988.

Chapter-3 Experimental methods

3.1 Introduction

This chapter starts with the synthesis procedure used in the CNT synthesis. A broad outline is given for CNT synthesis that includes catalyst preparation, CNT growth and purification. Further, the procedure followed for decoration of FWCNTs with Pd and SnO_2 are explained. The second part of this chapter deals with the working principle of the analytical techniques employed in the present thesis work for the characterization of the different stages of the CNT growth.

3.2 Carbon nanotube synthesis

Carbon nanotube synthesis by CVD consists of three steps, namely, (1) catalyst loading by impregnation and catalyst processing followed by (2) CNT growth by thermal CVD and (3) purification. This section gives a broad outline of the CNT synthesis procedure with necessary experimental parameters.

3.2.1 Stage-1: Catalyst preparation

The catalyst was prepared through wet impregnation and e- beam deposition and this yielded the catalyst in the form of a powder and mat respectively. Detailed catalyst preparation procedures are discussed below.

3.2.1.1 Catalyst by impregnation

For bulk growth of CNTs, the catalyst is prepared by an impregnation method using two catalyst supports namely zeolite-13X and MgO. The supports used were commercially available zeolite-13X, procured from Fluka (molecular sieve 13X) and

freshly synthesized MgO in the laboratory by heating 0.4 M of $Mg(NO_3)_2$ to 500 ^oC at 2 ^oC /min and keeping at 500 ^oC for 2 hr.

The chosen metal catalysts in this thesis work are Fe, Co, Ni and Mo. To impregnate the support with the required metal catalyst, the corresponding salt, such as, $Fe(NO_3)_3.9H_2O$ for Fe, $Co(NO_3)_2.6H_2O$ for Co, $Ni(NO_3)_2.6H_2O$ for Ni and $(NH_4)_6Mo_7O_{24}.4H_2O$ for Mo were used. To study the synergetic effect, of the catalyst combinations like Fe-Mo, Co-Mo, Co-Ni were also prepared. For that, 2.5 wt% of each metal was taken in the form of the respective salts to impregnate zeolite-13X or MgO in 25 ml of ethanol. Both the solutions were thoroughly mixed by continuous stirring at constant speed for 2 h then sonicated for 30 min to obtain a homogeneous catalyst impregnated support. To carry out impregnation in a basic environment, an ammonia solution was added dropwise to adjust the solution pH to the required value. This mixture was dried overnight at 120 ^oC. The dried sample was powdered by gentle crushing using a mortar and pestle to get the final loaded support for CNT growth.

3.2.1.1.2 Catalyst by coating

Si/SiO_2 is taken as a catalyst support. Here, SiO_2 was grown on Si (0 0 1) by dry oxidation in an ambient atmosphere at 1000 ^oC for one h. This SiO_2 barrier layer is essential to avoid silicide formation by the reaction between catalyst and Si substrate at high growth temperature since it will lead to undesirable deactivation of the catalyst and forbid the CNT growth. A thin layer of catalyst (<10 nm) of Fe or Fe/Mo was deposited on Si/SiO_2 substrate by electron beam deposition. Here 99.9% pure Fe and Mo pellets were used as metal source for e-beam evaporation. Before metal deposition on the substrate, pellets were melted by rastering the e-beam. This step helps to avoid sharp edges and impurities on the metal surface. During coating,

the substrate temperature is maintained at 300 ^{o}C. The e-beam energy is controlled by varying the applied current and voltage. Typical values were 0.05 A and 7.02 kV applied for 2 min. The coating thicknesses of Fe and Mo films were 10 nm and 5 nm, respectively. The description of e-beam deposition system is given in section 3.2.9.

3.2.2 Stage-2: Pre treatment and CNT Growth

The pretreatment steps to make the catalyst and to grow the CNT are carried out sequentially in a thermal CVD reactor. These processes are carried out at atmospheric pressure. A loaded catalyst-support (50 mg) was taken in an alumina boat and encased in a quartz tubular furnace. After purging with pure argon gas (99.999%), the furnace temperature was increased from room temperature to 600 ^{o}C at the rate of 10 ^{o}C/min and subsequently the impregnated catalyst was reduced with ammonia gas for 60 min. The reduction temperature and time were appropriately altered, taking into consideration of the support catalyst interaction which will be discussed in chapter-4. After reduction, the temperature was further raised to the growth temperature (~700-1000 ^{o}C) to enable the growth of CNTs. At this temperature, methane was mixed with argon and fed as a source gas into the bed flow reactor at a fixed ratio using a mass flow controller (MFC) for 30-60 min. After the growth period the system was cooled to RT under an Ar flow.

3.2.3 Stage-3 Purification

The purification includes removal of the catalyst support, catalyst and soot formed in the growth process. The major impurities (support and catalyst) were removed by an oxidation using an acid treatment. Required molar acid solutions were prepared by a standard procedure. The acids used for this process were analytical grade HCl, HNO_3 and H_2SO_4. To optimize the required process, magnetic stirring,

refluxing, sonication and centrifugation were mainly explored. The effect of acid, temperature and time on the purification was studied and reported in chapter-4.

In general, the chosen acid reacts with MgO or Fe to form the respective water soluble salt which can be removed by repeated washing and filtering of the solution. For example, reaction of MgO with HNO_3 occurs as follows,

$$MgO + HNO_3 \xrightarrow{\Delta} Mg(NO_3)_2 + H_2O \quad (3.1)$$

Among the acids used, the reactivity observed towards the sample is as follows HNO_3 < HCl < $1HNO_3{:}3H_2SO_4$. Catalytic activity of H_2SO_4 to produce more nitronium ion (NO_3^+) in the mixture of HNO_3 and H_2SO_4 made it highly reactive. Subsequent to acid treatment the solution was vacuum filtered using a polycarbonate isopore membrane filter (Millipore GTTP) with pore size of 0.22 um. After filtering, the sample was collected in a beaker and kept in an oven at 120 ^oC, overnight for drying.

3.3 Synthesis of decorated FWCNTs

FWCNTs were decorated with Pd and SnO_2 by a soft chemical route. In the first step, functionalization of these FWCNTs was carried out. The purified CNTs (25 mg) were added to a 3:1 mixture of concentrated H_2SO_4 and HNO_3. The mixture was treated in an ultrasonic bath for 15 min and stirred for 1 h. Then, the mixture was vacuum filtered and washed with distilled water until the pH of the filtrate reached 7. The filtered sample was dried at 120 ^oC for 12 h. In the second step decoration with Pd or SnO_2 was carried out.

3.3.1 Pd decoration

For Pd decoration, 5 mg of functionalized FWCNTs was placed in a beaker of deminarlized water and vigorously sonicated to achieve a uniform dispersion. $PdCl_2$

(0.005 M) was added slowly to this well dispersed FWCNT. Subsequently, 50 ml of an aqueous solution of 0.01M $NaBH_4$ was added dropwise in 20 min under ultrasonication to reduce of $PdCl_2$. The mixture was magnetically stirred for 30 min. Finally this sample was filtered and dried at 120ºC for 24 h.

In the reaction, $NaBH_4$ was used as a reducing agent to produce Pd^{2+} from $PdCl_2$. In general, the reduction takes place as shown below,

$$PdCl_2 + 2NaBH_4 \rightarrow Pd^{2+} + 2BH_3 + 2NaCl + H_2 \quad (3.2)$$

Here, BH_3 and NaCl dissolve in water whereas Pd^{2+} gets attached to the FWCNTs through -OH or -COOH group. These groups act as nucleation sites and growth takes place to produce Pd nanoparticles on CNT walls.

3.3.2 SnO_2 decoration

For SnO_2 decoration, 5 mg of functionalized FWCNTs was dispersed in deminarlized water and vigorously sonicated to achieve uniform dispersion. Then 1g of $SnCl_2$ was added slowly to the solution. This resulted in a colloidal solution due to the hydrolysis of $SnCl_2$ to $Sn_4(OH)_2Cl_6$ given by the equation,

$$4SnCl_4 + 2H_2O \leftrightarrow Sn_4(OH)_2Cl_6 + HCl \quad (3.3)$$

To this colloidal solution 5 molar HCl was added drop by drop till the solution became clear. This step is carried out to form Sn^{2+} cations in the solution. These tin ions reacted with dissolved oxygen in water to form SnO_2 as follows [1];

$$2SnCl_4 + O_2 + 2H_2O \leftrightarrow 2SnO_2 + 4HCl \quad (3.4)$$

After staining this solution, the filtered substance is washed thoroughly with distilled water and then dried overnight at 120 ^oC.

3.4 Characterization methods

This section briefly explains the characterization techniques and related studies used to evaluate CNTs.

3.4.1 Scanning electron microscopy

A Carl Zeiss make Supra 55 FESEM and Philips GX 30 ESEM was used for the present study. The system is equipped with energy-dispersive X-ray analysis (EDX) and is capable of qualitative as well as quantitative analysis of relative concentrations of elements present.

The scanning electron microscope (SEM) uses a focused, high-energy electron beam that interacts with the specimen to generate a variety of signals from its surface. Energetic electrons in a SEM interact with a solid sample and produce secondary electrons (SE) used to produce SEM images, backscattered electrons (BSE) gives phase contrast, diffracted backscattered electrons (EBSD) used to determine crystal structures and orientations, photons (characteristic X-rays that are used for elemental analysis), visible light (CL, cathodoluminescence) for studying luminescence under an electron beam and heat. Secondary electrons and backscattered electrons are commonly used for imaging samples [2].

SEM analysis requires use of a vacuum chamber, an accelerated electron beam, multi-sample loadable stage and various detectors. In the electron gun, electrons are produced by a field emission or thermionic technique and an accelerated to a high voltage up to 30 kV. These electrons are focused to a narrow beam and directed on to the sample. The various signals emitted from the sample are detected by appropriate detectors. A Supra-55 FESEM is equipped with an in-lens and Everhart-Thornley (ET) detectors and a peltier cooled EDS detector. The in-lens

detector is located inside the electron column of the microscope and is arranged rotationally symmetric around the optical axis. Due to a sophisticated magnetic field at the pole piece, the secondary electrons are collected with high efficiency. In particular at low voltages and small working distances, images with high contrast can be obtained with this detector. Besides information about morphology and surface topography, the in-lens detector images show the work function difference (e.g., electronic variations) on the sample with high lateral resolution. The ET detector is composed of a scintillator, collector, light pipe and photomultiplier tube. The secondary electrons emitted from the sample are attracted and accelerated towards a scintillator causing photons to be emitted. Photons emitted from the scintillator fall on the photomultiplier tube which amplify the original signal and eventually get collected. Common BSE detectors are solid state detectors and scintillator detectors. These detectors are not responsive to low energy electrons and therefore exclude the SE signal. The solid state detector is based on the principle that high energy electrons striking the silicon produce electron-hole pairs in the material. A bias on the detector separates the electrons and holes and the resultant charges are collected. The intensity of the charge is proportional to the energy of the incoming electrons and the number of electrons striking the detector. The scintillator detector is based on the interaction of BSEs with the detector to produce photons, similar to ET detector. The EDS detector measures the energy of an incoming photon by the amount of ionization it produces in the detector material. Traditionally solid state detectors like liquid nitrogen cooled lithium doped silicon Si(Li) are used. Recent times, Peltier cooled silicon drift detectors (SDD) have been used for higher count rates and without liquid nitrogen cooling. All these detectors separate the characteristic X-rays of different elements into an energy spectrum. The X-rays produced are made to fall on the

detector material and it in turn converts the energy of individual X-rays into electrical voltages of proportional size and the electrical pulses correspond to the characteristic X-rays of the element.

3.4.2 Transmission electron microscopy

A Carl Zeiss Libra 200 TEM was used in the present study. This system was equipped with complementary techniques such as EDS and Electron energy loss spectroscopy (EELS).

Transmission electron microscopy is an unique materials characterization technique that enables simultaneous examination of high resolution microstructural features as well as crystallographic information of the region[3]. It is an electron optical instrument and basically consists of two principal subassemblies: (1) a high energy electron source (eg., LaB_6 or Field emission source) and (2) a host of electromagnetic lenses to control the electron beam and to generate the high resolution image.

In this technique, the entrance surface of a thin foil specimen is illuminated by a high energy (up to 200 keV) parallel electron beam. These electrons may undergo any of several interactions with the specimens such as diffraction by the periodic atomic planes or transmittance through the thin crystal. Images formed using the transmitted electrons are known as bright-field images and images formed using specific diffracted (hkl) beams are known as dark-field images. Using a selected area aperture one can generate diffracted patterns from very small areas of interest. These selected area diffraction (SAD) patterns are useful in identifying the crystal structure, determining a crystal orientation or an orientation relationship between co-existing planes. The wavelength of electrons with energy 100 – 200 keV is of the order of 10^{-3}

nm and consequently the diffraction angles are typically tenths of a degree. For such small angles, θ = sin θ. For first order reflections, the Bragg's law reduces to,

$$n\lambda = 2\,\theta \tag{3.5}$$

Taking the microscope geometry into consideration the Bragg law can be written as $rd = \lambda L$ where r is the distance between the transmitted and diffracted beam, d the atomic interplanar spacing, λ the electron wavelength and L the effective distance from the specimen to the film.

In the case of nanocrystalline materials, high resolution TEM not only provides atomic-resolution lattice images but also chemical information at a spatial resolution of 1 nm or better. The surface defects, planar defects and interface dislocations created by lattice mismatch between nanocrystals can directly be imaged using a high resolution TEM. Nanocrystalline materials give rise to ring SAD patterns as many randomly oriented fine grains contribute to the observed patterns. Thus, to observe morphological features of nanocrystalline materials, TEM is definitely the most useful and effective technique.

3.4.3 Atomic force microscopy

In the present work, an atomic force microscope manufactured by M/S NT-MDT, The Netherlands was used in semi-contact and contact mode to the study surface morphology of catalyst films and CNTs.

Atomic force microscopy is a widely used technique used to study the surface morphology of a smooth film [4]. It is applicable to all categories of materials; metals, semiconductors or insulators. The AFM uses a sharp probe to scan the surface of a specimen and measures the changes in magnitude of force between the probe tip and

the specimen. Fig.-3.1 illustrates the working principle of an AFM. A cantilever with a sharp tip, positioned above the specimen is used to scan the surface. Depending on the separation between the tip and sample, a long range or short range force will dominate the interaction. This force is measured from the bending of the cantilever by an optical lever technique. In this method a laser beam is focused on the back of the cantilever and reflected into a photo detector. The small force acting between the tip and specimen will cause a deflection on the cantilever and this will be detected by a position sensitive photo diode. By raster-scanning the surface and recording the change in force as a function of position, a map of surface topography is easily generated.

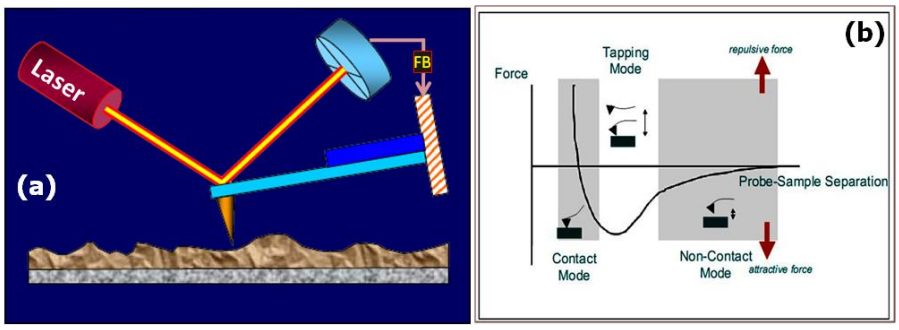

Figure 3.1: (a) Scheme of an atomic force microscope and (b) the force-distance curve characteristic due to interaction between the tip and surface.

The AFM is useful for obtaining three-dimensional topographic information with lateral resolution down to 1.5 nm and vertical resolution down to 0.05 nm. It can operate in gas, ambient and fluid environments and can measure physical properties including elasticity, adhesion, hardness, friction and chemical functionality by incorporating suitable operational gadgetry for such specific operations. The ability of an AFM to achieve near atomic scale resolution depends on three essential

components: i) a cantilever with a sharp tip, ii) a scanner that controls the *x-y-z* position, and iii) the feedback control loop.

The construction of an atomic force microscope requires a force sensor to measure the forces between a small probe and the surface being imaged. A common type of force sensor utilizes the relationship between the motion of a cantilever and the applied force. The relationship is given by the Hook's law

$$F = -k * d \tag{3.6}$$

Here, k is the spring constant and d is the distance at which the cantilever tip bends.

Many AFM modes have used to achieve different objectives. Among them contact, non-contact and tapping modes are commonly used. In the contact mode, electrostatic and/or surface tension forces from the adsorbed gas layer pull the scanning tip toward the surface. It can sometimes, damage samples and distort image data. Therefore, contact mode imaging is heavily influenced by frictional and adhesive forces compared to the non-contact or tapping mode. Non-contact imaging generally provides low resolution and can also be hampered by any contaminant layers which can interfere with the oscillation. Tapping mode AFM was developed as a method to achieve high resolution without inducing destructive frictional forces. With the tapping mode technique, very soft and fragile samples can be imaged successfully. In addition to phase imaging, the tapping mode AFM can be used to analyze components of a membrane.

3.4.4 Thermogravimetric analysis - Differential thermal analysis -

Mass spectrometry (TGA-DTA-MS)

The TGA system used for the present study a Setsys 16/18 (Setaram, France), was equipped with differential thermal analysis (DTA). Material properties like

glass transitions, crystallization, melting and sublimation can be studied by using DTA combined with TGA. Moreover a TGA system can be coupled to a mass spectrometry (MS) for the measurement of partial pressures of various reactive gases [5].

The TGA used had a vertical bottom loading system with provision for flow of inert carrier gas to protect the balance and an auxiliary gas around the specimen. TGA determines changes in sample weight with respect to a change in its temperature. The schematic of the TGA system is shown in fig.-3.2. This commercial thermo-gravimeter consists of four important parts. They are, a sensitive analytical micro balance, a high temperature furnace, gas handling system and a computer for instrument control and data acquisition. Here, the dual range microbalance duel range and can handle samples weighing up to 20 g with a mass resolution of 0.04 microgram. The high temperature graphite furnace rated for up to a temperature of 1750 ˚C as was programmable for desired heating, cooling rate, dwelling time etc., through the user friendly interface program. The temperature program of the furnace is controlled by a precision PID controller.

This system is ideal for studying the thermal decomposition of the materials. The change in weight of the material is due to the making or breaking of chemical bonds, desorption or adsorption of gases with change in temperatures. Moreover, the

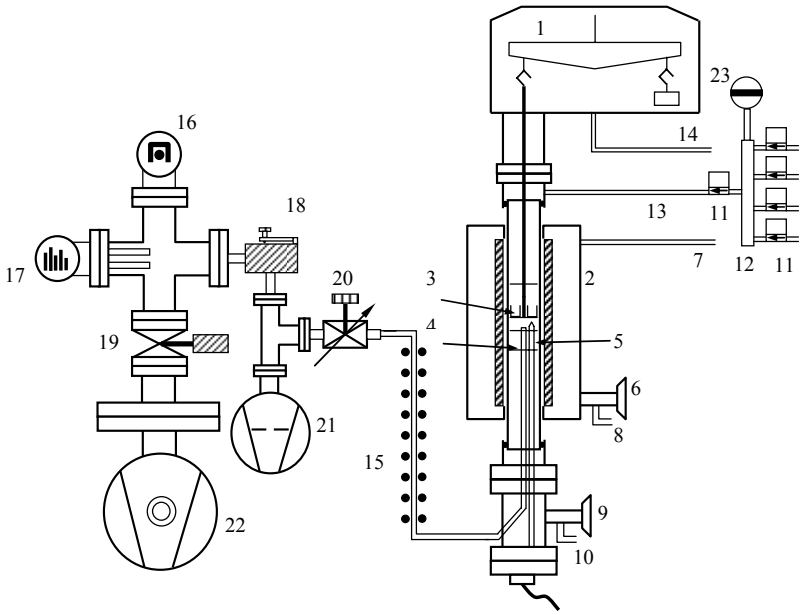

1. Microbalance
2. TGA furnace
3. Specimen in TG/DTA rod
4. Gas take off tube
5. Control thermocouple
6,9. To vacuum pump
7. Furnace protection gas – inlet
8. Furnace protection gas – outlet
10. Carrier & Auxiliary gas outlet
11. Mass flow controllers
12. Gas blender
13. Auxiliary gas inlet
14. Inert carrier gas inlet
15. Gas line to mass spectrometer
16. Magnetron gauge
17. Quadrupole mass analyser
18. Molecular leak valve
19. Gate valve
20. Micrometering valve
21. Rotary pump
22. Turbo molecular pumping unit
23. Baratron

Figure 3.2: Schematic of TGA-DTA-MS system [5].

delivery system with mass flow controllers makes it suitable for use as a vertical-thermal CVD system to grow nanostructures and also an exposure facility for carburization and nitridization studies. By using this system as a synthesis tool, one can get detailed information on the kinetics of reactions and transitions with respect

to temperature and time. A thermo-gravimetric curve represents the characteristic of a given material due to the sequence of physical transitions and chemical reactions in a particular temperature range. In this thesis, the TGA-MS is used for studying the catalytic and thermal decomposition of a methane source gas while DTA was used for studying phase transition of the support materials with respect to temperature.

3.4.5 Raman spectroscopy

In the present work, a Raman spectrometer (inVia, Renishaw, UK) was used with a Peltier cooled CCD detector. The electron and phonon structure of CNTs were studied using multiple laser excitation such as the 325 nm (UV) of He-Cd, 514.5 nm of Ar^+ and 785 nm of a diode with 2400, 1800 and 800 gr/mm grating, respectively.

Raman spectroscopy is a type of vibrational spectroscopy primarily concerned with the qualitative and quantitative evaluation of the structural property and transformation of materials at the molecular level [6]. In this technique, the sample which may be a gas, liquid or solid is irradiated with an intense beam of monochromatic radiation of wave number (υ_0) in the ultra violet, visible or infra-red regions of the electromagnetic spectrum. Most of the radiation is scattered without a change in wave number. This is the usual Rayleigh scattering. However, a small part of the scattered radiation (~ 10^{-5} of the incident intensity) is scattered with the wave number $\upsilon_0 \pm \upsilon_m$ where, υ_m is characteristic wave number of molecular vibration that undergo excitation. The $\upsilon_0 - \upsilon_m$ and $\upsilon_0 + \upsilon_m$ scattered radiation components are known as Stokes and anti-Stokes lines, respectively. The Raman effect is often thought of as a vibrational or rotational frequency modulation of the electric field of the incident radiation. The basic instrumentation of a conventional Raman spectrometer is shown in fig.-3.3. It consists of a monochromatic radiation source (Laser), spectrometer (dispersing device), detector and data acquisition unit.

The selection rule for Raman scattering is based on molecular polarizabilities and induced dipoles which operate in infrared absorption bands and depends on dipole moment changes. The position and width of the Raman bands of materials are related to their vibration and structural properties. Thus a better understanding of the Raman spectra of CNTs can be obtained by examining the local structure and electronic environment of its constituent atoms along with associated crystallographic knowledge [7].

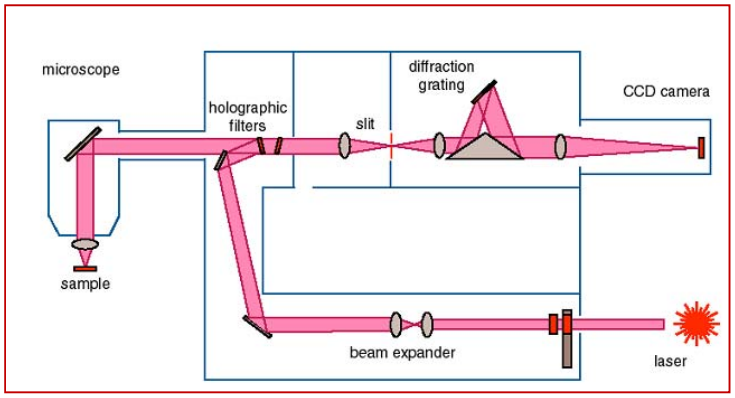

Figure 3.3: Schematic representation of Raman spectrometer

3.4.6 Fourier transform infra red spectroscopy

In this thesis, an ABB MB3000 FT-IR laboratory spectrometer was used for studying the vibrational properties of CNTs and functional groups. It works in the spectral range of 485- 4000 cm^{-1} with a 0.7 cm^{-1} resolution. For this study, CNTs in the form of powder was mixed with KBr and uniaxially pressed to get their IR transparent pellets.

In infrared (IR) spectroscopy, infrared radiation is passed through the sample. A part of the infrared radiation is absorbed by the sample from molecular vibrations and the rest is transmitted. The resulting spectrum presents the molecular absorption and transmission creating molecular finger prints of the allowed fundamental modes

in the sample and functional groups. Fourier Transform Infrared (FT-IR) spectroscopy was developed in order to overcome limitations like a slow scanning process encounterd with dispersive instruments. It is a method for measuring all of the infrared frequencies simultaneously, rather than individually [8].

In a normal instrumental process, infrared energy is emitted from a glowing black-body source. This beam passes through an aperture which controls the amount of energy presented to the sample. Then the beam enters the interferometer where the spectral encoding takes place. The resulting interferogram signal then exits from the interferometer. The beam enters the sample compartment where it is transmitted through or reflected off the surface of the sample, depending on the type of analysis to be accomplished. This is where the specific frequencies of energy are found to be characteristic of the sample absorption process. The beam finally passes to the detector for the final measurement. The measured signal is then digitized and sent to the computer where the Fourier transformation takes place and the final result is presented in a graph of intensity vs wave number.

3.4.7 X- Ray Diffraction

The room temperature powder diffraction pattern of all the samples studied in this thesis were recorded using a STOE diffractometer operated with a power of 40 kV and 30 mA, in the Bragg-Brentano geometry. The X-ray radiation used was the $Cu - K_{\alpha}$ line. The lattice parameters from the XRD pattern were extracted using a STOE and PCW programs [9].

XRD is a powerful tool to examine the crystal structure of the materials [10]. The basic components of an XRD instrument are the X– ray source, detector and control unit. The X-rays, with a wavelength comparable to that of the lattice spacing,

fall on the sample and interacts with the atoms in the lattice, causing scattering in all directions. When the sample is crystalline and has a periodic arrangement of atomic planes, the X-rays scattered by each plane constructively interfere and result in interference maxima at particular angles. This happens when the path difference of the scattered X- rays from successive atomic planes forms an integral multiple of the wave length (λ) of the X-ray. The condition for the formation of diffracted radiation is known as Bragg's law of diffraction and is expressed as

$$n\lambda = 2d \sin\theta \qquad (3.7)$$

where, λ is the wavelength of the X-ray used (normally Cu Kα, λ = 1.54056 Å), θ is the diffraction angle and d is the lattice spacing. A schematic view of this process is shown in fig.-3.4.

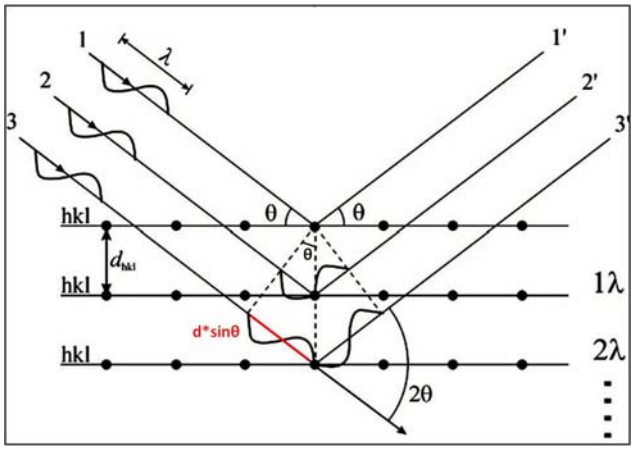

Figure 3.4: The schematic representation of conditions for Bragg's law of diffraction [10].

Diffraction (i.e. constructive interference of the scattered X-rays) will occur if the Bragg condition (eq. 1) is fulfilled and the scattering vector K is parallel to the normal of the hkl-planes. By scanning crystalline samples in search of interference peaks, one can obtain information about the lattice parameters, strain, texture, etc.

In a diffraction pattern, the recorded intensity is usually plotted against the diffraction angle 2θ. Grain size is calculated from the XRD data using the Scherer's formula.

$$D = \frac{0.9\lambda}{\beta \cos\theta} \tag{3.8}$$

where, D is the size of the grain, λ is the wave length of the X-ray, $\beta = \sqrt{\beta_g^2 - \beta_s^2 + \beta_i^2}$, β_g is the FWHM calculated from the diffraction profile, $\beta_s = 4\varepsilon \tan\theta$ (the strain broadening component), $\varepsilon = \Delta a/a$ and β_i is instrumental broadening.

3.2.8 Resistivity at ambient pressure and field

The sample is mounted on an oxygen free high thermal conductivity (OFHC) copper platform on which a pre-calibrated Si diode sensor is firmly attached using GE-varnish for monitoring the temperature. The sample is stuck to the other side of the OFHC Cu platform, positioned at the back of the diode sensor, with proper electrical insulation. Four contacts are made on the sample, two for applying current and two for measuring voltage drop, using a silver paint. The leads of the sensor and the sample are soldered onto a connector pad, from which connections to the corresponding current sources and nano voltmeters are already made. The temperature variation of 300 K to 4.2 K is achieved by inserting the dipstick mounted with the sample and sensor, into a liquid helium storage Dewar, containing the cryogen thus making use of the natural thermal gradient of the Dewar. During the insertion of the dipstick, data from the sample and the sensor are simultaneously collected using a Lab-View program through a GPIB interface with a computer. The sequence of data acquisition is as follows. Initially a known minimal current (I) is passed through the sample leads using a DC current source. The Si diode is activated with 10 μA current

with another similar current source. The sensor voltage is first read, from which the measurement temperature is determined from a set of pre-calibrated coefficients. Then the sample voltages are read with both forward (I^+) and reversed currents (I^-), to eliminate contributions from thermo-emf and from these voltage values the sample resistance is determined as $R_S=V_S / I_S$ where $V_S=V_S^{I+} - V_S^{I-}$. This process of data acquisition is repeated every second while the dipstick is slowly inserted into the liquid helium Dewar to achieve the temperature variation from 300K to 4.2K. After each data collection, the data are written onto a file and stored for further analysis. The measurement is generally repeated in the warming run by raising the dipstick and repeatable data could be obtained as in the cooling run, by the slow movement of the dip-stick and ensuring good contacts were made on the samples. A photograph of the sample holder and connection ports is shown in fig.-.3.5.

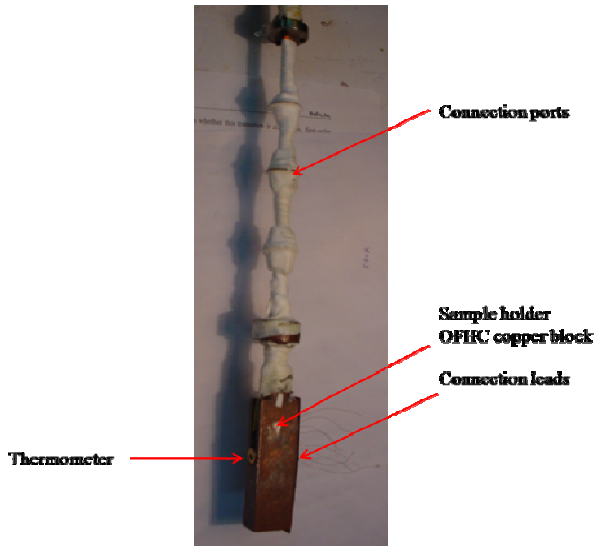

3.2.9 e- Beam deposition

The e- beam deposition system used for coating thin films in this study was indigenously designed and locally assembled. It consists of a 270 degree multi turret

and e-gun and an additional RF magnetron sputter source with Temescal SIMBA power supply (12 kW, 10 kV).

Electron beams are used when required temperatures are too high for thermal evaporation. Thermal emission of electrons from a tungsten filament source is used to heat samples to high temperatures. Magnetic fields and rastering used to steer the electron beam by 270^{o} onto a metal source. As shown in fig.-3.6 this design allows the shielding of the tungsten filament and prevents contamination. The Fe and Mo coatings used in the present study were coated by varying the applied voltage and current as discussed in section-4.1.

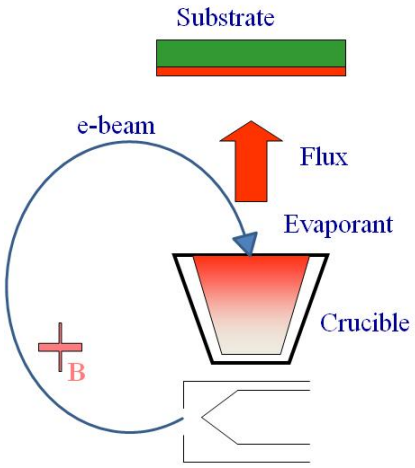

Figure 3.6: Schematic diagram of electron beam deposition system

3.3 References

[1] H. T. Fang*, et al.*, "Synthesis of tin (II or IV) oxide coated multiwall carbon nanotubes with controlled morphology," *The Journal of Physical Chemistry C,* vol. 112, pp. 5790-5794, 2008.

[2] W. Zhou and Z. L. Wang, *Scanning microscopy for nanotechnology: techniques and applications*: Springer Verlag, 2007.

[3] D. B. Williams and C. B. Carter, "The Transmission Electron Microscope," *Transmission Electron Microscopy,* pp. 3-22, 2009.

[4] N. Tomczak and K. E. J. Goh, *Scanning probe microscopy*: World Scientific Pub Co Inc, 2010.

[5] M. Kamruddin*, et al.*, "Thermogravimetry-evolved gas analysis-mass spectrometry system for materials research," *Bulletin of Materials Science,* vol. 26, pp. 449-460, 2003.

[6] J. R. Ferraro*, et al.*, *Introductory raman spectroscopy*: Academic Pr, 2003.

[7] M. S. Dresselhaus*, et al.*, "Raman spectroscopy of carbon nanotubes," *Physics Reports,* vol. 409, pp. 47-99, 2005.

[8] P. R. Griffiths and J. A. De Haseth, *Fourier transform infrared spectrometry* vol. 171: John Wiley & Sons, 2007.

[9] W. Kraus and G. Nolze, "Powder Cell for Windows 2.3 (1999)," *Federal Institute for Materials Research and Testing, Berlin, Germany*.

[10] B. D. Cullity and S. R. Stock, *Elements of X-ray Diffraction* vol. 3: Prentice hall Upper Saddle River, NJ, 2001.

Chapter-4 Study of the Synthesis of Carbon Nanotubes by Thermal CVD

4.1 Introduction

The unique properties of carbon nanotubes in terms of their electronic, mechanical and thermal applications compared to other existing materials have attracted researcher's attention over the last two decades [1-3]. Potential applications based on CNTs demand tubes of a specific type in large quantities. This emphasizes the study of nanotube growth, under the influence of various chemical and physical parameters. However, the current understanding of the growth mechanism of CNT is multifold, be it for arc discharge, laser ablation or CVD. In heterogeneous catalytic method, the growth, mechanism is widely discussed using the vapor-liquid-solid (VLS) model [4-5]. Magrez et al., [6] proposed polymerization of the aromatic carbon rings to give tubular CNT formation. In catalyst free CNT growth, the growth mechanism is explained on the basis of vapor-solid (VS) model [7].

From a mass application perspective, the catalytic growth of CNTs by CVD is a most promising synthesis technique in view of the lower temperatures required, good control on deposit morphology, capability of scaling up the process, growth on a specific area of interest etc., [8-11]. In this process, the catalyst is dispersed over a suitable support to control morphology and inhibit agglomeration at high growth temperatures. Though catalyst supports are considered as passive candidate during catalytic CNT growth process and the recent observations have clearly show that the growth of CNTs is greatly influenced by catalyst supports such as Al_2O_3, MgO, TiO_2, ZnO, zeolite, SiO_2 and CuO [12-14]. In this chapter the role of the physical and chemical properties of the support material in the context of CNT growth has been

studied in this chapter by using two well known supports, zeolite-13X and MgO, with Fe as catalyst and methane as carbon source.

Though monometallic Fe acts as a catalyst for CNT growth, the in-situ TGA study shows that deactivation of catalyst takes place over a period of time. In addition, CNTs grown using Fe alone as catalyst results in higher diameter with many walls. To enhance the yield by sustained catalytic activity with tunable diameter, bimetallic catalysts were studied. From the present study it is shown that a combination of Fe with Mo gives well defined tubular growth. Further it showed sustained growth for a long time with reduced diameter. These CNTs are called few walled CNTs (FWCNTs). The as grown FWCNTs were used for further studies after subjected to crucial purification process. The purification methods were carried out through a wet chemical route by a multistep process. This process yields higher pure and good quality carbon nanotubes.

This chapter deals with the crucial steps involved in the synthesis of CNTs by thermal CVD. The stages involved in this process such as catalyst preparation, effect of support catalyst interaction, FWCNT growth and purification are described.

4.2 Choice of support material: zeolite-13X and MgO

We have chosen two catalysts supports, namely zeolite-13X (Molecular sieve 13X, Union carbide) and MgO. The choice of these well studied materials with their contrasting physical and chemical properties could aid in understanding their influence on CNT growth parameters. Both of these support materials significantly differ in their morphology, thermal stability, porosity and surface chemistry.

Zeolite-13X is the sodium form of the aluminosilicate and has a pore opening of 10 Å. The chemical formula is, $Na_2O.\ Al_2O_3.\ (2.8\pm0.2)SiO_2.\ (6\sim7)H_2O$. The zeolite structure consists of silicon and aluminum bonded through an oxygen bridge to form a

porous structure, which possesses uniform porous channels and cavities with a large inner surface area. Besides Si, Al and O the structure contains metallic cations of low positive charge and chemically combined water molecules. Although these water molecules could be released upon heating, the crystal structure does not change. Moreover, it possesses three dimensional frames of networks with a pore volume of 28%-35% fraction of total volume, so that it is able to adsorb large number of molecules. Due to its homogeneous pore size distribution and highly adsorptive selectivity, it is a powerful adsorbent of catalyst and acts as catalyst support [15-16]. There are many reports on successful growth of carbon nanotubes using zeolite-supported catalysts by impregnation method with unsaturated carbon sources. The smallest CNTs with diameter close to the theoretical limit of 4.2 $\pm$ 0.2 Å were synthesized by pyrolyzing tripropylamine in the channels of the zeolite ($AlPO_4$-5) [17]. Since, SWNTs are formed inside ordered channels; they are highly aligned, isolated and uniform in size. Thus they resembles an ideal 1D system [18].

MgO is a highly ionic crystalline solid with interesting properties such as high temperature stability and chemical inertness. It possesses a simple stoichiometry and crystal structure and can be prepared as particles with desired sizes and shapes [19]. Catalytic properties of MgO powders depend mainly on the crystallite size, specific surface area, structural defects and acidic-basic site concentration. The MgO can be used as a catalyst support in various forms: porous powered material, nanoparticles or thin film. Though it lacks a controlled self assembled periodic porous structure like that of zeolite-13X, the importance of MgO as an efficient catalyst is attributed to its chemical properties.

In the present study, MgO was freshly synthesized in the laboratory by heating 0.4M of $Mg(NO_3)_2$ to 500 ^oC at 2 ^oC /min and kept at 500 ^oC for 2 hr. MgO is

found to be an attractive alternative metal oxide support due to its exceptional catalytic activity for CNT synthesis and ease of purification by mild acid treatment [20-21].

4.3 Catalyst preparation

Transition metals such as iron, cobalt and nickel are widely used as catalysts for the growth of CNTs [8]. Growth of CNTs depends on the catalyst particle size and morphology. The diameter of the tube is mostly proportional to the catalyst size and the growth rate is inversely proportional to the size of the catalyst. Hence, to achieve isolated CNTs of uniform size, the catalysts have to be dispersed on the catalyst support in the form of nanoparticle and their agglomeration at high growth temperatures should also be avoided [22-24]. In the bulk production of CNTs, the introduction of metal precursors onto a suitable support can be accomplished by several, established methods. Common methods include: (i) impregnation, which involves deposition of a metal precursor onto a support, typically from an aqueous solution (ii) co-precipitation, in which the support and metal precursor are simultaneously precipitated from solution, (iii) ion-exchange, as commonly used for the preparation of zeolite supported catalysts (iv) sol-gel method and (v) physical deposition [8, 25]. Each method has its own advantages and disadvantages.

Due to simplicity, impregnation is routinely used for the preparation of catalysts. Two different modes of impregnation are practiced: wet impregnation and incipient wet impregnation. In wet impregnation, the support material is brought into contact with a solution containing a large excess of metal precursors. By evaporation of the solvent, optional calcinations and reduction, the final catalyst is impregnated on the support. In general, the wet impregnation results in the catalyst being dispersed inside the pore as well as on the surface of supports as large particles.

In this thesis, for bulk production of CNTs, the impregnation method is used for catalyst preparation as discussed in chapter-3.

4.4 CNTs growth on zeolite-13X and MgO

The effect of catalyst support during CNT synthesis was studied by using zeolite-13X and MgO supports. In brief, the initial step was impregnation of the Fe catalyst (2.5 wt %) with on catalyst supports. Sub sequentially reduction of the catalyst in an NH_3 atmosphere at 600 ^oC followed by CNT growth at 900 ^oC using methane with a CVD reactor as mentioned in Chapter-3. The effect of process parameters on the CNT synthesis are discussed in the forth coming section.

4.4.1 Optimization of process parameters

The SEM images of CNTs grown on MgO and zeolite-13X supports at different methane to Ar flow ratios are shown in figs.-4.1&4.2, respectively. In these figs.- a, b and c correspond to CNTs prepared using methane and argon ratio of 1:20, 2:20 and 3:20, respectively.

Images show uniform and dense growth of CNTs on MgO support exposed to methane at 900^oC. The variation in CNT growth as seen in these images suggests that an optimal dilution is required to prevent soot formation and helps to sustain the active catalyst for the growth of CNTs. Combined observations of SEM and net weight gain in Fe-MgO after CNT growth shows that the optimal methane to argon ratio is 2:20.

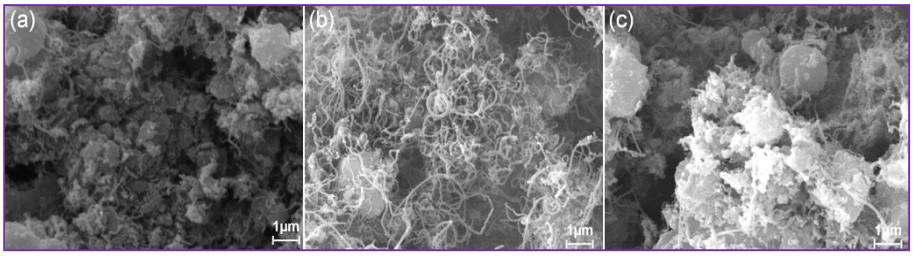

Figure 4.1: SEM micrographs of the as grown CNTs at different methane to argon ratio prepared on MgO support (a) 1:20 (b) 2:20 and (c) 3:20.

In the case of zeolite-13X, under similar growth conditions mixing a ratio of 1:20 and 2:20 shows no tube formation but only carbonization which was ascertained by elemental analysis from energy dispersive spectra (fig.-4.2). Here, the increase in methane concentration only increased the carbonization on the metal impregnated zeolite-13X surface. However, the samples exposed to a higher methane concentration, i.e., in the ratio of 3:20, showed formation of a few fiber like carbon nanostructures (inset fig.- 4.2(c)). Here, it should be noted that zeolite-13X is specified as self assembled mesoporous structure with a 10 Å pore diameter. Still the observation of high growth of CNTs on MgO whereas the inhibition of the same in porous zeolite-13X necessitated further investigation that is discussed in the following section.

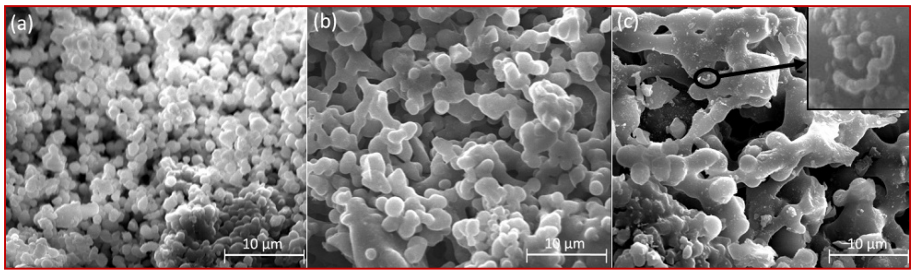

Figure 4.2: SEM micrographs of the zeolite-13X support after CNT growth using different methane to argon ratios (a) 1:20 (b) 2:20 and (c) 3:20. Inset in (c) depicts the magnified spot of the circled area for the growth of the fiber like carbon nanostructure.

The nature of the products grown on these two different porous supports was studied by Raman spectroscopy. Raman spectra of samples grown with a methane to argon ratio 2:20 are shown in fig.-4.3. Raman measurement provides a means to distinguish a variety of carbon materials, by their physical properties based on the ratio of sp^2 to sp^3 hybridization. In addition, Raman spectroscopy also reveals information on the electronic structure and defects in the CNTs. In general, the

Raman spectrum of CNTs shows two prominent peaks that represent G and D bands. Here, the G band represents the in plane vibration of a sp^2 network of carbon atoms and the D band indicates the presence of disorder in the graphite structures. In CNTs, the tubular formation from planar sp^2 carbon structure induces strain in the lattice network. This lattice strain manifests as a shift in G band for SWCNTs, whereas in higher diameter MWCNTs where the strain is significantly less the Raman signatures resemble that of graphite [26-27].

The Raman spectrum acquired for CNTs grown on the MgO support is shown in fig.-4.3a. A strong G band at 1580 cm^{-1} represents the tangential stretching mode of highly oriented pyrolytic graphite. The peak at 1349 cm^{-1} corresponds to D band that originates from crystalline disorder and lattice imperfections in curved graphene sheets.

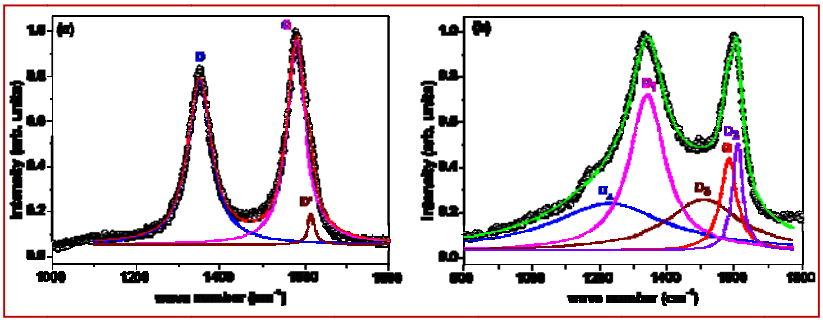

Figure 4.3: Raman spectra of samples prepared with a methane to argon ratio of 2:20 over (a) Fe -MgO (b) Fe- zeolite-13X sample.

In the case of zeolite-13X samples the spectrum acquired after surface carbonization is shown in fig.-4.3b. It can be deconvoluted in to five Lorenzian profiles with their peaks at 1583, 1341, 1609, 1508 and 1227 cm^{-1} corresponding to bands labeled G, D_1, D_2, D_3 and D_4. These are bands typical of soot formation confirming surface carbonization [28].

A nice correlation between the Raman spectra and SEM morphological features of these graphitic phases clearly shows that growth of CNTs takes place only on Fe-MgO. Under similar conditions mere soot formation takes place on Fe-zeolite-13X support. Further experiments were carried out to investigate this anomaly and the mechanism that hinders the formation of CNTs on zeolite-13X. In this thesis, CNTs grown using Fe-MgO were utilized for subsequent studies.

4.4.2 Effect of thermal stability of support materials

From the Raman and SEM observations, it is evident that MgO supports the growth of CNTs whereas zeolite-13X impedes the same. While both of them posseses their inherent pore structures, the growth of CNTs only on MgO and not on zeolite-13X is rather surprising. Intuitively, one can speculate that the initial conditions during the growth of CNTs could be a deciding factor. Hence, the experiments were carried out to monitor independently the thermal stability of these porous support materials by DTA up to a maximum temperature of 1000 ^{o}C in argon atmosphere at a heating ramp of 10 ^{o}C/ min.

The DTA data plotted for zeolite-13X (fig.-4.4a) shows two strong exothermic peaks at ~845^{o}C and 950^{o}C suggesting that over the investigated temperature range the zeolite-13X undergoes two crystalline structural transformations. The onset of the first high-temperature exothermic peak at T~800^{o}C, is attributed to the microstructural collapse of the zeolite-13X framework, and indicates its poor thermal stability [29-31]. This first exothermic peak represents the phase transformation from faujasite to carnegeite and the second peak at 940 ^{o}C pertains to structural transformation from carnegeite to nepheline [32]. These crystalline phase transformation in zeolite-13X are further confirmed from their respective XRD pattern as shown in fig.-4.5 and found to match well with the reported JCPDS data.

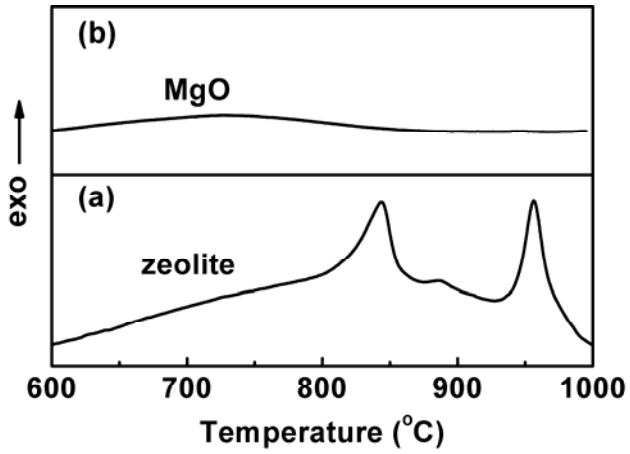

Figure 4.4: DTA of bare zeolite-13X and MgO templates. (a) Two strong exothermic peaks show the structural change in zeolite-13X through phase transformation. (b) MgO is stable throughout the temperature range.

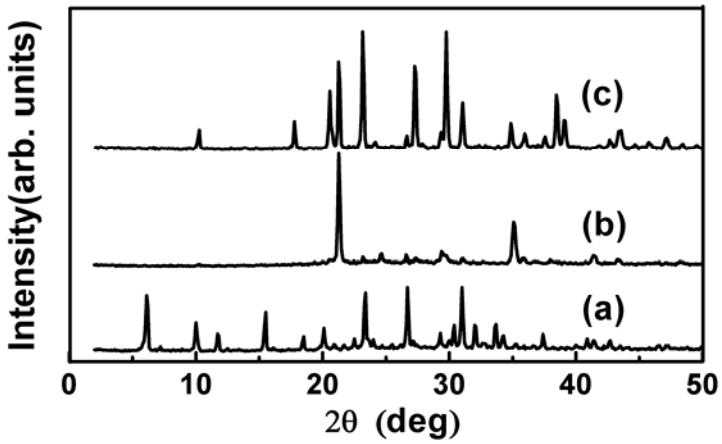

Figure 4.5: XRD pattern showing the structural transformation in zeolite-13X (a) at room temperature (b) heat treated to 850 ^{o}C and (c) heat treated to 950 ^{o}C. The XRD results are well matched with reported peak positions of JCPDS card no 39-1380, 11-0220 and 35-0424 for the faujasite, carnegeite and nepheline structure of zeolite-13X, respectively.

In essence, the micropourous structure in zeolite-13X collapses even before reaching the growth temperature of the CNTs, via the crystalline phase transition and this causes a major setback for the growth of CNTs by potentially inhibiting the catalyst from interacting with methane in this thermal window. In addition, it is also found, even at temperatures below this structural phase transformation, that only carbon deposits are found and no CNT growth. At the same process conditions, carbon deposits found higher on Fe-MgO compared to Fe-zeolite-13X. The low yield of carbon may be due to the partial coverage of the pores of the zeolite by the formation of soot during the initial stages. To address this aspect and to quantitatively estimate the yield of carbon on zeolite-13X, the weight gain measurements during the growth of CNTs was carried out by TGA-MS.

In the case of Fe-MgO, the dense formation of CNTs indicates that the most optimal temperature for the growth of CNTs is around 900 ^{o}C. As there is no structural or phase transformation, as shown by DTA, MgO is thermally quite stable over this temperature window (fig.-4.4b). This in turn proves the superiority of MgO as a catalyst support material when compared to zeolite-13X for the synthesis of CNTs especially while using, source gas like methane which requires a higher cracking temperature. Hence, the study of structural aspects of the catalyst support material and the cracking temperature of methane becomes essential.

4.4.3 In-situ monitoring of the catalytic cracking of methane using TGA- MS

To substantiate the above observations on the growth process and to understand the chemical activity of the catalyst support material in methane decomposition over various stages of CNT growth, a combined TGA-MS system was used. Fig.-4.6 shows the typical TGA-MS spectra of the thermal decomposition of methane in the absence of any catalyst. It shows the mass spectrometric signal of evolved gases as a

function of temperature. A small rise in the hydrogen signal around 930 ^{o}C (shown with an arrow in fig.-4.6) indicates the initiation of thermal decomposition of methane which further increases appreciably at temperature above 1050 ^{o}C.

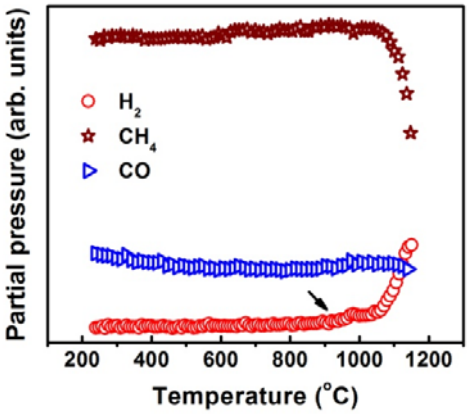

Figure 4.6: Mass spectrometry signal of H_2, CH_4, and CO during the thermal decomposition of methane in the absence of catalyst and catalyst support.

Having studied the thermal stability of the support material and the unaided decomposition of methane gas, further studies were extended to analyze the entire growth process of CNTs by simulating the exact conditions in the TGA-MS system. In this experiment, TGA was used to understand the chemical reaction of Fe-MgO/zeolite-13X with methane under a programmed temperature ramp. The weight gain was monitored online and the corresponding evolved gases were recorded by mass spectrometry (MS). To start with, the first step of catalyst reduction is initiated at 600 ^{o}C by passing ammonia over the zeolite for 30 min. This step is identical to the first step in the growth process of CNTs. Then, a mixture of methane and argon in the ratio of 2:20 was fed into the TGA furnace through MFCs. The weight gain and the corresponding evolved gases during the reaction are monitored in the temperature range of 700-1150 ^{o}C and the spectra are shown in fig.-4.7&4.8. For Fe-MgO system (fig.-4.7) the weight gain starts above 750 ^{o}C and the corresponding MS signal shows

methane decomposition as heralded by hydrogen evolution. Methane cracking at this temperature is due to catalytic decomposition which takes place at a relatively low temperature contrary to the thermal decomposition which noticeably started from 930 ^{o}C onwards as observed in the earlier experiment. Above 750^{o}C, the rate of weight gain is initially high and then slows down due to catalyst deactivation owing to soot formation that covers the catalyst. However, above 1000^{o}C irrespective of the deactivation of catalyst hydrogen evolution is appreciably high due to the thermal decomposition of methane.

On the other hand in zeolite-13X, in (fig.-4.8) the catalytic decomposition of methane could not be observed. However, as in the case of the unaided methane cracking reaction, noticeable hydrogen evolution started at 930^{o}C and instead of a weight gain, a weight loss was observed in the TGA signal. A careful analysis of this aspect reveals a increase in CO concentration. This may be due to the reaction of carbon with lattice oxygen of the impregnated iron oxide which may be partially reduced. To establish the origin of oxygen is only from the unreduced catalyst and not from the compounds of zeolite-13X, further experiments were carried out on bare zeolite-13X and MgO with methane and the inferences are discussed below.

The present study also addresses some of the earlier reported issues pertaining to Fe-zeolite-13X as a catalyst support for growth of CNTs [33-35]. The issues are: (1) use of Fe-zeolite-13X with acetylene gas yielding MWCNTs having a wide distribution of tube diameters, (2) growth of CNTs observed only on the external surface of the zeolite-13X but not from the pores and (3) Kumar and Ando [36] observation that a catalyst of lower loading (below 2.4 wt%) in the zeolite-13X did not yield any CNTs. Our investigations using the TGA-MS system provides some of the possible reasons for the above mentioned issues.

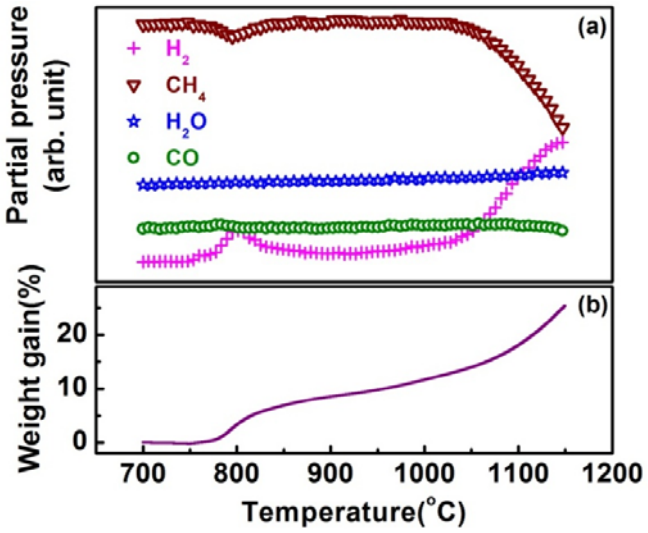

Figure 4.7: (a) Mass spectrometry signal of H_2, CH_4, CO and H_2O (b) with the corresponding weight gain from TGA measured during programmed thermal ramping of Fe-MgO powder under controlled feeding of the carrier gas mixture (methane to argon in the ratio 2:20).

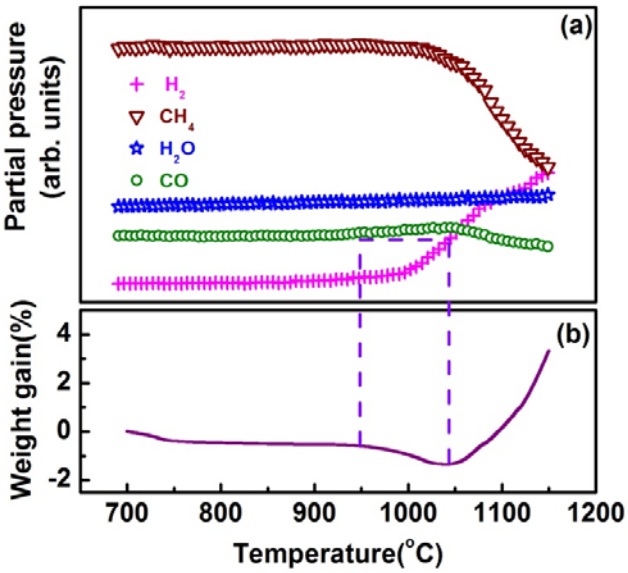

Figure 4.8: (a) Mass spectrometry signal of H_2, CH_4, CO and H_2O (b) with the corresponding weight gain from TGA measured, during programmed thermal ramping of Fe-Zeolite-13X powder under controlled feeding of carrier gas mixture (methane to argon in the ratio 2:20).

In zeolite-13X at a lower loading the Fe catalyst is preferably trapped inside the pore structures which are the active sites in zeolite-13X. Although the catalyst inside the 1 nm pores can produce SWCNTs, energetically the growth is favored only at higher temperature but by then the zeolite-13X loses its porous structure due to the structural transformation. However, even below this temperature, no appreciable methane cracking takes place as we have seen earlier that Fe-zeolite-13X does not act as a catalyst for methane decomposition. Above 930^{o}C, the complete reduction of iron oxide occurs due to the hydrogen generated from thermally decomposed methane. This process starts during the second crystalline transformation of Fe-zeolite-13X system and a 4% weight gain is observed up to 1150^{o}C due to carbon sedimentation. In the catalyst reduction step, the reducing nature of ammonia and its nascent hydrogen production at elevated temperature completes the reduction of iron oxide to produce active catalysts. The observation shows that the impregnated iron oxide in zeolite-13X is not fully reduced to produce active Fe catalyst during the initial ammonia treatment.

To understand the carbon deposition on bare zeolite-13X and MgO supports, the methane cracking reaction was investigated on these supports without catalyst by TGA-MS. The weight gain data is shown in fig.-4.9. In structurally stable MgO, the weight gain due to sedimentation of carbon from thermal decomposition of methane starts at 930 ^{o}C and attains a maximum at 1050 ^{o}C. Whereas, in the case of zeolite-13X observable weight gain starts only around 1050 ^{o}C by which it has already lost its porous nature. Though the weight gain continues up to 1150 ^{o}C, the net weight gain is only 0.6%. Additionally, no weight loss from bare zeolite-13X over this temperature range is observed. This confirms that the weight loss observed in loaded zeolite-13X and CO evolution are only due to partial reduction of iron oxide. From the above

observations and analysis it is clear that catalyst availability and its activity are considerably influenced by the nature of the support in the CNTs growth process temperature window.

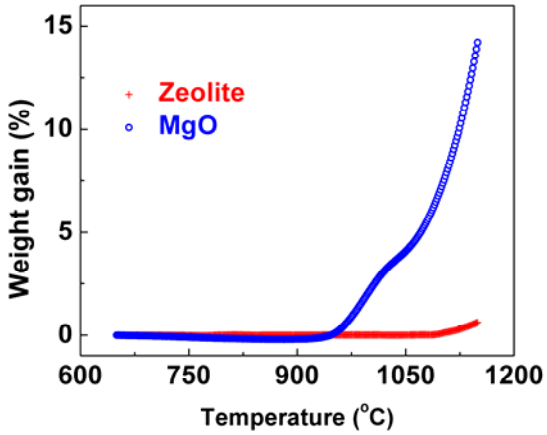

Figure 4.9: Weight gain observed from the TGA signal during programmed thermal ramping of MgO and zeolite-13X powder with controlled feeding of reactant methane to argon ratio 2:20.

4.4.4 Tuning of catalytic activity: Effect of physical and chemical properties

To establish the impact of the catalyst-support interaction and thermal stability of the support material in the cracking methane, the following experiments were carried out on Fe-zeolite-13X. The catalyst loading was increased from 2% to 5% in order to increase the availability of the catalyst on the zeolite surface. Further, the NH_3 treatment time was extended from 20 min to 2 hr to enhance catalyst reduction and the growth at 800 ^oC. From SEM observations as shown in fig.-4.10a, it is found that the number density of CNTs is very low but the image clearly shows the tubular growth of CNTs on zeolite-13X. This suggests, while a higher loading enhances the growth of CNTs, there exists some other parameter apart from catalyst loading and thermal stability that hinders the yield as compared to MgO. Since the growth is carried out at temperature below the structural collapse, the porosity and stability of

the support can be ruled out as the control parameters. A possible explanation can be invoked the chemical nature of the zeolite and its isoelectric point which is reported to be around 4-5 but 12 for MgO [37-38]. It depends on the Si/Al ratio and hence the alkaline sites are less when compared to that of MgO.

Taking a clue from this, the catalyst impregnation on zeolite-13X was carried out in a basic environment at pH-12 by use of liquid ammonia. This treatment aids in the increase of Lewis base sites in the support, which is observed to be a necessary condition for the catalyst support to enhance the growth of CNTs. With this increased basic nature of zeolite-13X support, the CNT growth was repeated using identical conditions and the growth of CNTs was then observed as shown in fig.-4.10b. This observation supports the requirement of polymerization of aromatic rings of carbon for the growth of CNTs which is suggested by Magrez et al., [6]. Further, the growth of CNT under similar condition at 900 ^{o}C was inhibited as can be seen from fig.-4.10c and energy dispersive spectra analysis shows only carbon sediment. The rate of weight gain obtained at 800 ^{o}C and 900 ^{o}C by in-situ TGA are 1.8 wt% /h and 1.3 wt% /h respectively. Hence, the thermal stability of the zeolite-13X not only affects the formation of CNTs, it also affects the catalytic activity required for methane decomposition.

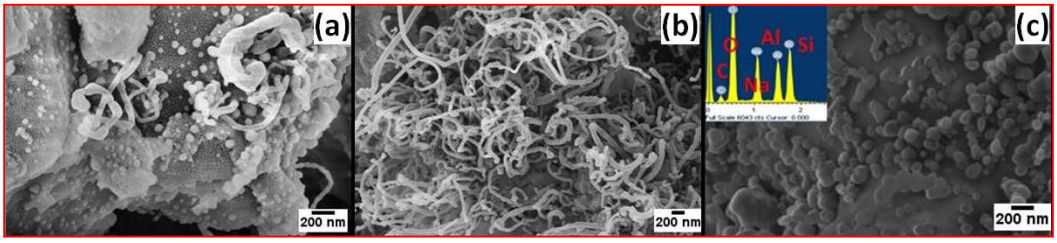

Figure 4.10: SEM micrographs of the as grown CNTs with (a) 5 wt% Fe impregnated zeolite-13X at 800 ^{o}C and (b & c) Fe impregnated zeolite-13X at pH-12

at 800 ^{o}C and 900 ^{o}C . Inset in fig-4.10c: EDS spectra showing the presence of carbon and chemical composition of zeolite-13X.

4.5 Effect of bi-metallic catalyst in CNTs synthesis

As discussed in earlier experiments, many parameters influence the growth of CNTs. To achieve higher yields and perfect structural CNT features, different combinations of a catalyst can be used. Fe–Mo, Co–Ni, and Co–Mo have been found to improve the control over the growth of CNTs because catalyst activity is significantly enhanced by the synergetic effect of the metals involved [39-40]. In addition, aggregation of catalyst particles can be prevented by the presence of more than one metal species. Also, the use of a co-catalyst instead of a single metal provides additional degrees of freedom, such metal species which have chemical and thermodynamic advantages [41]. The chemical advantages arise since the fractions of constituent species can be tailored to enhance the catalytic performance of the catalysts. Metallic nanoparticles are very efficient catalysts in their liquid or viscous state, probably because of considerable carbon bulk diffusion in these phases, as compared to surface or subsurface diffusion. The melting point of the catalyst is reduced by adding alloying components. Hence, the composition of catalyst nanoparticles could be tailored to enhance the yield and quality of CNTs by moving the liquid line of the alloy below the synthesis temperature.

4.5.1 Synthesis of few walled CNTs (FWCNTs): synergetic effect of Mo with Fe catalyst

Fig.-4.11 shows the temperature ramp and weight change with time corresponding to different stages of the CNT growth using a monometallic (Fe) and a bimetallic catalyst (Fe-Mo). In the stage S-1 weight loss is observed in two steps during a heating ramp up to 600^{o}C. This is mainly due to the release of adsorbed and

molecular water, while decomposition of corresponding precursor $Fe(NO_3)_2.9H_2O$, ammonium molybate and $Mg(OH)_2$ along with release of NO_2 and NH_3 occurs in second step. To produce active catalysts, iron oxide reduction is carried out in the presence of NH_3 during stages S-2 and S-3. In this step, Fe_xO_y is reduced to Fe in stages through intermediate phases viz., Fe_2O_3, Fe_3O_4, FeO and finally the active catalyst required for CNT synthesis is produced.

In stage S-4, CNT growth is initiated by methane decomposition, an endothermic process with ΔH=75.6 kJ/mol. As discussed earlier, the onset of thermal decomposition of methane takes place above 930^oC, whereas, catalytic decomposition occurs in the presence of Fe above 700^oC.

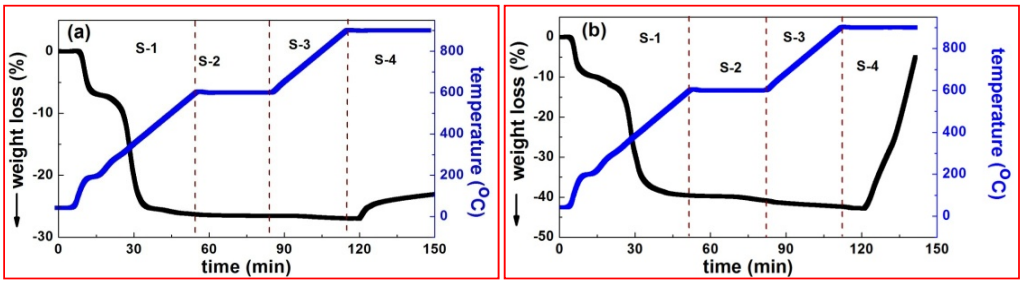

Figure 4.11: TG measurement during the CNT growth on (a) Fe-MgO (b) FeMo-MgO

In fig.-4.11a, the weight gain takes place at 900 ^oC just after the inflow of methane and Ar which results in catalytic decomposition of methane and deposition of carbon on the Fe/MgO support. During the first 5 min, the growth rate of CNTs is about 0.5 wt% /min and subsequently the growth rate declines to 0.06 wt%/ min. Over a span of 30 min the total weight gain is merely about 4 wt%. The reduction in growth rate is mainly attributed to Fe particles getting covered by the carbonaceous materials and thereby inhibiting the catalyst activity.

In the case of Fe-Mo/MgO, as shown in fig.-4.11b, the growth rate is very high when compared to Fe/MgO. The growth rate is about 1.4 wt% /min, which is about three times higher than the initial growth rate on Fe/MgO. In addition to a higher growth rate it is also sustained throughout the 30 min period. This improvement in growth is mainly attributed to the effect of Mo within a Fe matrix. The Fe and Mo form a mixture, in such a way that the active Fe catalyst is surrounded by passive Mo atoms. Here the formation of MoC from Mo acts as a buffer source for continuous supply of C to Fe which enhances the CNT growth. This phenomenon explains the sustained growth rate. Further, the addition of Mo reduces the effective diameter of catalyst by surrounding it and also reduces the agglomeration of Fe catalyst particles at higher temperatures. From TEM and SEM images as shown in fig.-4.1 2a&b, it is found that the diameter of the CNTs is significantly reduced from about 50 nm to below 10 nm.

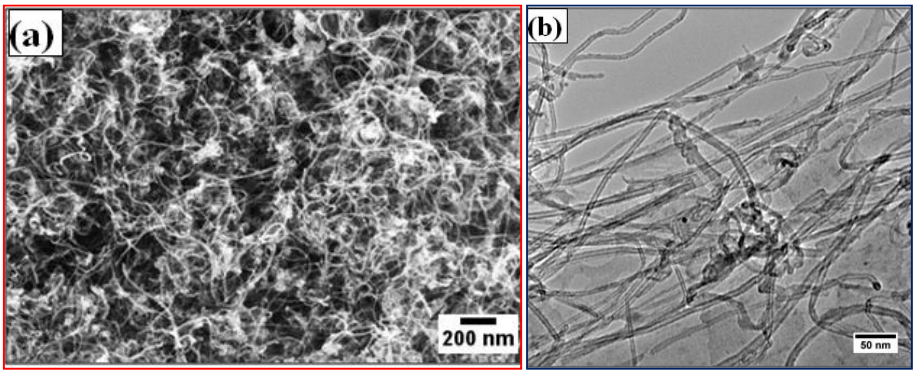

Figure 4.12: (a) SEM and (b) TEM morphology of the FWCNTs grown on Fe-Mo catalyst

4.5.2 Co–Ni and Co–Mo: Bamboo CNTs

The experiments were also repeated under similar conditions of growth as mentioned above for the growth of FWCNTs using different combination of bimetallic catalyst such as Co-Ni and Co-Mo. Fig.- 4.13 shows the SEM and TEM

images which indicate the diameter of the grown nanotubes are in the range 15-25 nm with intermediate diameter when compared to CNTs grown using Fe and Fe-Mo catalysts. TEM analysis shows that the tubes have a bamboo like structure consisting of equally spaced compartments. Bamboo like internal structure has often been observed for MWNTs. The understanding of the origin of the internal layers, which separate the tube body into several compartments, is still rudimentary. It has been suggested that the bamboo structures might be due to the catalyst type, size and shape. Slow displacement of the catalyst with the growing CNTs and bulk diffusion is projected as the primary source for the growth of the internal structures in characteristic bamboo like CNTs [42].

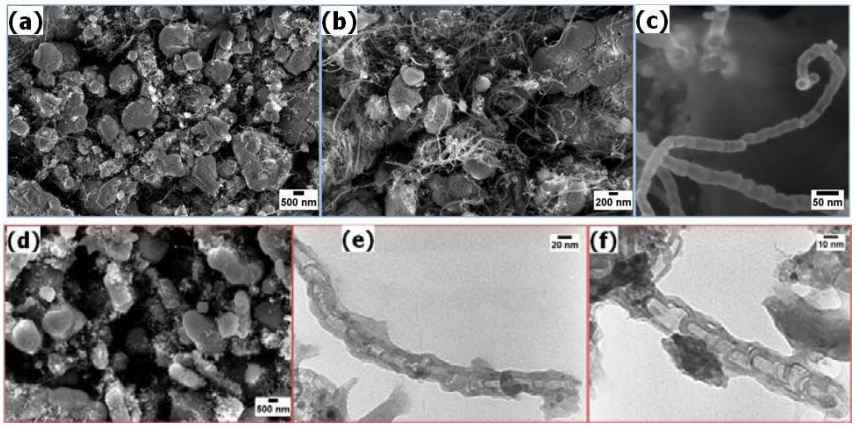

Figure 4.13 (a, b and c) SEM and TEM micrographs of bamboo like CNTs grown on Co-Mo /MgO and (d, e and f) on Co-Ni/ MgO.

4.6 Purification

High purity CNTs with few defects is a prerequisite for CNTs to be used as a structural and electronic material. The synthesis process using the CVD technique gives CNTs that contain impurities, most notably metal catalyst particles, the metal oxide catalyst support and unwanted carbonaceous by-products. These impurities can be removed by using their physical and chemical characteristic differences when compared with with CNTs [43]. Oxidation by acid treatment is one of the potential

approaches to convert metal and metal oxides into respective water soluble salts and then separate them from CNTs by simple filtration. Here, the chemical inertness of the graphitized CNTs is exploited. This simple cost effective method gives high yields with the possibility of a scaling up feature.

Though this method has unique advantages, finding a suitable combination of acids and optimization of process conditions are essential to get highly pure and minimally defective CNTs. A highly reactive concentrated acid treatment can oxidize amorphous carbon and fullerene caps in CNTs, and it can modify the structure of CNTs by functionalization. This will generate defects. To overcome these difficulties a less harsh purification process is necessary. In this thesis, mild acids were used to remove metal and metal oxide impurities. Further, we explore the effect of the oxidation agent H_2O_2 to remove carbonaceous impurities. In the following section, the step-wise procedure adopted for purification is discussed. Further, the efficiency of impurities removal was calculated by TGA. These aspects correspond to their structural quality and functionalization will be discussed in chapter-5

4.6.1 Purification of FWCNTs

The first purification step includes removal of the impurities by wet chemical oxidation. Hydrochloric and nitric acids are frequently used for this purpose. Additional steps include decanting, centrifugation or filtration followed by rinsing in de-ionized water. In between, gentle treatment in an ultrasonic bath helps to continuously loosen up the agglomerated nanotubes. These approaches are frequently combined to achieve a comprehensive purification and a higher CNT yield. Zeolite, alumina and silica are hard to dissolve chemically. Hence, HF was employed for removal of silica. This acid is difficult to handle due to its hazardous nature. In contrast, MgO can dissolve in mild acids. Several trials were made by using HCl,

HNO_3 and a mixture of HNO_3 with H_2SO_4 to generate purified CNTs and the results were evaluated using TGA as a primary tool to find the metal and metal oxide residue in the sample.

All TGA measurements for purity determinations were done in an atmosphere of 20% oxygen mixed with 80% Ar at a heating rate of 10^oC/min. Quantitative estimation of metal oxide impurities in the purified sample was calculated from the residual weight after removal of CNTs. At elevated temperatures in the presence of oxygen, structural carbon decomposes into CO and CO_2. The oxidation temperatures for amorphous carbon and CNTs are 300-450 ^oC and 500-650 ^oC, respectively. The integrity of the CNT structure depends on the quality of the tubes such as length, diameter, defect and functional groups which are reflected in the line shapes of the TGA curves. In the present study presence of amorphous carbon and structural damage of FWCNTs during acid treatments was calculated through TG weight loss curves. The analysis of the fraction of CNTs corresponding to different oxidation temperatures was evaluated by differential thermogravimetric (DTG) curves. Further, attempts to fit the DTG data with Gaussian line shapes were made. The center of the peak is taken as oxidation temperature for specific carbonaceous material. The percentage weight loss together with the oxidation temperature is a meaningful parameter to estimate the effect of acid treatment on the CNTs.

4.6.1.1 As grown FWCNTs

Fig.-4.14 shows a typical HRTEM image of the unpurified FWCNTs which contains MgO support, metallic catalyst (Fe-Mo/ MgO), amorphous carbon, and graphite nanoparticles. The dark regions in the TEM show the presence of Fe-Mo/MgO particles as well as FWCNTs. These as grown FWCNT samples were taken for purification process. To estimate the carbon content in the as grown FWCNTs, a

20 mg sample was taken for TG analysis and the results are shown in fig.-4.15a. Here, 0.4 wt% and 0.2 wt% weight losses are observed between 200-300 ^{o}C and 300-450 ^{o}C, respectively. This could be due to removal of molecular water and amorphous carbon respectively. In TG curve the major weight loss started around 550^{o}C and the estimated total weight loss was about 35 wt%. In conclusion as grown FWCNTs contain a small amount of carbonaceous impurities and their overall purity is about 35%. In forthcoming section the analysis on the effect of HCl on the purification of the as grown FWCNTs will be discussed.

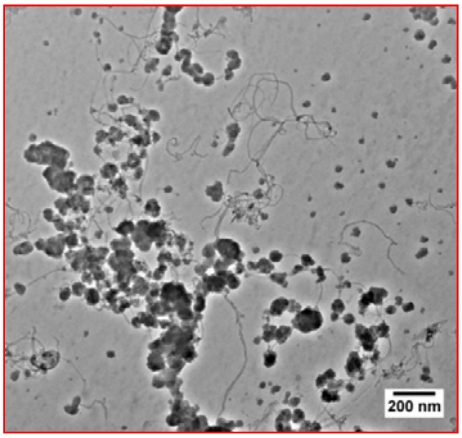

Figure 4.14: TEM micrograph of as grown FWCNTs shows the presence of catalyst support and FWCNTs in the sample.

4.6.1.2 Purification of FWCNTs with HCl

In all purification experiments, 15 mg of as grown CNTs were added to 20 ml of 5M HCl and different purification steps were used. Respective TGA and DTG plots are shown in fig.-4.15a&b.

In the first trial, the solution was stirred for 5 h. Then the solution was filtered and dried at 120^{o}C. TGA estimation shows an enhancement of carbon content than in as prepared pristine FWCNTs with a 68 wt% of total weight loss. To enhance the reactivity of HCl in purification process and to improve removal of impurities, a reflux process was adapted in the second trial. Here, the sample was refluxed with 5 mol. HCl at 80 ^{o}C for 2 h. This process further improved the purity to 81 wt%.

Though it enhances the purity, (11 wt% losses up to 450 ^{o}C) the data indicates an enhancement in functional group content and amorphous carbon materials arising from the damaged CNTs.

To reduce the reactivity and to increase the removal of metal oxide, a third trial was made using reflux at a lower temperature (70 ^{o}C) and for 5 h. During reflux process the solution was sonicated for 2 min for every one hour. Temperature reduction provides a marginal improvement in the CNT structure and the increased time provided enhanced purification of around 93 wt% of carbon material. Quantitative estimation of oxidation temperature is discussed below from DTG data.

Oxidation of acid functionalized CNTs may involve complex degradation mechanisms. TGA curve gives information on the distribution of tubes in the sample. The TG Derivative (dw/dt) curve is more useful to extract minor variations in the decomposition rates found in the TG curve. Since this curve represents a distribution of materials, in this thesis a attempt was made to fit data with Gaussian line shapes [44-45]. The DTG curve and deconvoluted peaks in the CNT decomposition region are shown in fig.-4.15b. R^2 values above 0.99 were used as fitting acceptance criteria. From the fitting parameters, the center of the peak is taken as oxidation temperature.

The samples corresponding to the as prepared and three trials are named as R, L1, L2 and L3 respectively. DTG curve for R, L1 and L2 were fitted by two Gaussian peaks whereas the broad L3 fitted with four peaks. The two peak centers and heights in the deconvoluted CNT decomposition region is represented as C1, C2 and h1, h2 respectively. Peak center and height ratios are shown in fig.-4.15c and 4.15d. Here, reduction of first oxidation temperature (C1) indicates degradation of the tube quality. Temperature difference between C1 and C2 correlated with peak broadening that corresponds to higher distribution of tube diameters in the sample. By taking

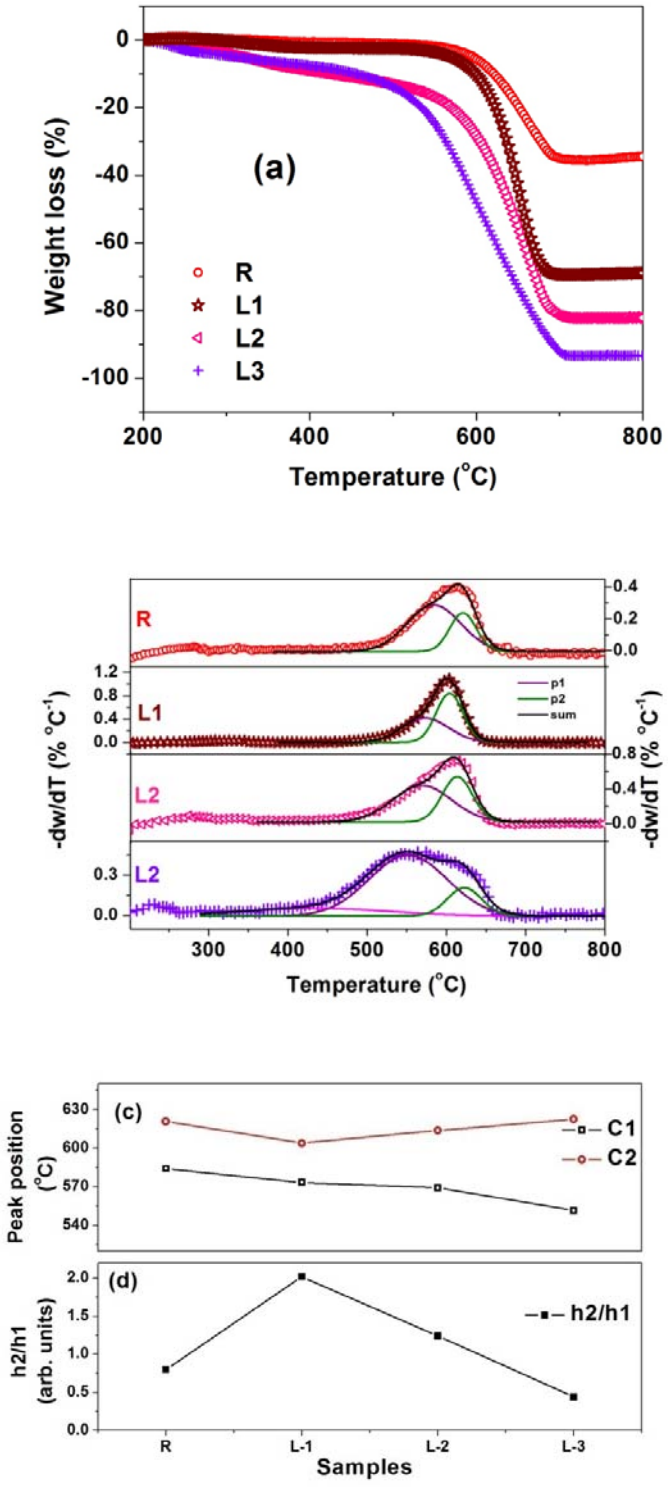

Figure 4.15: Purification of FWCNTs using HCl (a) TGA and (b) DTG. Comparison of (c) oxidation temperature and (d) peak height ratio for different samples.

into consideration of the fact that good quality tubes oxidize at high temperature, the peak height ratio between C2 and C1 was calculated and plotted in fig.-4.5c. The decrease in this parameter h2/h1 from L1-L3 indicates a reduction in the tube quality.

In conclusion from above studies, HCl treatment allows effective removal of impurities. A residual weight as low as 7 wt% can be achieved with the reflux process used. Meanwhile the treatment considerably changed the structure of the CNTs. To achieve high purity CNTs with fewer defects we used HNO_3.

4.6.1.3 Purification of FWCNTs with HNO_3 - multi step process

For the HNO_3 based purification, a reflux method was adopted. In this process, the as grown FWCNTs were taken in 5 mol. HNO_3 and sonicated for 5 min to get a uniform dispersion. This solution was refluxed at 70^{o}C for 5 h as like earlier.

The process was designated as N1 and the corresponding TGA of the sample is shown in fig.-4.16. An effective removal of impurities is observed with ~99% measured weight loss. Moreover, 2.5 wt% weight losses up to 450 ^{o}C shows that the surface modification of the CNT is less when compared to the 11 wt% losses in L2. Hence, after this process only trace levels of impurities are present and this could be catalyst trapped inside CNTs with fullerene caps.

To remove such trace impurities encapsulated inside the tubes, removal of fullerene cap is essential. HNO_3 treatment for a longer time can remove the fullerene cap but this can also affect the tube walls. Hence, a multi step process is essential for a complete purification. To remove the fullerene cap with less damage to the CNTs, H_2O_2 was used at room temperature in neutral condition. Here, the sample was stirred continuously for 7 days.

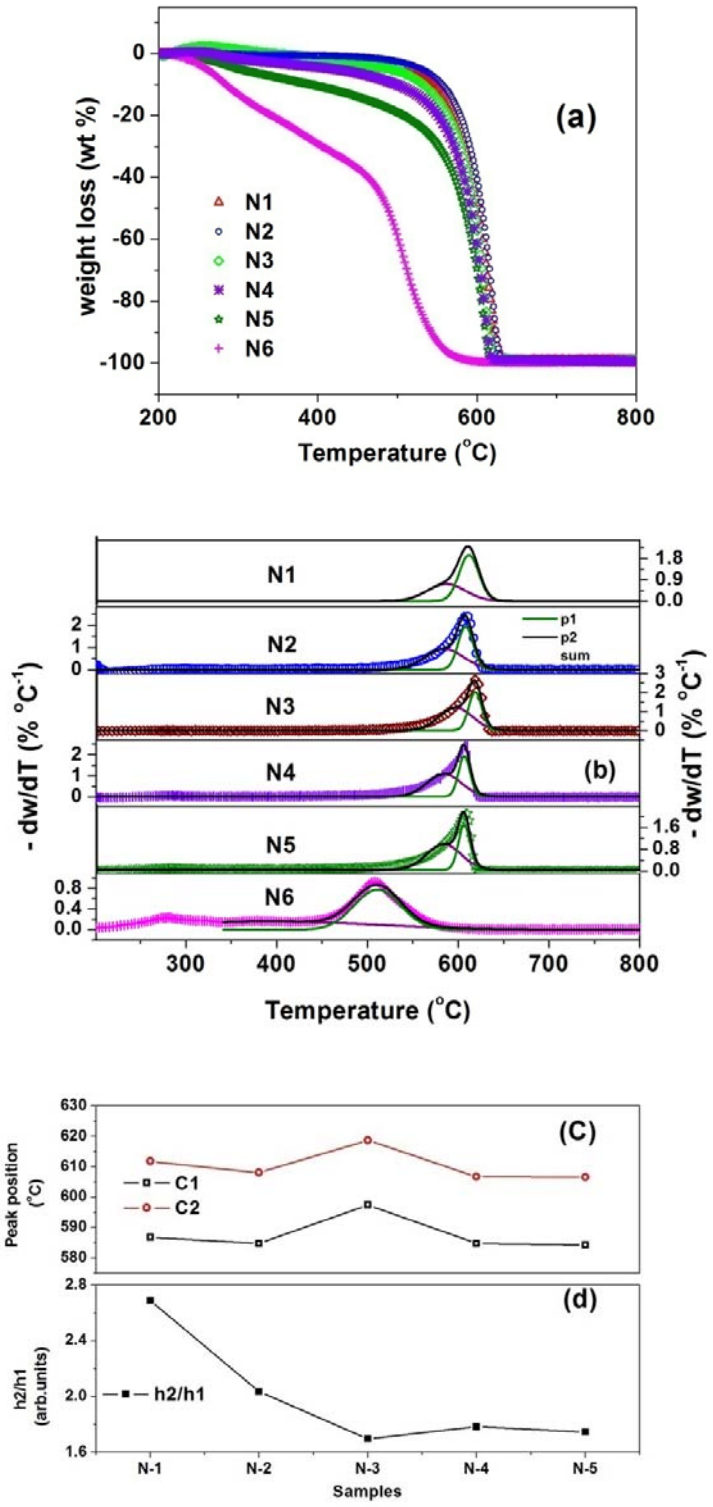

Figure 4.16: Step by step purification of FWCNTs (a) TGA and (b) DTG. (c) Oxidation temperature and (d) peak height ratio.

H_2O_2 treatment (N2) enhanced the thermal stability with only 1.1 wt% loss up to 450 ^oC. Residual weight present in the sample is below 1%. Hence, this treatment provides good purity without damaging the tubes. The purity evaluation in terms of intercalation and fullerene cap removal in CNTs are discussed in next chapter.

After decapping the tubes, to remove the trace metal particles which were encapsulated by a fullerene cap and to enhance functionalization a third step was carried out (N3). Here the sample was stirred in 5 mol. HNO_3 for 30 min. The structural quality of the tubes and functional groups (-OH and -COOH) present on these tubes will be discussed in the next chapter.

It is widely reported that a $1HNO_3$:$3H_2SO_4$ mixture is a good agent for oxidization and functionalization of CNTs [46]. To test for integrity of the sample for these high strength acids the following experiments were carried out and evaluated by TGA. Stirring (N4) for 20 min, refluxing for 20 min (N5) and 1 h (N6). In all these processes gradual degradation of the tubes observed with weight losses of about 3.4 wt%, 5.6 wt%, 13.8 wt% and 37 wt% for N3-N6, respectively for temperature up to 450^oC.

DTG curves and deconvoluted peaks for the purification processes N1-N6 are shown in fig.-4.16b. The observed trend for N6 indicates a distinct reduction in the oxidation temperature (510^oC) which shows a structural disintegration of CNTs. For a comparative study, oxidation temperatures and peak height ratio of N1-N5 were plotted in fig.-16c and 16d. It is observed that change in oxidation temperature did not give a remarkable change whereas h1/h2 decreased during each process step.

In conclusion, the multi step process with HNO_3 treatment followed by H_2O_2 treatment was required to produce high purity CNTs (up to 99.5%). The final step removes trace impurities but functionalizes the tube walls at the cost of CNTs quality.

4.6.1.4 X-ray diffraction analysis

The structure and chemical composition of the as grown and purified CNTs were determined by X-ray diffraction analysis (XRD) and the results are discussed below.

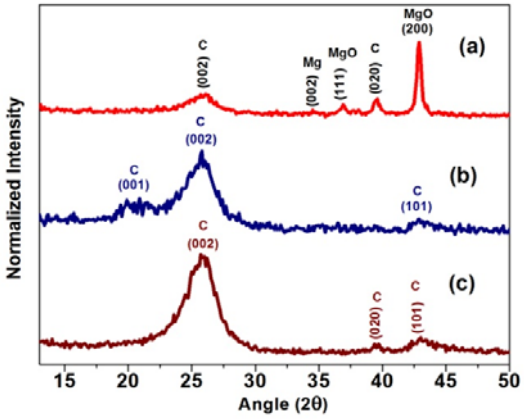

Figure 4.17: X-ray diffraction pattern of (a) as grown FWCNTs (R), samples that were treated with (b) H_2O_2 (N2) and (c) HNO_3 (N3) respectively in the multi step purification process.

Fig.-4.17 shows the XRD patterns of as synthesized and purified CNTs in the multi step process. In fig.-4.17a, as-grown CNTs show the presence of carbon along with the catalyst support materials, MgO and Mg. The intense peak (200) and small peak (111) correspond to the MgO support material, while the peak at 2θ ~ 34 (002) represents the Mg and other lower intensity peaks at 2θ are 26 (002) and 39 (021) are due to the graphitic structure. Fig.-4.17b&4.17c show the XRD pattern for CNTs after the second and third steps in the multistep purification process respectively. The absence of peaks corresponding to MgO and other impurities confirms the removal of all impurities from the as prepared CNTs. Also, other weak carbon peaks are seen in the purified samples. Thus, from the XRD analysis one can conclude that the non

carbonaceous elements were removed from the samples down to the XRD detection limit. The XRD results were consistent with TGA measurements.

4.7 Summary

Growth of CNTs on Fe impregnated MgO and zeolite-13X catalyst supports at 900^{o}C using methane as carbon source was investigated. The morphology and structure of CNTs grown on Fe-MgO and Fe-zeolite-13X have been analyzed by SEM and Raman spectroscopy. DTA and XRD analysis show that MgO is structurally stable while zeolite-13X is structurally unstable above 800^{o}C and undergoes crystalline phase transformations. TGA–MS results clearly show that the catalytic decomposition of the methane takes place on Fe-MgO in the temperature regime above 750^{o}C but the peaks are absent in Fe-zeolite-13X. The key findings from these investigations show that the lack of reduction of the impregnated iron oxide during ammonia treatment on the zeolite-13X surface results in the paucity of the active catalyst that in turn impedes the growth of CNTs on zeolite-13X. By tuning the basic nature of the support one can enhance the growth of CNTs within the thermal stability window of the support.

The role of the Fe catalyst in CNT synthesis has been analyzed through in situ TGA-MS analysis. The growths were monitored using TGA-MS through a programmable temperature ramp. It was found that sustained catalyst activity was achieved throughout the growth period by the addition of Mo. Also, the enhancement in yield and reduction in tube diameter is possible using Mo is added to Fe. Thus the addition of Mo to active Fe catalyst gives a handle to tune the diameter and yield of CNTs. Other bimetallic catalysts such as Co-Mo and Co-Ni provide CNTs with a bamboo type structure, having internal compartments, with yields that were also lower

compared to the Fe-Mo catalyst. The FWCNTs grown using the Fe-Mo catalyst was taken for purification and FWCNTs with purity better than 99.5% were achieved through a multi step purification process.

4.8 References

[1] C. L. Kane and E. J. Mele, "Size, Shape, and Low Energy Electronic Structure of Carbon Nanotubes," *Physical Review Letters,* vol. 78, p. 1932, 1997.

[2] J. W. G. Wildoer*, et al.*, "Electronic structure of atomically resolved carbon nanotubes," *Nature,* vol. 391, p. 59, 1998.

[3] M. Abe*, et al.*, "Structural transformation from single-wall to double-wall carbon nanotube bundles," *Physical Review B,* vol. 68, p. 041405, 2003.

[4] Y. Saito, "Nanoparticles and filled nanocapsules," *Carbon,* vol. 33, p. 979, 1995.

[5] E. F. Kukovitsky*, et al.*, "VLS-growth of carbon nanotubes from the vapor," *Chemical Physics Letters,* vol. 317, p. 65, 2000.

[6] A. S. Magrez, R*, et al.*, "Striking influence of the catalyst support and its acid-base properties: new insight into the growth mechanism of carbon nanotubes," vol. 5, p. 3428, 2012.

[7] Y. Chen and J. Zhang, "Diameter controlled growth of single-walled carbon nanotubes from SiO_2 nanoparticles," *Carbon,* vol. 49, p. 3316, 2011.

[8] A.-C. Dupuis, "The catalyst in the CCVD of carbon nanotubes - a review," *Progress in Materials Science,* vol. 50, p. 929, 2005.

[9] Ç. Öncel and Y. Yürüm, "Carbon nanotube synthesis via the catalytic CVD method: A review on the effect of reaction parameters," *Fullerenes, Nanotubes, and Carbon Nonstructures,* vol. 14, p. 17, 2006.

[10] M. Meyyappan, *et al.*, "Carbon nanotube growth by PECVD: a review," *Plasma Sources Science and Technology,* vol. 12, p. 205, 2003.

[11] M. Kumar and Y. Ando, "Chemical vapor deposition of carbon nanotubes: a review on growth mechanism and mass production," *Journal of nanoscience and nanotechnology,* vol. 10, p. 3739, 2010.

[12] R. L. Vander Wal, *et al.*, "Substrate–support interactions in metal-catalyzed carbon nanofiber growth," *Carbon,* vol. 39, p. 2277, 2001.

[13] A. M. Cassell, *et al.*, "Large scale CVD synthesis of single-walled carbon nanotubes," *The Journal of Physical Chemistry B,* vol. 103, p. 6484, 1999.

[14] P. B. Amama, *et al.*, "Influence of alumina type on the evolution and activity of alumina-supported Fe catalysts in single-walled carbon nanotube carpet growth," *ACS nano,* vol. 4, p. 895, 2010.

[15] D. Mravec, *et al.*, "Some possibilities of catalytic and noncatalytic utilization of zeolites," *Chem. Pap,* vol. 59, p. 62, 2005.

[16] B. Smit and T. L. M. Maesen, "Towards a molecular understanding of shape selectivity," *Nature,* vol. 451, p. 671, 2008.

[17] Z. K. Tang, *et al.*, "Superconductivity in 4 Angstrom Single-Walled Carbon Nanotubes," *Science,* vol. 292, p. 2462, 2001.

[18] A. Okamoto and H. Shinohara, "Control of diameter distribution of single-walled carbon nanotubes using the zeolite-CCVD method at atmospheric pressure," *Carbon,* vol. 43, p. 431, 2005.

[19] R. M. Morris and K. J. Klabunde, "Formation of paramagnetic adsorbed molecules on thermally activated magnesium and calcium oxides. Characteristics of the active surface sites," *Inorganic Chemistry,* vol. 22, p. 682, 1983.

[20] B. C. Liu*, et al.*, "Single-walled carbon nanotubes produced by catalytic chemical vapor deposition of acetylene over Fe–Mo/MgO catalyst," *Chemical Physics Letters,* vol. 383, p. 104, 2004.

[21] H. Ago*, et al.*, "Gas analysis of the CVD process for high yield growth of carbon nanotubes over metal-supported catalysts," *Carbon,* vol. 44, p. 2912, 2006.

[22] C. Bower*, et al.*, "Nucleation and growth of carbon nanotubes by microwave plasma chemical vapor deposition," *Applied Physics Letters,* vol. 77, p. 2767, 2000.

[23] M. Chhowalla*, et al.*, "Growth process conditions of vertically aligned carbon nanotubes using plasma enhanced chemical vapor deposition," *Journal of Applied Physics,* vol. 90, p. 5308, 2001.

[24] W. H. Chiang and R. M. Sankaran, "Relating carbon nanotube growth parameters to the size and composition of nanocatalysts," *Diamond and Related Materials,* vol. 18, p. 946, 2009.

[25] J. A. Schwarz*, et al.*, "Methods for preparation of catalytic materials," *Chemical reviews,* vol. 95, p. 477, 1995.

[26] M. S. Dresselhaus*, et al.*, "Raman spectroscopy of carbon nanotubes," *Physics Reports,* vol. 409, p. 47, 2005.

[27] S. Reich and C. Thomsen, "Raman spectroscopy of graphite," *Philosophical Transactions of the Royal Society of London. Series A: Mathematical, Physical and Engineering Sciences,* vol. 362, p. 2271, 2004.

[28] A. C. Ferrari and J. Robertson, "Raman spectroscopy of amorphous, nanostructured, diamond–like carbon, and nanodiamond," *Philosophical*

Transactions of the Royal Society of London. Series A: Mathematical, Physical and Engineering Sciences, vol. 362, p. 2477, 2004.

[29] F. Fajula*, et al.*, "Synthesis of zeolite omega. Influence of the temperature and the reagents on the crystallization kinetics," *Zeolites,* vol. 7, p. 203, 1987.

[30] S. Ernst*, et al.*, "Zeolite ZSM-20: synthesis and characterization through XRD, SEM and thermal analysis," *Zeolites,* vol. 7, p. 180, 1987.

[31] J. Li*, et al.*, "Studies on natural STI zeolite: modification, structure, adsorption and catalysis," *Microporous and Mesoporous Materials,* vol. 37, p. 365, 2000.

[32] H. Mimura and T. Kanno, *Processing of Radioactive Waste Solution with Zeolites (I): Thermal-Transformations of Na, Cs and Sr Forms of Zeolites* vol. 29: Sci. Rept. Res. Inst. Tohoku University, 1980.

[33] K. Hernadi*, et al.*, "Production of nanotubes by the catalytic decomposition of different carbon-containing compounds," *Applied Catalysis A: General,* vol. 199, p. 245, 2000.

[34] A. Fonseca*, et al.*, "Optimization of catalytic production and purification of buckytubes," *Journal of Molecular Catalysis A: Chemical,* vol. 107, p. 159, 1996.

[35] K. Hernadi, "Catalytic synthesis of multiwall carbon nanotubes from methylacetylene," *Chemical Physics Letters,* vol. 363, p. 169, 2002.

[36] M. Kumar and Y. Ando, "Controlling the diameter distribution of carbon nanotubes grown from camphor on a zeolite support," *Carbon,* vol. 43, p. 533, 2005.

[37] F. Akhtar and L. Bergström, "Colloidal Processing and Thermal Treatment of Binderless Hierarchically Porous Zeolite 13X Monoliths for CO2 Capture," *Journal of the American Ceramic Society,* vol. 94, p. 92, 2011.

[38] W. Shan, *et al.*, "Electrophoretic deposition of nanosized zeolites in non-aqueous medium and its application in fabricating thin zeolite membranes," *Microporous and Mesoporous Materials,* vol. 69, p. 35, 2004.

[39] W. Q. Deng, *et al.*, "A two-stage mechanism of bimetallic catalyzed growth of single-walled carbon nanotubes," *Nano letters,* vol. 4, p. 2331, 2004.

[40] W. H. Chiang and R. M. Sankaran, "Synergistic effects in bimetallic nanoparticles for low temperature carbon nanotube growth," *Advanced Materials,* vol. 20, p. 4857, 2008.

[41] H. Liu, *et al.*, "Effects of bimetallic catalysts on synthesis of nitrogen-doped carbon nanotubes as nanoscale energetic materials," *Particuology,* vol. 9, p. 465, 2011.

[42] C. J. Lee and J. Park, "Growth model of bamboo-shaped carbon nanotubes by thermal chemical vapor deposition," *Applied Physics Letters,* vol. 77, p. 3397, 2000.

[43] P.-X. Hou, *et al.*, "Purification of carbon nanotubes," *Carbon,* vol. 46, p. 2003, 2008.

[44] K. Dasgupta, *et al.*, "The production of high purity carbon nanotubes with high yield using cobalt formate catalyst on carbon black," *Materials Letters,* vol. 61, p. 4496, 2007.

[45] M. R. Smith Jr, *et al.*, "Selective oxidation of single-walled carbon nanotubes using carbon dioxide," *Carbon,* vol. 41, p. 1221, 2003.

[46] J. Zhang, *et al.*, "Effect of chemical oxidation on the structure of single-walled carbon nanotubes," *The Journal of Physical Chemistry B,* vol. 107, p. 3712, 2003.

Chapter-5 Raman spectroscopy and transport studies on FWCNTs

5.1 Introduction

The exceptional structural and transport properties of CNTs allow them to be incorporated in micro and nano-electronic devices to achieve superior performance. However, owing to the enormous difficulties in handling a single nanotube, an ensemble of CNTs can be used as a random network. In a CNT based devices, these networks will improve the current carrying capacity, stability, reproducibility and reduce failure rate of devices. Though fabrication of such network is easily achievable by direct growth of CNTs or solution deposition methods, the collection behavior of the CNTs in the network has to be studied in detail. [1]. Hence it is essential to characterize and understand the collective behavior of CNTs in a network.

The pronounced influence of structural parameters like diameter, helicity and the number of concentric cylinders modifies the band structure of individual CNTs and results in unusual electrical transport properties. Theoretical and experimental studies show that electron transport in a defect free CNT exhibits ballistic conduction. Nevertheless, the presence of defects and impurities modifies the phonon and electronic structure to produce diffusive conduction phenomena [2-5]. These structural properties and their modifications affect the optical properties of CNTs. The optical properties studied by Raman spectroscopy provide information on phonon and electronic structures. Understanding the Raman active modes allows for the analysis of allotropic forms of carbon, structural defects and impurities. Hence, correlations between Raman spectroscopy and transport properties provide experimental evidence about CNT device characteristics.

This chapter comprises of two sections. In the first part, Raman spectroscopy is used to study the structural properties of the grown FWCNTs. It is known that CVD growth and purification processes significantly incorporate defects and functional groups in FWCNTs [6-7]. These physical and chemical modifications in tube walls are evaluated by Raman active modes and correlated with HRTEM and FTIR studies.

In the second part, FWCNTs are spin coated to form a random network and their temperature dependent conduction mechanisms are studied. Transport models including power law, Luttinger liquid model, metallic conductivity, variable range hopping (VRH) [8] and fluctuation induced tunneling (FIT) [9-10] are used to explain the conduction mechanism. In spite of many suggested theories to explain the transport mechanism in a CNT random network, a comprehensive and consistent picture pertaining to tube diameter and structure of CNTs is still elusive. In this chapter the effect of tube diameter and structural defects on the transport mechanism are studied using FWCNTs network.

5.2 Raman spectroscopy of CNTs

The first Brillion zone and phonon dispersion relation for graphite is shown in fig.-5.1a&b, respectively. Here, Γ, K and M are the high symmetric points present at the zone center, corner and middle of the two corners [11-12]. According to quantum mechanical selection rules, Raman scattering can probe phonon modes close to the zone center. Further, introduction of defects in a crystal lattice activates phonons from inside the first Brillion zone. In the Raman spectrum, these phenomena are used to evaluate the structure and quality of the CNTs associated with graphitic and defect related peaks.

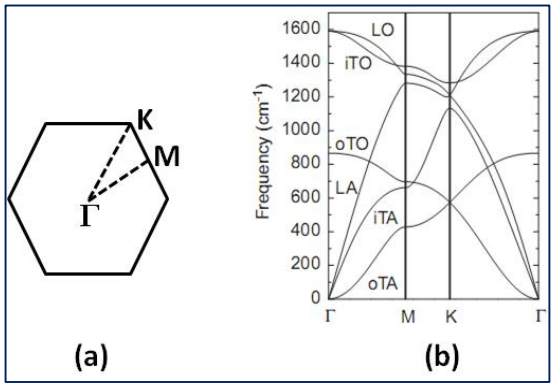

Figure 5.1: (a) First Brillion zone and high symmetric points of 2D graphite and (b) Phonon dispersion. The phonon branches are labeled: out-of-plane transverse acoustic (oTA); in-plane transverse acoustic (iTA); longitudinal acoustic (LA); out-of-plane transverse optic (oTO); in-plane transverse optic (iTO); longitudinal optic (LO) [11-12].

5.2.1 Geometry dependent Raman spectra of CNTs

Geometrically CNTs are envisioned as rolled graphene sheets with different diameter and helicity [13]. Here, confinement of electrons around the circumference of CNTs makes them behave as a 1-D quantum wire. This geometrical phenomenon affects the allowed phonon modes and electronic properties. Hence, CNTs are significantly different from planar graphite.

In this section, the Raman modes in FWCNTs, MWCNTs are compared with highly oriented pyrolytic carbon (HOPG). The fig.-5.2 shows the Raman spectra obtained using 2.14 eV laser excitation of HOPG, as grown MWCNTs and FWCNTs grown on Fe/MgO and Fe-Mo/MgO, respectively. As grown samples were chosen to avoid ambiguities pertaining to purification induced shifts from chemical doping.

In a Raman spectrum, the G-band is a first order process from an iTO phonon in the zone center (Γ). A Lorenzian fit to the experimental data shows G peak positions at 1581, 1580 and 1572 cm^{-1} for HOPG, MWCNTs and FWCNTs, respectively. Here, the G-peak position of FWCNTs, MWCNTs are down shifted

around 9 and 1 cm^{-1}, respectively with reference to HOPG. This shift in the G-band peak is attributed to phonon softening from a stretched C–C bond due to curvature created by rolling of a graphene sheet [14-15]. This observation is supported by the estimated diameter of FWCNTs and MWCNTs 5-10 nm and 50-80 nm, respectively. This analysis shows that phonon modes of higher diameter MWCNTs behave like an unstretched 2D planar graphite. Further, at resonant condition a weak RBM is found in FWCNTs which reveals the existence of a diameter dependent property as in SWCNTs. This RBM related behavior is discussed appropriately in a later part of this chapter.

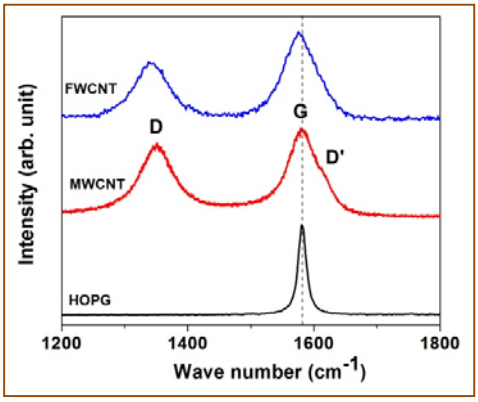

Figure 5.2: Raman spectra of HOPG, MWCNTs and FWCNTs. The vertical dotted line shows the center of G band in HOPG

D and D′ bands arise from LO or iTO phonons in K point. The presence of defects in a graphite lattice is a necessary condition to activate these modes. Hence, these bands are absent in highly crystalline HOPG. However, the inherent nature of CVD growth yields defect bands around 1350 (D), 1610 cm^{-1} (D′) in FWCNTs and MWCNTs.

Based on the above analysis, it can be shown that the Raman spectra of FWCNTs are significantly different from MWCNTs. In the following section, the

effect of purification of FWCNTs was evaluated from Raman spectroscopy along with the appropriate supportive techniques such as FTIR and HRTEM.

5.2.2 Effect of chemical purification on FWCNTs

To study the effect of the chemical purification process, Raman spectra of the multi step purified FWCNTs was analyzed. The observed spectrum is divided into three regimes I, II and III corresponds to 1000-2000, 2500-3200 cm^{-1} and < 400cm^{-1}, respectively. Inferences derived from these analyses are correlated with structural properties of FWCNTs.

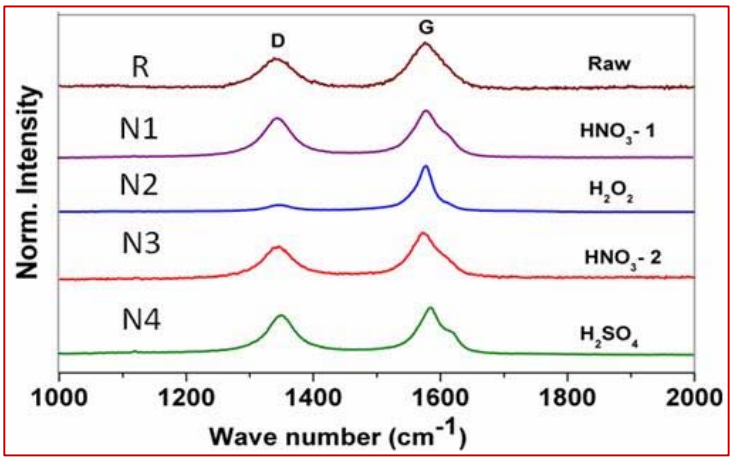

Figure 5.3: First order Raman spectra of FWCNTs in the regime-I using laser excitation energy of 514 nm for each purification step.

5.2.2.1 Evolution of acid treated FWCNTs: G, D and D' bands

In this study, FWCNTs referred as R, N1, N2, N3 and N4 were studied; they were synthesized as discussed in chapter-4. In regime-I (fig.-5.3) strong features of D, G and a weak D′ bands are identified using a Lorenzian fit with R^2 values better than 0.98. The obtained fit parameters are given in the table 1. By comparing these parameters, it is found that H_2O_2 treatment (N2) provides a sharp G band with a weaker D band. In contrast, $1HNO_3{:}3H_2SO_4$ treated FWCNTs (N4) show strong D and D' bands. The origin and quantification of these defects are discussed below.

The absolute intensity of the G, D, and D' bands and their ratio I_D/I_G and $I_{D'}/I_G$ were used to measure of the quality of the FWCNTs. Fig.-5.4 shows the plot for the calculated I_D/I_G and $I_{D'}/I_G$ for each progressive purification step. Here, I_D/I_G ratio for the N1 treated samples, is found to increase from 0.753 to 0.848 whereas the $I_{D'}/I_G$ reduces from 0.38 to 0.19. Although, both D and D' phonon modes are related to defects, the contrasting behavior indicates that they have different manifestation. It is reported that, while both intrinsic defects in the crystalline and amorphous carbon contributing to the D band, the D' band represents only the intrinsic defects and intercalation [16]. Here, an intrinsic defect in the FWCNTs could be in plane substitution of hetero-atoms, vacancies, grain boundaries and a finite size effect. All of these defects contribute to reduce crystal symmetry of the quasi infinite lattice structure of the FWCNTs.

Based on these observations, it is concluded that the amorphous carbon increases by a small amount during the purification step while intrinsic defects and impurities are reduced. It may arise from decomposition of poorly graphitized carbon during removal of impurities such as, Fe and MgO in the purification process. Subsequent treatments from N1 to N4 follow similar trends in I_D/I_G and $I_{D'}/I_G$ ratios. To investigate the origin of these defects pertaining to chemical functionalization, FTIR measurements were carried out and are discussed in the following section.

Sample	Raman mode (cm^{-1})				I_D/I_G	I_D/I_G
	D	G	D'	G' (2D)		
R	1342.1	1571.7	1599.1	2685.6	0.75	0.38
N1	1345.6	1579.4	1613.8	2688.1	0.85	0.19
N2	1347.7	1575.3	1614.3	2674.3	0.14	0.02
N3	1350.2	1579.1	1609.1	2687.1	0.71	0.17
N4	1350.5	1584.8	1619.9	2695.7	0.85	0.22

Table 5.1: Comparison of Lorenzian fit parameters in Raman spectra of FWCNTs for purification steps R to N4.

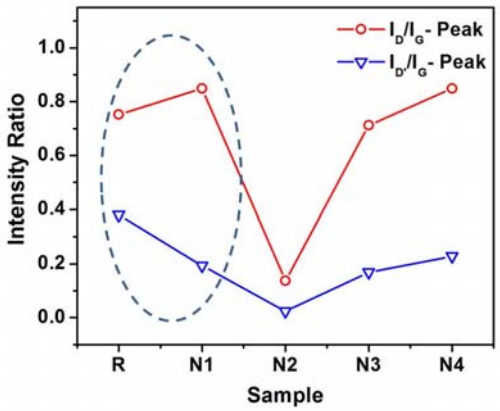

Figure 5.4: Raman peak intensity ratios (I_D/I_G and $I_{D'}/I_G$) for purified samples using a 514 nm laser excitation. The dotted circle shows an opposite trend in I_D/I_G and $I_{D'}/I_G$ ratio between the R and N1 treatment.

5.2.2.2 Characterization of FWCNTs by FTIR

FTIR is a powerful tool to probe the functional groups that are attached to the CNT walls. FTIR spectra obtained for the R to N4 purification processes are shown in fig.-5.5. The peak at 1450 cm^{-1} in the as prepared sample shows the presence of MgO. This is attributed to O-Mg-O molecular stretching in MgO [17]. Peaks at 1580 and 1630 cm^{-1} are assigned to the C=C stretching from the carbon network backbone in the CNTs and -OH stretching from -COOH groups, respectively. All the samples show a peak around 3560 cm^{-1} that corresponds to –OH functional group from free water molecules. Schematics of this functionalization by oxidizing agents are shown in fig.-5.6.

Purification steps show a progressive increase in of –COOH functionalization and reduction of C=C stretching. Hence, it is evident that purification steps progressively modify the surface of the FWCNTs with carboxylic acid groups. Moreover, no significant change in the functional groups associated with H_2O_2 treatment is observed to support defect reduction derived from Raman spectra. Hence,

from FTIR studies it is concluded that a drastic reduction of defect concentration is not induced by functionalization of FWCNTs.

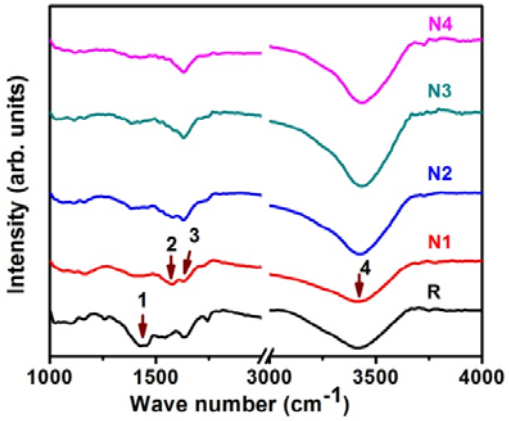

Figure 5.5: FTIR spectra show the presence of functional groups on the CNT walls. Here, 1, 2, 3 and 4 represents O-Mg-O, C=C, -COOH and OH groups respectively.

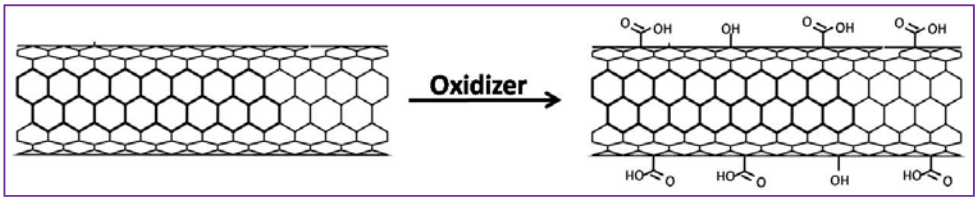

Figure 5.6: Schematic diagram showing the oxidation of CNTs to give functional groups such as -OH and -COOH.

Apart from functionalization related defects, amorphous carbon, structural change and intercalation also manifest as defects. By considering the structure of FWCNTs, the presence of a fullerene cap can also exhibit a defect structure in the Raman spectra. This aspect is investigated by using HRTEM in the following section.

5.2.2.3 Cap removal

Hemispherical fullerene cap in a FWCNT consists of a combination of pentagon and heptagon rings to give a spherical shape. These non graphitic structures act as a defect in the sp^2 lattice and contribute to enhancement of D band intensity.

Compared to a stable hexagonal sp^2 structure, the non sp^2 areas are found to be highly unstable for chemical process [18]. For direct observation of these spots, HRTEM analysis has been carried out for N1 and N2 treated samples (Fig.-5.7). A close observation depicted in the inset reveals the presence of a fullerene cap before H_2O_2 treatment and cap removal after the treatment.

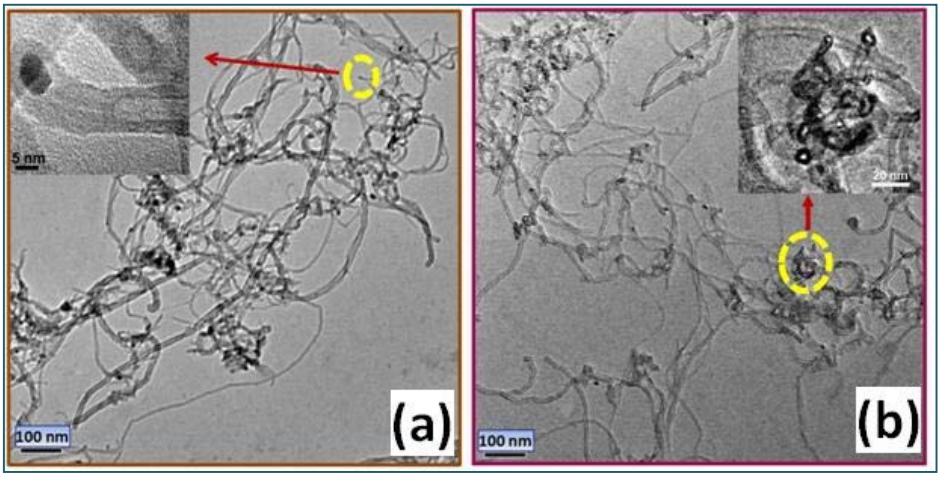

Figure 5.7: HRTEM images of the (a) HNO_3-1(N1) purified FWCNTs (b) H_2O_2 (N2) treated FWCNTs. The insets give a closer view of the tube ends before and after the removal of a fullerene cap.

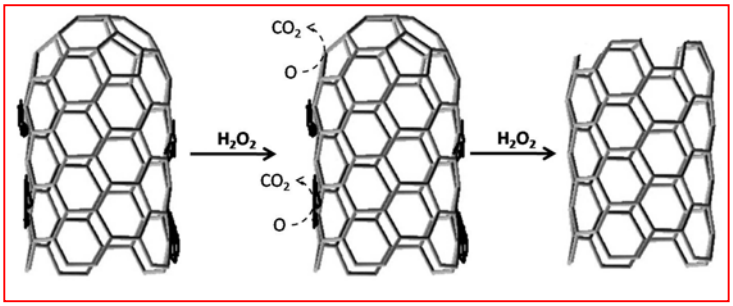

Figure 5.8: Schematic diagram for the oxidation of amorphous carbon and cap removal by H_2O_2.

Cap removal can be achieved using the strong oxidizing property of H_2O_2. Even at room temperature it can oxidize the chemically unstable non sp^2 carbon atoms, amorphous carbon and other defective areas in the FWCNTs [19-20]. Hence,

prolonged stirring in H_2O_2 facilitates the removal of amorphous carbon and fullerene caps. This process could explain the high graphitic nature estimated by the smaller FWHM of the G-band after H_2O_2 treatment. The schematic of this reaction is shown in fig.-5.8.

Calculated values of I_D/I_G for N1 and N2 are found to be 0.85 and 0.13, respectively. Though the defects are reduced after H_2O_2 treatment (N2), it increases again after N3 (0.71) and N4 (0.85) treatments which are close to N1. This increase in D band intensity is validated by production of amorphous carbon during acid treatment. To explain the D´ band intensity, the present analysis is further extended to relate the acid molecule induced defects due to intercalation.

5.2.2.4 Intercalation

The production of a graphite intercalated compound (GIC) by HNO_3 or a mixture of HNO_3 and H_2SO_4 treatment is widely studied. GICs are formed by the insertion of guest chemical species between layers in the graphite.

Carbon atoms in the graphite structure contain two distinct types of bonding orbitals. One of them is the strong covalent "σ bond" based on $sp^x p^y$ orbital and other is the weak "π bond" based on the interaction of p^z orbital. It is unlikely that the graphite lattice sites were substitutionally doped by electron donors or acceptors because the in-plane C-C bond is very strong. Hence, the dopants tend to occupy the interstitial spaces between adjacent graphene sheets thus forming "graphite intercalation compounds". The same idea also applies to carbon nanotubes, where it is rather difficult to dope nanotube walls substitutionally but the dopant atoms can occupy the space between two layers [21].

In HNO_3 treated FWCNTs, the intercalant is present in the form of neutral HNO_3 molecules admixed with charged NO_3^- ions. In this process, the NO_2^+ ion

oxidizes the FWCNTs and introduces hole doping as shown in equation 5.2. Hence, intercalated FWCNTs behave as p type semiconductors. The reaction is depicted as,

$$HNO_3 \leftrightarrow NO_2^+ + NO_3^- + H2O \quad (5.1)$$

$$NO_2^+ + C \rightarrow C^+ + NO_2 \uparrow \quad (5.2)$$

In a mixed solution of HNO_3 and H_2SO_4, the generation of NO_2^+ ion is catalyzed by H_2SO_4. Hence, the NO_2^+ ion density increases with respect to H_2SO_4 in the solution. The reaction is as follows,

$$HNO_3 + 2H_2SO_4 \rightarrow NO_2^+ + H_3O^+ + 2HSO_4^- \quad (5.3)$$

Hence, charge transfer from intercalation species could shift the Fermi energy E_F in the nanotube electronic band structure. Since the layers of CNTs with different chemical environments have different Raman characteristics, it can be used to investigate the intercalation species and their concentration [21-22].

After the purification process N1 to N4, the G band peak positions are observed at 1579, 1575, 1579 and 1584 cm^{-1}, respectively. By comparing the peak position of the raw sample (1571 cm^{-1}), the N1 treatment upshifts the G peak by 8 cm^{-1}. This is partially recovered by N2 (4 cm^{-1}) treatment which indicates a de-doping behavior in the FWCNTs. Subsequent, N3 and N4 process further upshifts G-peak by 4 and 9 cm^{-1}, respectively with respect to N2. These observations reveal that the electronic properties of FWCNTs are modified by each acid treatment. The upshift of the G band occurs due to the hardening of phonon modes i.e. by hole doping. Hence, HNO_3 treatment enhances hole doping by introducing NO_2^+ ion intercalation whereas H_2O_2 treatment reduces the intercalated NO_2^+ ions and thus act as a de-doping agent. As discussed earlier (5.2.2.4), enhancement of the nitronium ion concentration in the solution gives a higher shift in the G peak for the mixture of

HNO_3 and H_2SO_4 than observed to the HNO_3 treatment. This electronic perturbation related phonon frequency shift in the G' band will be discussed below.

5.2.2.5 Second order defect band: G' (2D), D+G

The second harmonic of the D band is called the G′ band and a combination of D+G bands and the most intensive features are found in regime-II (2000 to 3000 cm^{-1}) (fig.-5.9). The peak position of the G′ band for the N1 to N4 processes are at 2688, 2674, 2687 and 2696 cm^{-1} respectively as found from a Lorenzian fit. Similar to the G band, an upshift in the G′ band with respect to N2 is observed for N1 (14 cm^{-1}), N3 (13 cm^{-1}) and N4 (22 cm^{-1}) treatments, respectively. Here, the shift in G′ band is significantly higher than the G band shift. This G′ band is more sensitive to small perturbations in the electronic structure or the environment around the nanotubes. Hence, this band is effectively used to determine the number of layers in graphene materials. Moreover, fitting a G′ band with a single peak is much more straight forward than deconvoluting the G band with a D' band. The next intensive feature in the Raman spectra is a sum of D+G bands which also follows a similar trend for the N1 to N4 processes (2927.5, 2925, 2828 and 2939 cm^{-1}) as found for the upshift in the G and G′ bands [23].

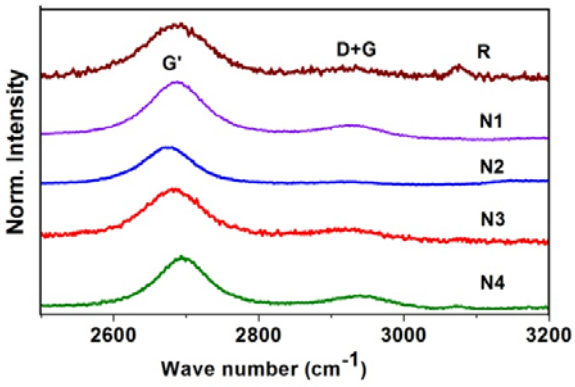

Figure 5.9: Second order Raman spectra of the FWCNTs after each purification step.

By combining these results with the FTIR spectra, it is concluded that acid treatment yields amorphous carbon, functionalization and intercalation whereas H_2O_2 treatment gives oxidized amorphous carbon, functionalized CNT walls and reduced intercalated acid molecules in the FWCNTs.

5.2.2.6 Radial Breathing Mode (RBM)

Radial breathing mode (RBM) is an unique quantum behavior and is observed only in SWCNTs due to the vibration of carbon atom along the tube diameter [13]. The signature of a RBM is reduced by increasing the diameter and number of walls in CNTs. However, a RBM signature in FWCNTs cannot be ruled out completely, especially when the inner diameter of the tubes are comparable to SWCNTs when the resonance condition can be satisfied. Furthermore, a strong correlation of the RBM with tube diameter can be used to extract an accurate diameter distribution in the sample. An expression relating the observed RBM frequency and the tube diameter can be written as,

$$\omega_{RBM} = \frac{C_1}{d(nm)} + C_2\ (cm^{-1}) \tag{5.4}$$

where, C_1 and C_2 are constants and found to be 235 (cm^{-1} nm) and 9 (cm^{-1}), respectively. Here C_2 is attributed to the bundling effect.

Using the above equation it is possible to calculate the diameter of FWCNTs, since it presumably resembles SWCNTs bundles [24]. The RBM in regime-III (100 to 400 cm^{-1}) for samples R, N1 to N4 treatments are shown in fig.-5.10. Here, only the H_2O_2 (N2) treated sample shows a RBM mode and this could come from inner diameter of the tube. The estimated inner tube diameter of FWCNTs is about 2 nm. In FWCNTs, the RBM signal is weak because of the large diameter and the presence of more than one wall compared to SWCNTs. Nevertheless, RBM band in doped

FWCNTs might have broadened to such an extent that it could not be distinguished from the noise [25]. This could be the reason for a weak RBM mode which could not be probed in the acid treated FWCNTs with lower intensity of the incident laser.

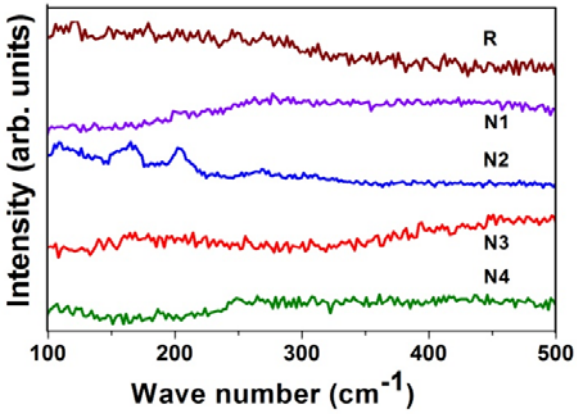

Figure 5.10: RBM of FWCNTs for each purification process

5.2.3 Excitation dependent Raman spectra of FWCNTs

The excitation energy dependent phonon dispersion study on FWCNTs provides information on the intrinsic nature and origin of Raman modes. Previous investigations using multiple excitation wavelengths have revealed that the G peak does not disperse because it is a fundamental Raman mode arising from a zone center phonon [13]. In contrast, disorder-induced D bands shift upward with increasing laser excitation energy and this indicates that the mode arises from inside the Brillion zone

The dispersive behavior of the D band can be explained by using a double resonance model from an intravalley scattering process as shown in fig.-5.11. In this figure, k and q represent electron and the phonon wave vectors, respectively and dotted line represents the elastic scattering vector. In the Raman process, laser excitation energy (E_L) dependent magnitude of k and q results in the observed dispersion of D band. Similarly, dispersion of the D′ band can also be explained by this model using an intervalley scattering process [11-13].

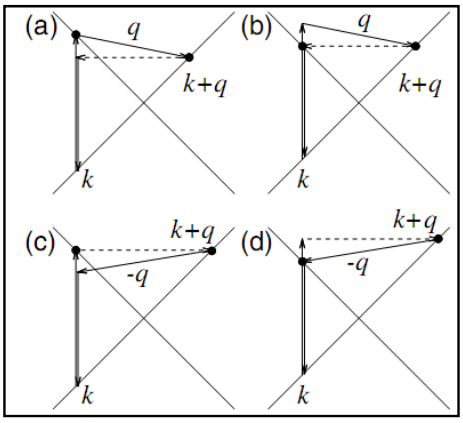

Figure 5.11: Four types of second-order double resonance Stokes processes for the D band. For each process, the dashed lines denotes an elastic scattering process and black dots are shown for the resonant points [13].

Though this model explains the phonon dispersion, it does not give a quantitative estimation of the intensity. Interestingly, it is observed that the intensity of the D band decreases with increasing laser energy. These results fall under the empirical relationship between the intensity ratio (I_D/I_G) and the correlation length (L_a) as formulated by Knight and White [26] and written as,

$$L_a = C\left(I_D/I_G\right)^{-1} \qquad 5.5$$

where, L_a is the in-plane correlation length and was used to find the defect concentration and C is a laser energy dependent parameter. In the forth coming sections, the D, G band peak positions and their intensity variations with respect to the different laser excitation energies of 1.58, 2.41 and 3.69 eV are discussed.

5.2.3.1 Peak shift

Fig.-5.12 (a) and (b) show the dispersion of the D and G band peak positions with respect to different excitation energies. The D band peak position increases nearly linearly with excitation energy and the peak position is not vary significantly with respect to the purification process. The dispersion of the D band is calculated by

$d\omega/dE_L$ for the samples treated by N1 to N4 processes and they are 49+1.8, 42+3.8, 45+2.3, 46+0.65 cm^{-1} respectively. Here, $d\omega/dE_L$ does not show any noticeable systematic variation between purification processes. This results ($d\omega/dE_L$) are in agreement with the literature on linear dispersion with a slope of ~50 cm^{-1} [13].

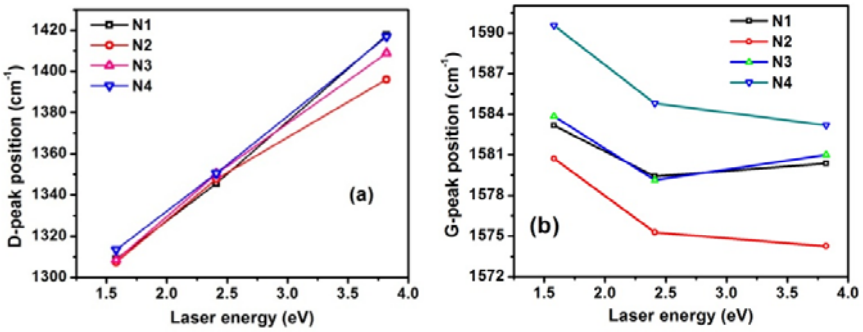

Figure 5.12: Energy dependent Raman peak shift for the (a) D-band and (b) the G-band

The analysis of the G band shift shows that the dispersion of the G band is small in comparison to the D band. For all excitations, the H_2O_2 treated samples have lower G peak values than the acid treated FWCNTs. This is consistent with the earlier discussion on a red shift occurring due to the lowering of nitronium ion concentration by H_2O_2 treatment. Hence, it can be concluded that irrespective of the laser energy used, the doping dependent G peak position follows the same trend.

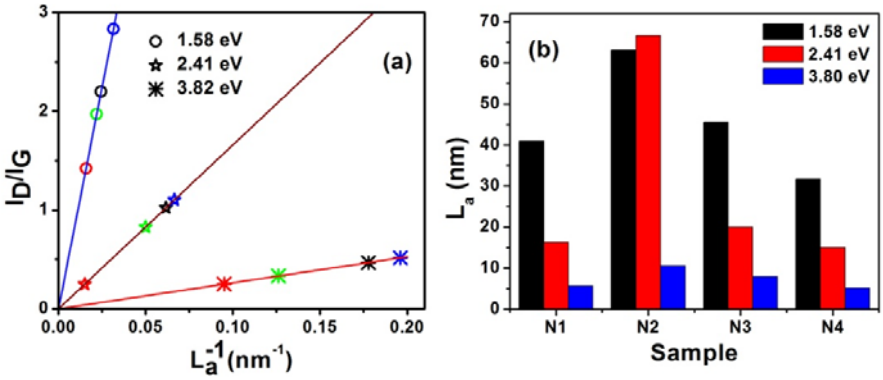

Figure 5.13: Excitation energy dependent (a) I_D/I_G is plotted with respective to L_a^{-1} for a set of FWCNTs. Here, the colors green, blue, red and cyan correspond to N1-N4 respectively and (b) Calculated L_a values for each purification step.

5.2.3.2 Peak intensity

The intensity of the Raman modes provides quantitative information about the quality of the CNTs. For example the in plane correlation length L_a is proportional to $(I_D/I_G)^{-1}$ but the intensity of the D band strongly depends on laser energy. Fig.-5.13a shows $1/L_a$ vs I_D/I_G values for the 1.58, 2.41, 3.81 eV laser excitation sources. A straight line fit to the data shows that the line passes through the origin. Here, zero defects are the indication of infinite L_a matching with theoretical prediction.

Tuinstra et al. [27] correlated the laser energy and intensity of the D band with an empirical formula, $I_D/I_G \ \alpha \ E_L^{-4}$ and the in plane correlation length (L_a) was estimated from,

$$L_a = \left(560/E_L^4\right) * \left(I_D/I_G\right)^{-1} \tag{5.6}$$

The plot between the calculated L_a from eqn-5.6 with different laser excitations is shown in fig.-5.13. In planar graphite, the excitation energy (E_L) dependency of L_a can be used for probing specific types of sp^2 clusters. In this view, the calculated L_a for FWCNTs could be due to preferential excitation of specific defects in FWCNTs. Soin et al.,[28] correlated the E_L dependent estimated magnitude of L_a with the tip diameter of aligned MWCNTs. In the present analysis, diameters of the FWCNTs are constant whereas, I_D/I_G values change with the chemical treatment. The H_2O_2 treated sample shows the higher correlation length. This is consistent with the higher quality of H_2O_2 treated FWCNTs. Further research is required to give a quantitative defect analysis and identify the specific nature of defects by E_L dependent study in CNTs.

5.3 Transport properties of FWCNTs

As discussed in chapter-1, a conduction mechanism in CNTs depends upon the CNTs chairality. The ballistic conduction of CNTs can suffer due to

intrinsic defects present in the tubes. On the other hand, a conduction mechanism of CNT networks are found to be affected by several factors, including the type of associated CNTs, defects, network density, interactions between tubes or bundles, bundle length and doping. In the present work, temperature dependent transport mechanisms of FWCNTs were undertaken and results correlated with structural properties.

5.3.1 Stabilization of the device: cyclic heat treatment

For transport measurements, the purified FWCNTs were spin coated on interdigitated Au electrodes deposited on an alumina substrate with 0.8 mm spacing between the electrodes. The coated FWCNTs contain adsorbed water molecules from the atmosphere, chemical impurities added during the purification process and volatile dispersing agents like ethanol or isopropyl alcohol. Hence, it is very important to remove these unwanted impurities from the sensor device. Moreover, in the network of spin coated CNTs, the tube-tube and electrode-tube contacts require initial annealing to enhance network integrity and hence to avoid erroneous signal. To demonstrate the stabilization of the device during heat treatment, the device was loaded in a quartz chamber and electrodes were connected to create a external electrical output. A K-type thermocouple was attached to the device. Both temperature and resistance were measured using a data logger. The measurements were carried out from 300-500 K under an Ar flow. Fig.-5.14 shows the variation of resistance with respect to different heating cycles. As can be seen from the plots, in the first heating cycle a large reduction in resistance was observed with increasing temperature whereas the subsequent heat cycles reduced the resistance further and after three cycle it almost stabilized. From repeated experiments on various test devices, it was observed that initial heating cycles are mandatory. Hence in all of our

transport measurements a heating cycle was used. The resistance of the FWCNT network showed semiconducting behavior in the temperature range studied.

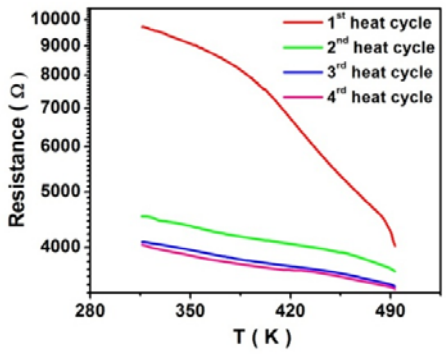

Figure 5.14: Temperature dependent resistance of FWCNT networks with four heating cycles in the range of 300-500 K.

5.3.2 Transport mechanism in FWCNTs network

From a detailed literature review it has been found that various transport models including power law, Luttinger liquid model, metallic conductivity, variable range hopping (VRH) and fluctuation induced tunneling (FIT) have been used to explain the conduction mechanism in SWCNTs and MWCNTs [8-10]. In spite of these suggested theories to explain the transport mechanism in CNTs, a comprehensive and consistent picture on this process invoking parameters pertaining to tube diameter and structure of CNTs in the network is still elusive. In present work, the electronic transport mechanisms in CNTs have been investigated in networks comprised of FWCNTs synthesized with optimized growth.

Two different samples were synthesized at 900 and 1000 ^{o}C and named as C900 and C1000 respectively. The morphology and size distribution of these as grown and purified FWCNTs were characterized by HRTEM. Further, the structural properties are studied by Raman Spectroscopy with laser excitation energy of 2.41 eV.

5.3.3 Structural study by HRTEM and Raman

Fig.-5.15 a&b shows typical HRTEM images obtained for samples C900 and C1000, respectively. The inset shows the magnified image of an individual tube and bundled tubes of C900 and C1000. Estimates made from HRTEM images show that the diameter of the FWCNTs are in the range of 5-10 nm and 3-8 nm for the samples grown at 900 and 1000 ^{o}C respectively. It should be noted that, in the preparation method of FWCNTs, the high temperature growth favors thinner tubes with a lesser number of walls.

Fig.-5.16 shows the first order Raman spectra recorded on samples C900 and C1000. These spectra indicate the presence of intense peaks corresponding to radial breathing modes (RBM) and also asymmetry in the G band. From eqn-5.4, the inner diameter of FWCNTs were estimated and found to be in the range 1.23 -1.67 nm and 1.37-1.51 nm for samples C900 and C1000, respectively. This confirms there is a narrow distribution in the inner wall diameter of the tubes and act as the origin of RBM.The estimated inner tube diameters from RBMs are in good agreement with values obtained from HRTEM analysis. In addition, it confirms that the observed RBMs originate from the inner walls of the FWCNTs, as no SWCNTs or DWCNTs are evidenced from HRTEM analysis.

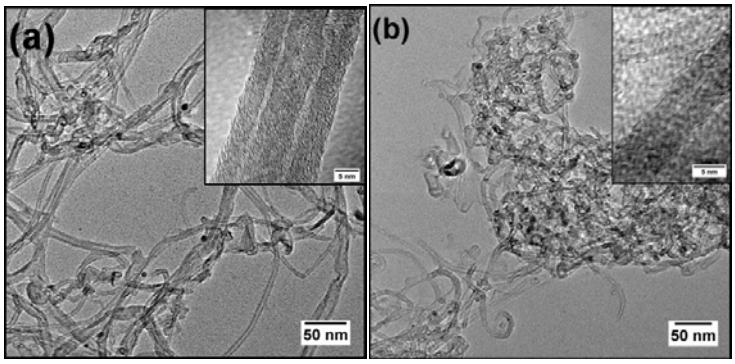

Figure 5.15 HRTEM images of the FWCNTs grown at (a) 900 ^{o}C (b) 1000 ^{o}C. The inset shows selected images of a single or bundle of CNTs.

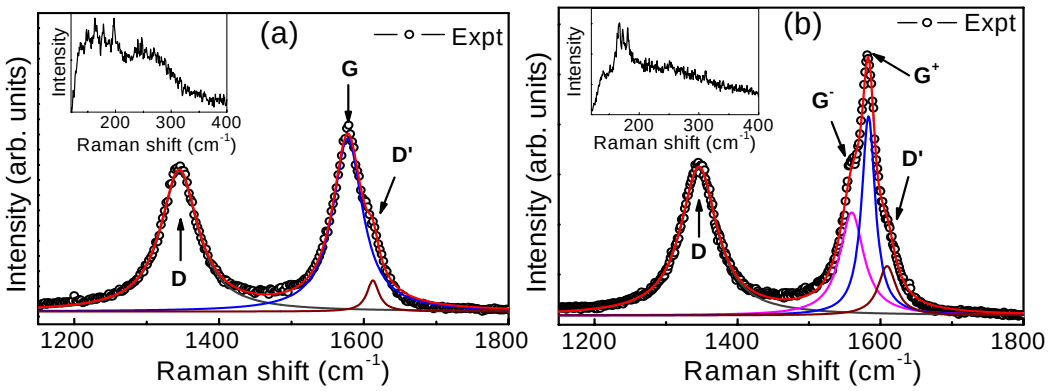

Figure 5.16. Raman spectra for FWCNTs for the samples (a) C900 and (b) C1000. The inset shows the presence of RBM modes. The arrows indicate the deconvoluted peak positions evaluated from a Lorentzian fit and shown as solid lines.

Hence, Raman spectra and HRTEM observations clearly establish that the numbers of walls in the FWCNTs are few owing to their small diameter and more importantly some inner diameters are in the limit of 2 nm satisfying the resonance condition to give rise to the RBM. It should be noted that the laser intensity and time has to be high enough to probe the weak RBM signals and here the experiments were performed with a laser power of about 5 mW.

Further, to carry out line shape analysis on the Raman spectra, the G and D bands were fitted with Lorenzian profiles. For sample C1000, the G band splitting could be deconvoluted into three peaks with centers at 1560, 1583 and 1609 cm^{-1} corresponding to G^-,G^+, and D' bands. The presence of D' is attributed to intercalation of the CNTs with other types of carbon in the sample. In the case of C900, the peaks are observed only at 1578 and 1612 cm^{-1} corresponding to G and D' bands. The absence of G splitting is an outcome of an averaging effect of the signals that emerge from a higher number of walls in C900 when compared to C1000. A qualitative estimate of the structural purity of the nanotubes can be obtained by calculating I_D/I_G. The calculated peak intensity ratio of D to G band is found to be 0.773 and 0.575 for

the samples C900 and C1000, respectively. These results reveal that the sample C1000 is less defective and exhibits better structural quality. In the subsequent discussion, how the information on structural defects was effectively utilized to predict the nature of the conducting mechanism in temperature dependent transport properties of the CNTs.

5.3.4 Temperature dependent transport mechanism

Fig.-15.17 shows the on the temperature versus normalized conductance measurements in the range of 5-200 K. It indicates that in both samples, the conductance decreases steeply at low temperatures exhibiting a semiconducting character. However, C1000 exhibited a poorer conductance than C900 at low temperatures and the resistance asymptotically approached a finite value as the temperature dropped to 5 K. Such behavior in C1000 implies the presence of a metallic component whose conductivity can be explained in terms of a FIT mechanism. However, in the case of C900, the conductivity does not appear to saturate as the temperature approaches to 0 K. Based on this behavior, the conductivity in C900 can be attributed to a hoping conduction mechanism which predicts the divergence of resistance at the limit of 0 K.

To proceed further in scrutinizing the possible conduction mechanism, various models including VRH and FIT were attempted to fit the experimental data. It was found that the best fit was achieved only with a combination of a FIT and a VRH model. The combined model can be written as,

$$\sigma(T) = \sigma_t exp\left[-\left(\frac{T_t}{T+T_s}\right)\right] + \sigma_0 exp\left[-\left(\frac{T_0}{T}\right)^{1/2}\right] \quad (5.7)$$

The first term represents the FIT model which predicts the conduction mechanism for disordered materials in which the thermal fluctuations induce

modulation of the tunneling barriers which play an important role in determining the dependence of the conductivity on temperature and electric field [29]. Further, $T_b = 2SV_0^2 / \pi k_B e^2 w$ is the activation energy required for an electron to tunnel through the insulating gap between conductive clusters. $T_s = 4\hbar SV_0^{3/2} / \pi^2 w^2 k_B e^2 \sqrt{2m}$ is the minimum temperature required to activate the thermal conduction to overcome the barrier. Here, S and w are the junction surface and width respectively, V_0 is the potential barrier height, and other parameters have their usual meaning. The second term in equation.5.5 indicates the Mott's variable range hopping conduction for disordered semiconductors [30].

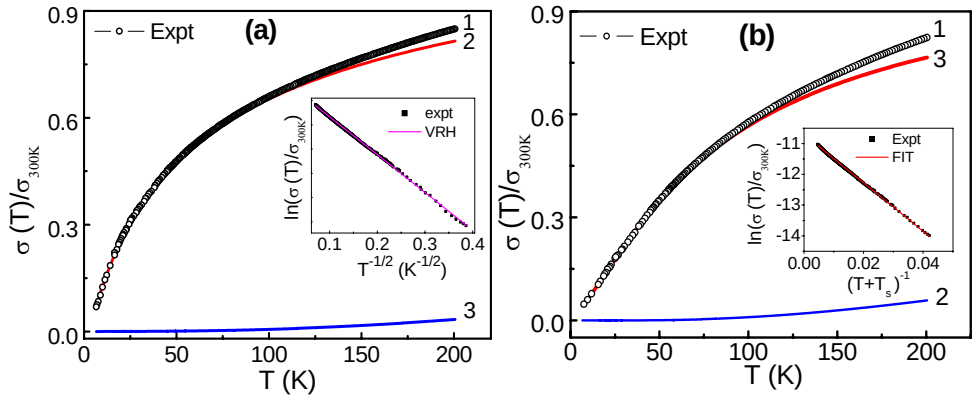

Figure 5.17. Temperature dependent conductance of FWCNTs networks (a) C900 (b) C1000. In both the plots, Curve 1 indicates experimental conductance, while, curves 2 and 3 are the contribution to the VRH and FIT mechanisms, respectively, as fitted with eqn 5.7. The inset shows the fit to the experimental data with (a) VRH and (b) FIT mechanisms respectively.

Fig.-5.17a and 15.17b show the fit to the experimental curve using eqn.-5.7 for samples C900 and C1000 respectively. The curves 1, 2 and 3 in the plots represent the experimental conductance in the network, and the individual contribution of VRH and FIT mechanisms, respectively. From these plots, it is very clear that one of the mechanisms dominates over the other in the conduction process. Thus, in sample

C900, it is observed that VRH is the dominant conduction mechanism with a small contribution from FIT. In contrast, in the case of sample C1000, it is the other way around. To evaluate the validity of these models, the experimental data is also independently fitted to one of the dominant conduction mechanism; either VRH or FIT (inset in the fig.-15.17a&b). A linear fit to semi logarithmic conductance vs temperature can highlight the dominant mechanism present in the system. Herein it was found, the best fit was achieved only by invoking both mechanisms in parallel. The parameters evaluated from the best fit are comparable to the reported values of the respective models. In order to confirm the effect of contact resistance on the conduction mechanism, the measurements were repeated with a four probe technique and the results are shown in fig.-5.18. The data agree well with the two probe measurements. Hence, the possible influence of contact resistance between the electrodes and CNT bundles is ruled out. The discussion was further extended to show how the conduction mechanism corroborated the Raman observation on structural defects.

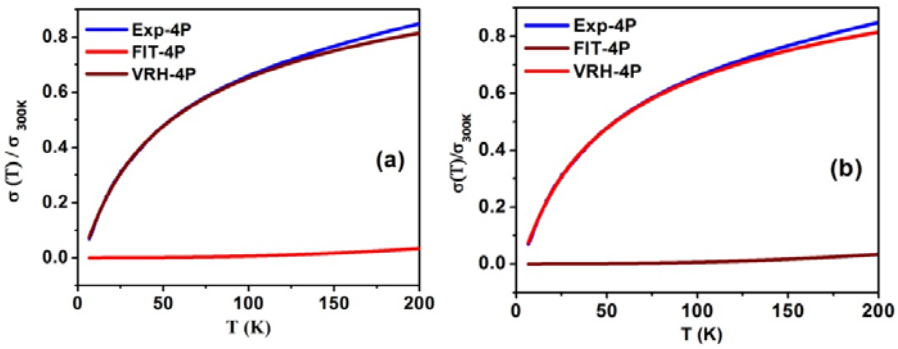

Figure 5.18: Temperature dependent conductance of FWCNT networks measured using a four probe method for (a) C900 (b) C1000.

The effect of temperature on resistance in CNT networks have been investigated by many research groups [9, 31-35]. In all these studies, it was noted that the reasons for the choice of a particular model to fit the experimental data is not

always explicit and clear. Since both sample contains FWCNTs with a similar diameters and number of walls, the observed difference in their dominant mechanism clearly indicated that the conduction mechanism is not entirely dependent on wall number alone. Among many possibilities to account for this phenomenon is that of the interrelation of structural defects and electrical conduction. Based on this, possible structural defects that could arise from the synthesis condition was explored. Indeed, the structural defects vary with growth conditions, as observed for C900 and C1000 with difference in their growth temperatures could possibly influence the conduction mechanisms. In view of this, a systematic analysis of the Raman data available in the literature in addition to the present study was performed. This analysis provided adequate information to understand the structural defects of CNTs as seen by their I_D/I_G ratio. This in turn correlated with the electrical conduction from the following important observation. While the tube diameters do not vary significantly between the samples, as found from HRTEM, the structural defects varied substantially as indicated by Raman spectra. Herein, it is interesting to note the I_D/I_G ratio can be uniquely used as a measure of structural defects and gives the clue for the possible conduction mechanism. Hence, based on these observations and analysis, it can be concluded that structural perfection plays an important role in determining the transport mechanism of FWCNT networks. While FWCNTs with larger I_D/I_G ratio follow a VRH mechanism, tubes with less structural defects follow a FIT mechanism. Thus, the transport mechanism in CNTs does not only rely on the number of walls, but also significantly influenced by structural defects.

5.4 Summary

FWCNTs were extensively investigated by Raman spectroscopy, FTIR spectroscopy and HRTEM. Curvature induced shifts in the G band and the presence

of RBM in FWCNTs were found to have different features when compared to MWCNTs. The structural quality of FWCNTs are evaluated by Raman spectroscopy using I_D/I_G and $I_{D'}/I_G$ ratios. This analysis showed that H_2O_2 treatment in a multi step purification process give high quality FWCNTs when compared to acid treatment. Further, a blue shift in the G band of the acid treated FWCNTs showed hardening of phonons due to p type doping by intercalation. FTIR spectra were recorded after every purification step and N1-N4 showed progressive functionalization of the surface by carboxylic groups. Corroborating the Raman and FTIR spectra, it can be concluded that acid treatment yielded amorphous carbon, functionalization and intercalation whereas H_2O_2 treatment oxidized amorphous carbon, functionalize CNT walls and recovered intercalated acid molecules from FWCNTs. Further, HRTEM analysis showed the removal of fullerene caps from prolong room temperature oxidation.

A multi wavelength laser excitation study provided an understanding of the phonon dispersion in FWCNTs. The wavelength dependent dispersion in the D band substantiated that the modes originated from a non-zone center phonon. Further, the intensity of the D band and the in plane correlation length showed the lower defects with increasing laser energy. This could be due to an excitation energy dependent activation of defects.

The transport properties of the FWCNTs grown at two different temperatures viz. 900 and 1000^o C were studied. Their respective diameters were found to be in the range of 5-10 and 3-8 nm. The conduction mode in FWCNTs was found to be predominantly influenced by FIT and VRH mechanisms respectively and corroborated with Raman studies on structural defects. These investigations revealed that the dominant conduction mechanism in FWCNTs depends not only on the number of walls but were also highly influenced by structural defects.

5.4 References

[1] E. Snow, *et al.*, "Random networks of carbon nanotubes as an electronic material," *Applied physics letters,* vol. 82, p. 2145, 2003.

[2] L. Langer, *et al.*, "Quantum Transport in a Multiwalled Carbon Nanotube," *Physical Review Letters,* vol. 76, p. 479, 1996.

[3] H. Dai, *et al.*, "Probing electrical transport in nanomaterials: conductivity of individual carbon nanotubes," *Science,* vol. 272, p. 523, 1996.

[4] P. Poncharal, *et al.*, "Room temperature ballistic conduction in carbon nanotubes," *The Journal of Physical Chemistry B,* vol. 106, p. 12104, 2002.

[5] A. Urbina, *et al.*, "Quantum Conductance Steps in Solutions of Multiwalled Carbon Nanotubes," *Physical Review Letters,* vol. 90, p. 106603, 2003.

[6] R. Graupner, *et al.*, "Doping of single-walled carbon nanotube bundles by Brønsted acids," *Phys. Chem. Chem. Phys.,* vol. 5, p. 5472, 2003.

[7] S. Frank, *et al.*, "Carbon nanotube quantum resistors," *Science,* vol. 280, p. 1744, 1998.

[8] F. Jing-Hai, *et al.*, "Hopping Conductivity in a Single-Walled Carbon Nanotube Network," *Chinese Physics Letters,* vol. 23, p. 953, 2006.

[9] M. Salvato, *et al.*, "Charge Transport and Tunneling in Single-Walled Carbon Nanotube Bundles," *Physical Review Letters,* vol. 101, p. 246804, 2008.

[10] E. Kymakis and G. A. J. Amaratunga, "Electrical properties of single-wall carbon nanotube-polymer composite films," *Journal of applied physics,* vol. 99, p. 084302, 2006.

[11] C. Thomsen and S. Reich, "Double resonant Raman scattering in graphite," *Physical Review Letters,* vol. 85, p. 5214, 2000.

[12] R. Saito, *et al.*, "Double resonance Raman spectroscopy of single-wall carbon nanotubes," *New journal of Physics,* vol. 5, p. 157, 2003.

[13] M. S. Dresselhaus, *et al.*, "Raman spectroscopy of carbon nanotubes," *Physics Reports,* vol. 409, p. 47, 2005.

[14] H. Hiura, *et al.*, "Raman studies of carbon nanotubes," *Chemical physics letters,* vol. 202, p. 509, 1993.

[15] P. Eklund, *et al.*, "Vibrational modes of carbon nanotubes; spectroscopy and theory," *Carbon,* vol. 33, p. 959, 1995.

[16] Z. Ni, *et al.*, "High temperature Raman spectroscopy studies of carbon nanowalls," *Journal of Raman Spectroscopy,* vol. 38, p. 1449, 2007.

[17] I. Mironyuk, *et al.*, "Magnesia formed on calcination of Mg $(OH)_2$ prepared from natural bischofite," *Applied surface science,* vol. 252, p. 4071, 2006.

[18] S. Niyogi, *et al.*, "Chemistry of single-walled carbon nanotubes," *Accounts of Chemical Research,* vol. 35, p. 1105, 2002.

[19] Y. Feng, *et al.*, "Room temperature purification of few-walled carbon nanotubes with high yield," *ACS nano,* vol. 2, p. 1634, 2008.

[20] Y. Peng and H. Liu, "Effects of oxidation by hydrogen peroxide on the structures of multiwalled carbon nanotubes," *Industrial & engineering chemistry research,* vol. 45, p. 6483, 2006.

[21] M. S. Dresselhaus and G. Dresselhaus, "Intercalation compounds of graphite," *Advances in Physics,* vol. 51, p. 1, 2002.

[22] S. Osswald, *et al.*, "Monitoring oxidation of multiwalled carbon nanotubes by Raman spectroscopy," *Journal of Raman Spectroscopy,* vol. 38, p. 728, 2007.

[23] M. A. Hoefer and P. R. Bandaru, "Defect engineering of the electrochemical characteristics of carbon nanotube varieties," *Journal of applied physics,* vol. 108, p. 034308, 2010.

[24] D. Y. Kim*, et al.*, "Characterization of thin multi-walled carbon nanotubes synthesized by catalytic chemical vapor deposition," *Chemical physics letters,* vol. 413, p. 135, 2005.

[25] F. A.G.S*, et al.*, "Raman spectroscopy for probing chemically/physically induced phenomena in carbon nanotubes," *Nanotechnology,* vol. 14, p. 1130, 2003.

[26] D. S. Knight and W. B. White, "Characterization of diamond films by Raman spectroscopy," *Journal of Materials Research,* vol. 4, pp. 385-393, 1989.

[27] F. Tuinstra and J. L. Koenig, "Raman spectrum of graphite," *The Journal of Chemical Physics,* vol. 53, p. 1126, 1970.

[28] N. Soin*, et al.*, "Excitation energy dependence of Raman bands in multiwalled carbon nanotubes," *Journal of Raman Spectroscopy,* vol. 41, p. 1227, 2010.

[29] P. Sheng*, et al.*, "Fluctuation-induced tunneling conduction in carbon-polyvinylchloride composites," *Physical Review Letters,* vol. 40, p. 1197, 1978.

[30] B. I. Shklovskii and A. L. Efros, *Electronic properties of doped semiconductors*: Springer-Verlag, 1979.

[31] W. Zhou*, et al.*, "Single wall carbon nanotube fibers extruded from super-acid suspensions: Preferred orientation, electrical, and thermal transport," *Journal of applied physics,* vol. 95, p. 649, 2004.

[32] Z. Li*, et al.*, "Does the wall number of carbon nanotubes matter as conductive transparent material?," *Applied physics letters,* vol. 91, p. 053115, 2007.

[33] Z. H. Khan, *et al.*, "Electrical transport via variable range hopping in an individual multi-wall carbon nanotube," *Journal of Physics: Condensed Matter,* vol. 20, p. 475207, 2008.

[34] M. Aggarwal, *et al.*, "Variable-range hopping in Fe 70 Pt 30 catalyzed multi-walled carbon nanotubes film," *The European Physical Journal B-Condensed Matter and Complex Systems,* vol. 60, p. 319, 2007.

[35] W. Y. Jang, *et al.*, "Electrical characterization of individual carbon nanotubes grown in nanoporous anodic alumina templates," *Applied physics letters,* vol. 84, p. 1177, 2004.

Chapter-6 Study and development of decorated FWCNTs for gas sensor applications

6.1 Introduction

Chemical sensors working on the basis of a change in resistance are called chemiresistors. They have been in use for the high sensitive detection of a wide range of species such as, toxic gases, nerve agents, explosives and environmental pollutants. The transport properties of CNTs are amazing and the whole surface of a CNT act as a reactive material that offers great potential applications as a novel gas sensor material. The use of carbon nanotubes for sensing technology has attracted intensive research interest in the past several years because interactions between target molecules and CNTs can significantly change their electronic properties like capacitance and resistance, even at room temperature [1-2].

Toxic gases or other molecules present in the atmosphere can be adsorbed on the walls of CNTs and can modify the overall electrical conductivity of the CNT either by donating or accepting charge carriers [3-4]. Hence, the change in conductance depends on the gas adsorption kinetics on a CNT and their charge transfer capabilities. It has been shown that using functional property of CNTs the chemically inert sidewalls can be modified by functionalization and decoration of nanoparticles to improve its sensitivity and sensing performance [5-6].

Metals exhibit a broad range of electronic, chemical and physical properties that are often highly sensitive to changes in their chemical environment [7-8]. CNTs decorated with Pd, Pt, Au, Rd nanoparticles have been widely reported to sense a wide range of gas molecule. In a metal decorated CNT, metal cluster surfaces and interfaces between metal and CNTs act as reactive sites for the adsorption of the

target molecules and can enhance the charge transfer process into CNTs. Among the metals, Pd nanoparticles are often used in hydrogen sensors. The CNTs assist in maintaining the dispersion of Pd nanoparticle and enhance the sensing nature of CNTs.

On the other hand, metal oxides are well-known materials for detecting a wide spectrum of gases with adequate sensitivity. SnO_2, ZnO and TiO_2 are commonly used metal oxides for chemical gas sensor applications. Among these many metal oxides, SnO_2 has been proved to be a very suitable candidate due to its superior properties. The advantages of a sensor fabricated using SnO_2 includes high sensitivity, simple design and low cost. However, in general, the metal oxide based sensors need to be operated at elevated temperature to exhibit an appreciable sensitivity for toxic species [9]. Hence, their sensing properties often suffer a degradation resulting from the growth and aggregation of nanoparticles. Thus, considerable research has been carried out to improve its gas-sensitivity as well as to reduce the operating temperature. This can be achieved by introducing dopants or down scaling the SnO_2 particle size to the nanoscale regime, typically below 10 nm. CNTs are found to be an efficient material for decoration with SnO_2 since growing fine sized nanoparticles and also for maintaining their dispersion. This chapter focuses on the sensor properties of Pd and SnO_2 decorated FWCNTs.

Apart from their use as chemiresistive gas sensors, the high aspect ratio of CNTs enables the emission of electrons at low operating voltage. Hence, it is possible to make a more sensitive and selective ionization gas sensor for a wide range of gases [10]. In view of this, to demonstrate their field emission properties, CNT mat has been synthesized and studied with respect to their morphology.

6.2 FWCNTs gas sensor

This section discusses the gas sensing property of pure FWCNTs for a on wide range of gases viz. NO_2, N_2O, CH_4, H_2 and NH_3. FWCNTs synthesized using Fe and Mo as catalyst on a MgO support at 900 ^oC were used for the present investigation. For sensor device fabrication, the FWCNTs were dispersed in isopropyl alcohol with a solution concentration of 1 μg/ml. The dispersion was then spin coated at 2000 rpm on an interdigitated electrode patterned on an alumina substrate. This configuration act as a device that consists of a random network of FWCNTs spread across the electrodes. The electrical conductivity measurements of the sensor were carried out in an argon atmosphere. The sensor was placed in a confined quartz tube and the change in the resistance of the sensor on dosing with analyte gases was recorded with a high precision multimeter HP34401A with time tag. The measurements were repeated several times to evaluate the consistency of the device performance and found to show excellent repeatability.

Fig.-6.1(a-d) shows the gas sensing behavior of the FWCNT network for NO_2, N_2O, CH_4, and H_2 gases. Here, the sensor response is plotted with respect to time. The response is defined as,

$$r = \frac{(R - R_i)}{R_i} * 100 \tag{6.1}$$

where, R is the dynamic resistance of the sensor during exposure to the test gas and R_i (1.2 kΩ) is the initial resistance measured before exposure to the test gas. All the measurements were made under a dynamic flow of gas. Periodic measurements were made with respect to gas concentration. In each cycle, the ‘on’ state means the analyte

gas was sent to the device mixed with Ar while the 'off' state means only Ar is sent through the device for recovery.

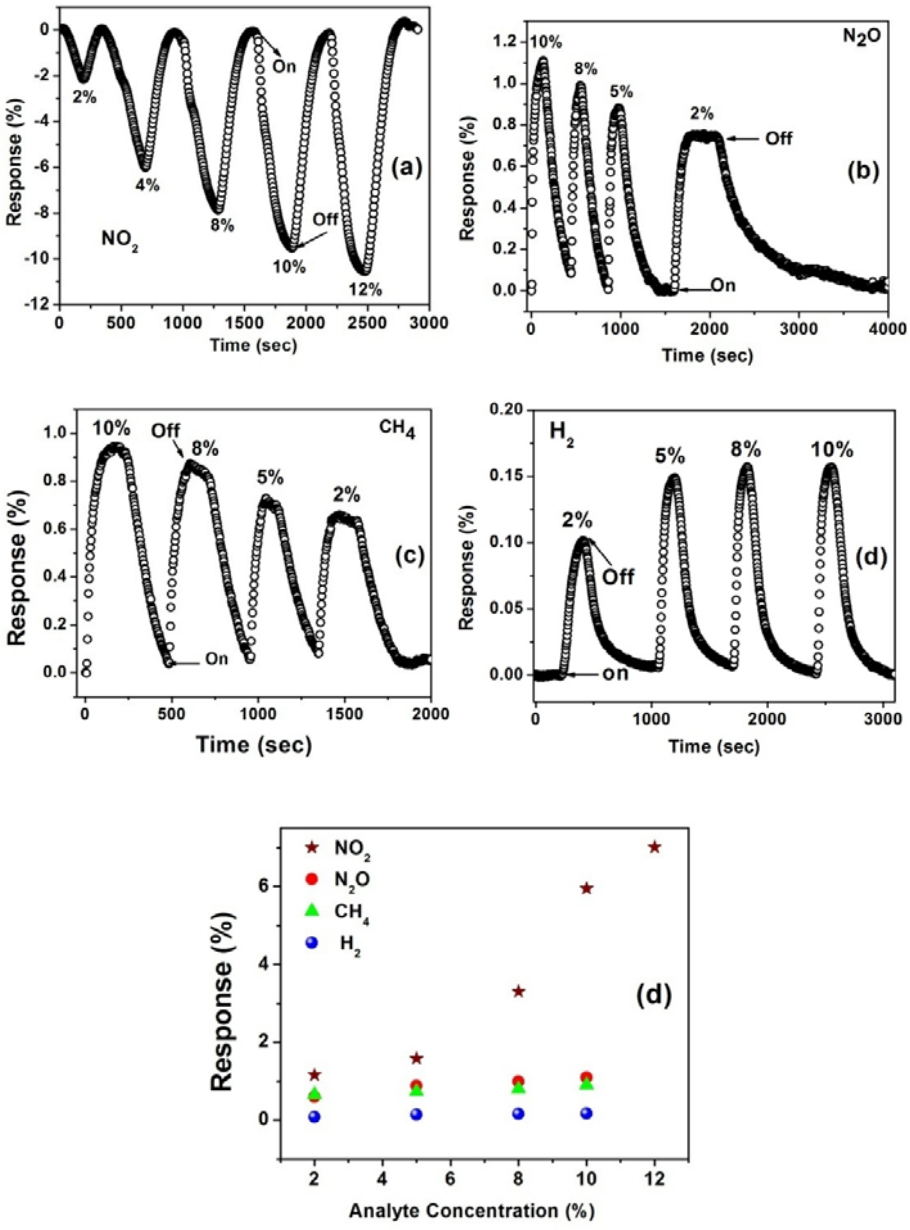

Figure 6.1 Gas sensor responses of the FWCNTs for (a) NO_2 (b) N_2O (c) CH_4 and (d) H_2. (e) Comparison of the concentration dependent response of the above studied gases

6.2.1 Qualitative analysis

Observation of the sensor response showed that upon exposure to an oxidizing gas such as NO_2, the resistance increased whereas the resistance decreased for reducing gases such as N_2O, CH_4, and H_2 as shown in fig.-6.1 (a-d). The figure shows that the chemical environment changed the electronic structure of the FWCNTs. In a CNT random network, adsorption of electron donor/acceptor gas molecules renders a change in conduction properties by intratube and intertube modulation by charge transfer [11-12]. In intratube interaction charge transfer affects the transport property of the individual nanotubes whereas adsorption of gas molecule in the nanotube-nanotube junctions alters the intertube interaction in the network and thus affects the hopping/ FIT mechanism. However, in the present work, only the macroscopic variation of the electrical behavior of the CNTs network was studied.

The adsorption of electron-withdrawing (NO_2) gas molecules or electron-donating (N_2O, CH_4, H_2 and NH_3) gas molecules in a CNTs network causes an electrical charge transfer between the FWCNTs and target gas molecules. It is widely reported that functionalilation by acid treatment and oxygen adsorption from the atmosphere leads to an injection of holes in to CNTs. Hence, the Fermi level shifts towards the valance band and makes the device behave like a p-type semiconductor [13-14]. Hence, an electron-withdrawing (NO_2) gas adsorbed onto the surface of the FWCNTs network increases the density of holes in the valence band. Consequently, the Fermi level shifts further towards valence band and thus decreasing the electrical resistance. On the other hand, the adsorption of electron-donating (N_2O, CH_4, H_2 and NH_3) gases causes the number of holes to decrease as well as Fermi level to shift from the valence band increasing their band separation, and thus increasing the electrical

resistance. These results clearly demonstrate a p-type semiconducting behavior of the CNT network. Hence, FWCNTs can detect gases and selectively distinguish between oxidizing and reducing type of molecule. The quantitative analysis of the sensitivity and selectivity among the oxidizing/ reducing gases, with these gas sensors is discussed below.

6.2.2 Quantitative response

A quantitative response of the sensor depends on the charge transfer and adsorption kinetics between analyte molecules and CNTs. The sensor responses are calculated after 120 sec exposure for NO_2, N_2O, CH_4, H_2 & NH_3 and as shown in fig.-6.1d and 6.2b. For the exposure of 2-10 % NO_2, the response varies from 1- 6%. In contrast, sensor responses for reducing agents are in the range 0.6-1% for N_2O & CH_4 and 0.08 to 0.16% for H_2, respectively. It shows that the response is almost the same for N_2O & CH_4 and is hardly detected for H_2 gas. Zhao et al. [4] studied the adsorption of various gas molecules such as NO_2, O_2, NH_3, N_2, CO_2, CH_4, H_2O, H_2, and Ar on single SWCNT and SWCNT bundles using a first principles method. Their results showed that adsorption of these gas molecules can be identified as physisorption with a small charge transfer (0.01 ~ 0.035 e) and weak binding energy (≤0.2 eV). It was shown that NO_2 a charge acceptor with a relatively large charge transfer and higher adsorption energies when compared to all other donor molecules that were studied. These observations are consistent with the experimental results that follow the order $NO_2 > CH_4 > H_2$. Fig.-6.2a shows the sensor response for NH_3 gas at the ppm level. Among the reducing gases studied here, NH_3 showed the highest response for the FWCNT device. This shows the strong perturbation of the electron transport in a FWCNT network by NH_3 molecules. In the following section the

discussion is continued on the effect of an applied potential on the sensing property of FWCNTs for NH_3.

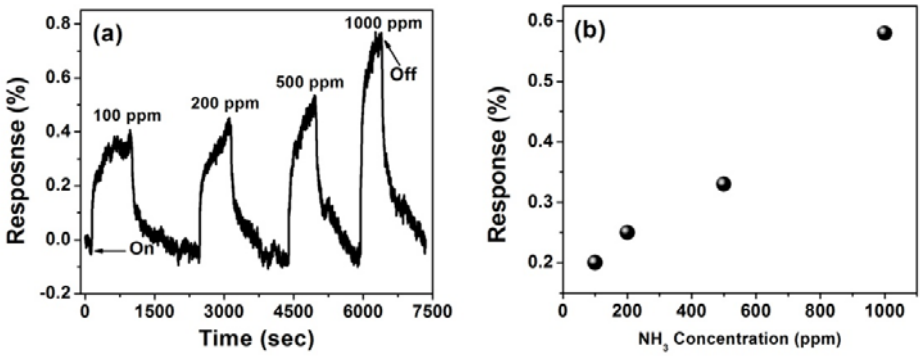

Figure 6.2: Concentration dependent FWCNTs NH_3 gas sensor (a) time dependent response and (b) quantitative comparison of response at 120 sec.

6.2.3 Bias dependent sensor response

It was shown in chapter-4 that the transport property of a CNT random network depends on a tunneling or hopping mechanism. Hence, it is possible that an applied potential can enhance the charge transport. To study this behavior, the sensor response was also measured by applying a constant bias to the device and monitoring the current variation in the presence of an analyte gas. The characteristic response of the sensor measured with constant biases at 0.1 V, 0.5 V and 1 V for 100 ppm NH_3. The measured current was converted into resistance by Ohms law and is shown in fig.-6.3 along with the default resistance measurement. The observed responses are 0.17 %, 0.33 %, 0.42 % at 0.1 V, 0.5 V and 1 V respectively for 100 ppm of NH_3. The sensor response is about 0.21% by default resistance measurement from the multimeter for the same amount of gas. Hence it is obvious that the device response increases with respect to the applied bias.

To understand the voltage enhanced sensing property further, I-V measurements were taken at 300 and 4.2 K and shown in fig.-6.4a&b, respectively. As can be seen,

the I-V curve measured at 300 K is almost linear, whereas non linear behavior was observed at low temperature.

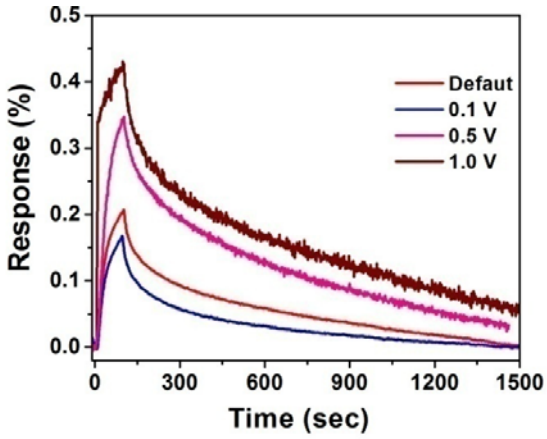

Figure 6.3: Bias voltage dependent responses of the FWCNTs sensor for 100 ppm of NH_3

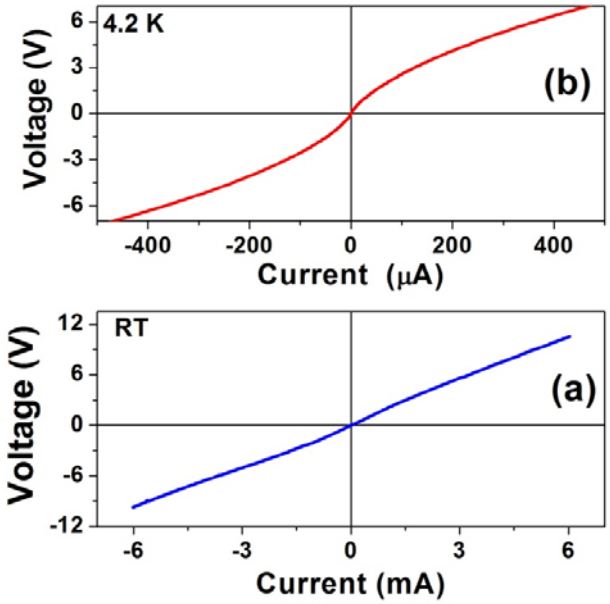

Figure 6.4: I-V characteristics of FWCNTs at (a) 300 K and (b) 4.2 K

The deviation from Ohms law shows that the conduction enhancement in the network is from the higher applied potential. This fact clearly indicates the presence

of a voltage dependent activation behavior in FWCNT random networks. This may be due to Joule heating, a change in Schottky barrier or a transport mechanism. In our study, to remove the possibility of Joule heating the measurements were repeated with different sweep rates. It was found that the results are same irrespective of the sweep rate. Further, the Ohmic conduction at RT shows the absence of a Schottky barrier between the metal electrode and the FWCNTs. Hence, the non-linear behavior in current transport at low temperature is anticipated to be due to the presence of an activation dependent diffusive conduction mechanism such as FIT and VRH [15-17]. The presence of combined FIT and VRH mechanisms in a FWCNTs network was discussed in chapter-4.

From the above studies, a p-type sensing property of a FWCNT gas sensor was demonstrated at RT. The sensor is able to clearly distinguish oxidizing and reducing gases. However selectivity is not appreciable among similar types of gases. Further, the charge transfer and adsorption energy dependent conducting properties yield a poor response for inert gases. In the next section, the discussion follows for enhancing sensing property of FWCNTs by metal or metal oxide decoration.

6.3 Decorated FWCNTs as gas sensors

This section deals with FWCNTs decorated with Pd and SnO_2 to enhance the sensor response. To make the inert FWCNT walls wettable to Pd and SnO_2, it is necessary to functionalize the FWCNT walls to create nucleation sites. The schematic diagram for the functionalization and decoration of a CNT is given in fig.-6.5. To achieve functionalization, the FWCNTs are treated with a $1HNO_3$: $3H_2SO_4$ mixture as detailed in chapter-4 (sample-N4). The wet chemical routes for decoration of FWCNTs were given in chapter-3. In the forthcoming sub-sections, characterization of the Pd and SnO_2 decorated FWCNTs and their sensor properties are discussed.

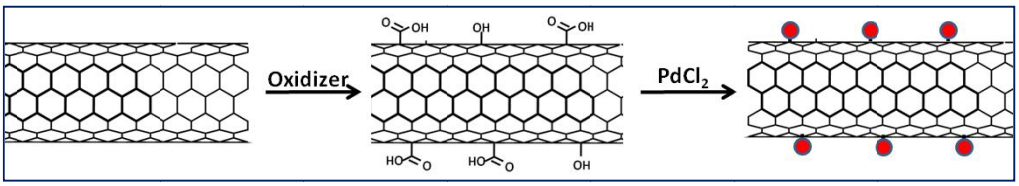

Figure 6.5: Schematic representation of functionalization and Pd decoration of CNT.

6.3.1 Pd decorated FWCNTs as a H_2 sensor

The development of room temperature (RT) hydrogen detectors are essential for industrial application [18]. For this purpose, CNTs are considered as a potential functional material. On the other hand, as discussed in section-6.2.2, the sensitivity of FWCNTs for H_2 is very small. Hence, to improve the sensitivity, FWCNTs can be decorated with Pd nanoparticles and their characteristic sensing properties studied.

6.3.1.1 Structural Characterization

The morphological features of the purified and decorated FWCNTs were studied by HRSEM and the results are shown in fig.-6.6a&b. Spherical Pd nanoparticles of diameter 5-10 nm are clearly seen on the decorated FWCNTs. These nanoparticles are attached discretely onto the FWCNTs.

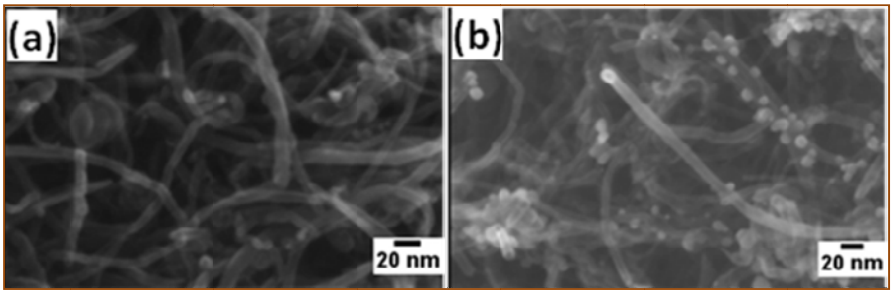

Figure 6.6: HRSEM morphology of (a) pure FWCNTs and (b) Pd decorated FWCNTs

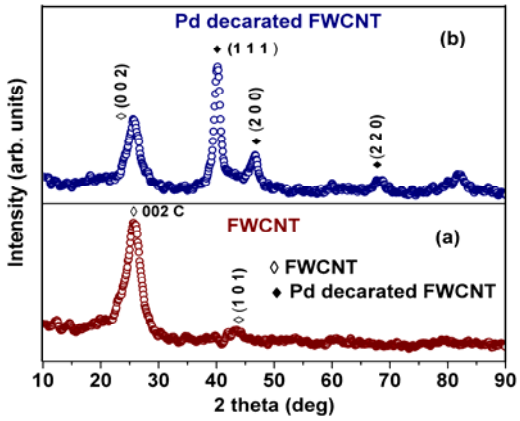

Figure 6.7: Powder XRD pattern of (a) pure FWCNTs and (b) Pd decorated FWCNT

The XRD patterns of pure and decorated FWCNTs are shown in fig.-6.7a&b. The XRD pattern of the pure FWCNTs shows the intense (002) peak at 24^{o} (2θ) corresponding to the graphitized carbon and after Pd decoration new peaks arise corresponding to the face center cubic crystalline structure of Pd (JCPDS-7440053). Crystallite size was estimated using the Scherrer formula and found to be 10 nm. From XRD and SEM characterization it is shown that crystalline Pd nanoparticles were discretely dispersed on the FWCNTs. Hence conduction between metallic particles is possible through the CNTs. To explore the transport property of this Pd-FWCNT hybrid material, temperature transport properties were measured and discussed below.

6.3.1.2 Temperature dependant transport properties

The Pd-FWCNT random network was prepared. The resistance of the device is about 800 Ω which is a much lower resistance than the undecorated FWCNTs (1.2 kΩ) prepared under similar conditions. The temperature dependent transport behavior is shown in fig.-6.8. As found for the FWCNT random network, the Pd-FWCNTs also exhibit a semiconducting nature over the entire measured temperature

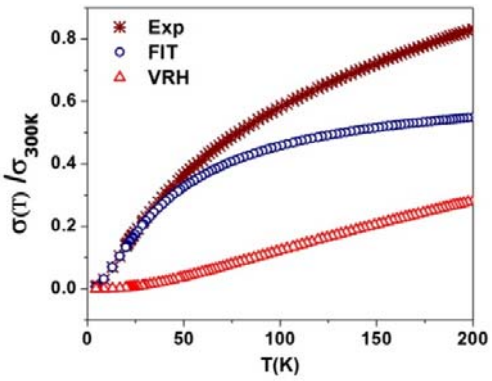

Figure 6.8: Temperature dependent conductance of the Pd-FWCNT networks. Here, curve 1 indicates experimental conductance, curves 2 and 3 are the contribution of the FIT and VRH mechanism, respectively.

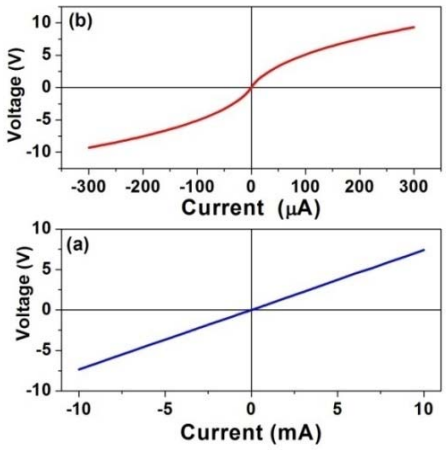

Figure 6.9: I-V characteristics of Pd-FWCNTs at (a) room temperature and (b) 4.2 K

regime (4.2-300 K). It is noted that the decoration of Pd did not introduce metallic behavior ($\sigma \alpha T^{-1}$) in the network. This is due to the discrete decoration of Pd nanoparticles without exceeding the percolation threshold. A best fit to the experimental data with equation-5.7 over the range 4.2 to 200 K shows that the transport behavior follows a combination of a FIT and VRH mechanism. To determine their the bias dependent activation behavior, their I-V characteristics were

studied. I-V plots in fig.-6.9a&b show nonlinear behavior at 4.2 K which becomes almost linear at RT. Hence, their transport behavior is similar to that of FWCNTs. The gas sensing characteristics of this hybrid material is discussed below.

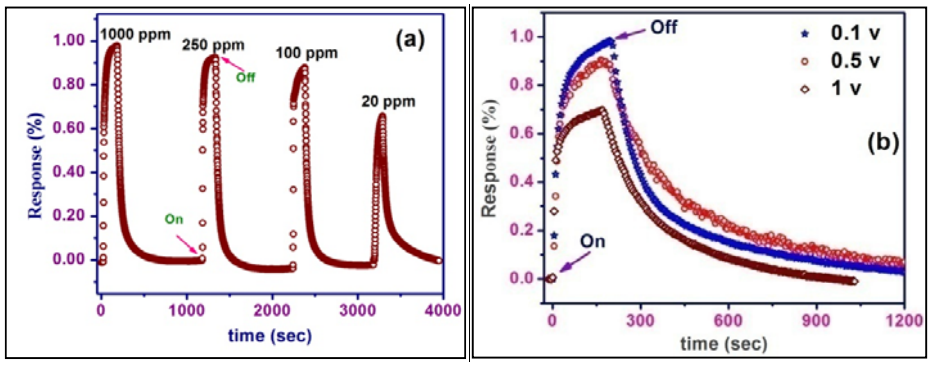

Figure 6.10 Sensor response of the hybrid Pd-FWCNTs for H_2 at room temperature (a) concentration dependent and (b) bias dependent at 100 ppm.

6.3.1.3 Gas sensor analysis

Fig.-6.10a shows the response of the Pd decorated FWCNTs to hydrogen gas at room temperature. Similar transport properties of Pd-FWCNTs and FWCNTs are due to the p type semiconducting behavior of the network. On the other hand, as shown in the fig.-6.10a enhanced sensor responses are observed even for concentration as low as 20 ppm. Nevertheless, the sensor response of pure FWCNTs is about 0.16% for 10% of H_2 gas and it is insensitive to ppm levels of H_2. A multifold enhancement of response is observed after decoration with Pd and the response increased to 0.8% even at 100 ppm. The reason for such a high response can be understood. Pd has a high affinity for hydrogen atoms which occupy the octahedral interstitial positions within the face centered cubic (FCC) lattice structure and hence Pd can form Pd hydride. This can be recovered into Pd in room temperature. The decorated Pd donates a large number of electrons into the FWCNTs due to a spillover

effect from Pd hydride and this increases the FWCNTs resistance drastically [19]. Hence, the Pd-FWCNT exhibit an improved response over pure FWCNTs.

The bias dependent sensor response is shown in fig.-6.10b. The sensor response increased with respect to bias voltage. The responses for 100 ppm of H_2 were 0.68, 0.87 and 0.93% for applied voltages of 0.1, 0.5 and 1 V, respectively in 120 sec. Hence, Pd-FWCNTs also shows a voltage dependent enhancement which might be due to enhanced conduction by voltage dependent activation behavior as found for the FWCNT network as discussed in section-6.3.

In conclusion, Pd decorated FWCNTs shows p type semiconducting behavior. Temperature dependant transport properties show a combined FIT and VRH mechanism. Further, Pd decoration enhances the sensing property of the FWCNTs to H_2 gas.

6.3.2 SnO_2 decorated FWCNTs as a selective gas sensor

As discussed earlier, combining the advantage of the materials in the form of hybrid structures could lead to a novel functional material. To utilize the well known properties of the metal oxides, their combination with CNTs was explored. In this thesis, FWCNTs and SnO_2 were added together to give a hybrid structure to form discretely decorated SnO_2 on the walls of FWCNTs.

SnO_2 is an n-type metal oxide semiconductor with a wide band gap of about 3.6 eV [20]. Many groups have investigated MWCNT-SnO_2 combinations for sensing ethanol at elevated temperature and found that it behaves like a *n*-type semiconductor [21-22]. Hiey et al. [23] reported room temperature SnO_2-MWCNT composites could be used as a ammonia gas sensor and show a *p*-type behavior. In the report, the possibility of using discrete SnO_2 decorated MWCNT as a room temperature gas sensor was demonstrated by Lu et al., [24]. In the current study the hybrid property of

the discretely decorated SnO_2 on FWCNT was explored and their temperature dependent gas sensing property was investigated in detail.

6.3.2.1 Structural Characterization

The detailed procedure for decoration of SnO_2 on FWCNTs was given in chapter-3. Fig.-6.11 shows the HRSEM and HRTEM images of the bare and SnO_2 decorated FWCNTs. HRSEM images reveal that the walls of FWCNTs are uniformly decorated with SnO_2 nanoparticles. Further investigation by HRTEM studies clearly showed that the SnO_2 nanoparticles had a (1 1 0) orientation with a 0.34 nm lattice spacing. These particles are well separated on the FWCNT walls and were decorated in an isolated fashion leaving a considerable surface area of the FWCNTs walls exposed for molecular interaction. Fig.-6.12a shows the XRD pattern of the CNTs and the presence of characteristic peak of graphite (0 0 2) at 25.6^o (2Θ) is an indication of the carbon graphitization. For SnO_2 decorated FWCNTs (fig.-6.12b), the signature of CNTs are not well pronounced as the peak is masked by the intense peaks of metal oxide nanoparticles. From the XRD pattern, it is found that the SnO_2 crystallite structure belongs to the rutile phase and the average value of the crystallite size is estimated using the Scherrer formula to be 2.5 nm. To quantify the loading ratio of the SnO_2 to FWCNTs, TGA analysis was carried out at a heating ramp of 10^o C/min using ambient conditions. The result is shown in fig.-6.12c. A weight loss up to 99.8% is observed for the bare FWCNTs on heating and this takes place well above 500 ^{o}C. This signifies the purity of the FWCNT used for the decoration. The SnO_2 decorated FWCNTs showed a residual weight loss in two steps. The first step is mainly attributed to the release of chemically bonded water molecules, followed by the decomposition of FWCNTs. A total weight loss of about 60% indicates that the remaining fraction contains thermally stable SnO_2 nanoparticles in the composite.

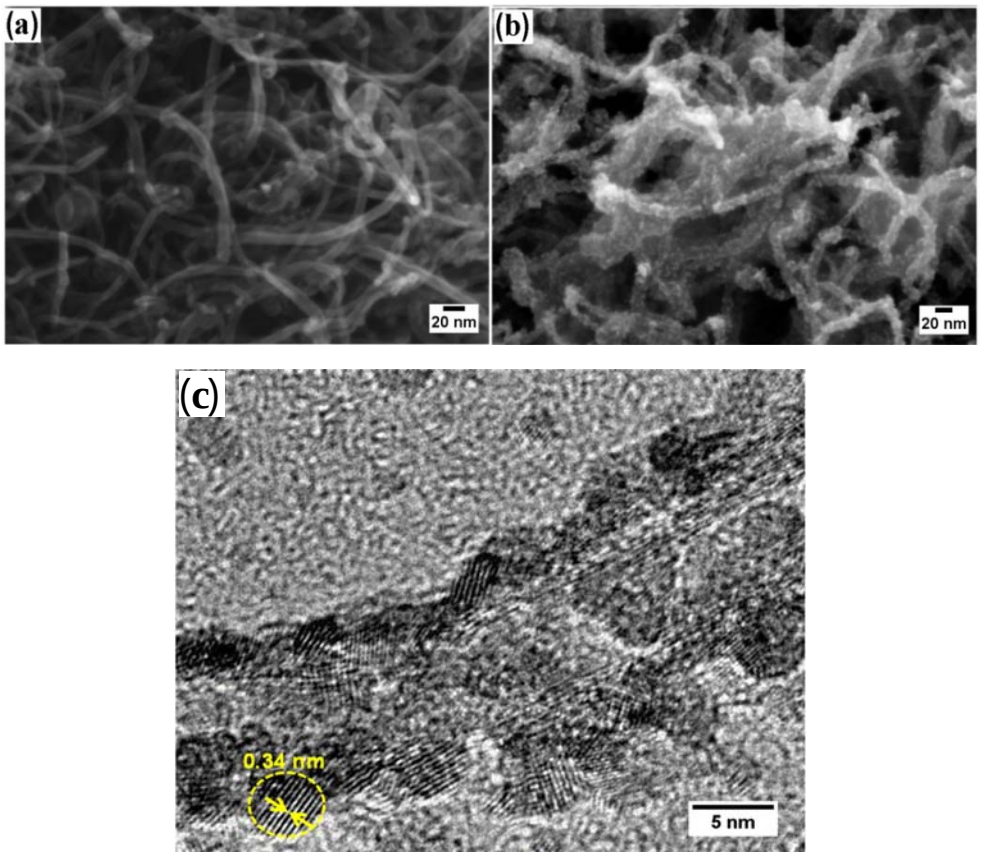

Figure 6.11: HRSEM micrograph of (a) FWCNTs, (b) SnO_2 decorated FWCNTs and (c) HRTEM micrograph of SnO_2 decorated FWCNTs. The spherical SnO_2 particle and its lattice spacing 0.34 nm are indicated in the figure.

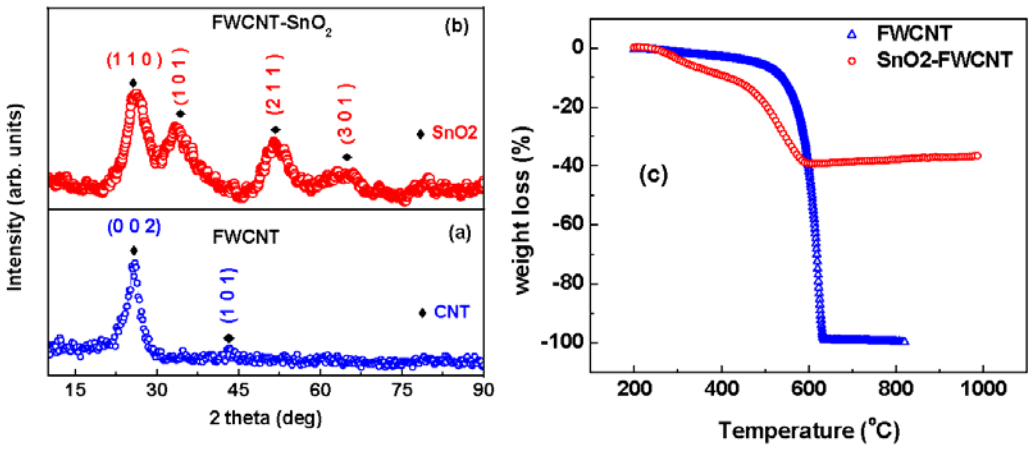

Figure 6.12: XRD of (a) FWCNTs, (b) SnO_2 decorated FWCNTs and (c) TGA of FWCNTs and SnO_2 decorated FWCNTs in ambient atmosphere.

6.3.2.2 Temperature dependant transport properties

A SnO_2-FWCNT random network sensor device was prepared as done for the FWCNTs. The device resistance is about 1.5 MΩ which is three orders magnitude higher than the pure FWCNTs. Temperature dependent transport behavior showed semiconducting behavior over the entire measured temperature regime 60-300 K (fig.-6.13). Due to very high device resistance (>10 MΩ) at low temperatures, the measurements could not proceed down to liquid He temperature. Fitting the experimental data between 60 and 300 K, showed that the network behaved like a highly disordered semiconductor with 3D-VRH mechanism. The equation for 3D VRH in terms of conduction is as follows [25],

$$\sigma(T) = \sigma_0 \exp\left[-\left(\frac{T_0}{T}\right)^{1/4}\right] \qquad (6.2)$$

Here, T_o is activation energy required for hopping. This 3D-VRH behavior of SnO_2 decorated FWCNTs reveals the absence of low dimensional anisotropic properties of FWCNTs from a Quasi 1D VRH mechanism. Hence, SnO_2 decoration on the FWCNTs changes the transport mechanisms in the network. Gas sensor properties of this device will be discussed in the next section.

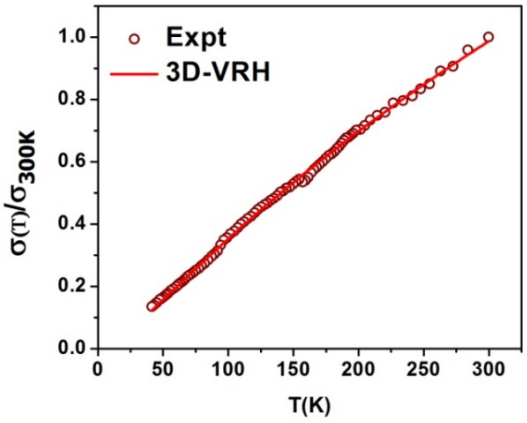

Figure 6.13: Temperature dependent conductance of the SnO_2-FWCNT networks. The straight line indicates the VRH fit to the observed data.

6.3.2.3 Gas sensor analysis

In this section, the gas sensor properties of the SnO_2 decorated FWCNTs are discussed. It is well known that oxides show high sensitivity at higher temperatures whereas CNTs show good sensitivity even at room temperature. The sensor properties are measured with respect to temperature, to establish the hybrid property of the SnO_2 decorated FWCNTs. Further to demonstrate the selectivity of the sensor, two different electron donor molecules were chosen as analyte. Observation of the gas sensing properties and their results are discussed below.

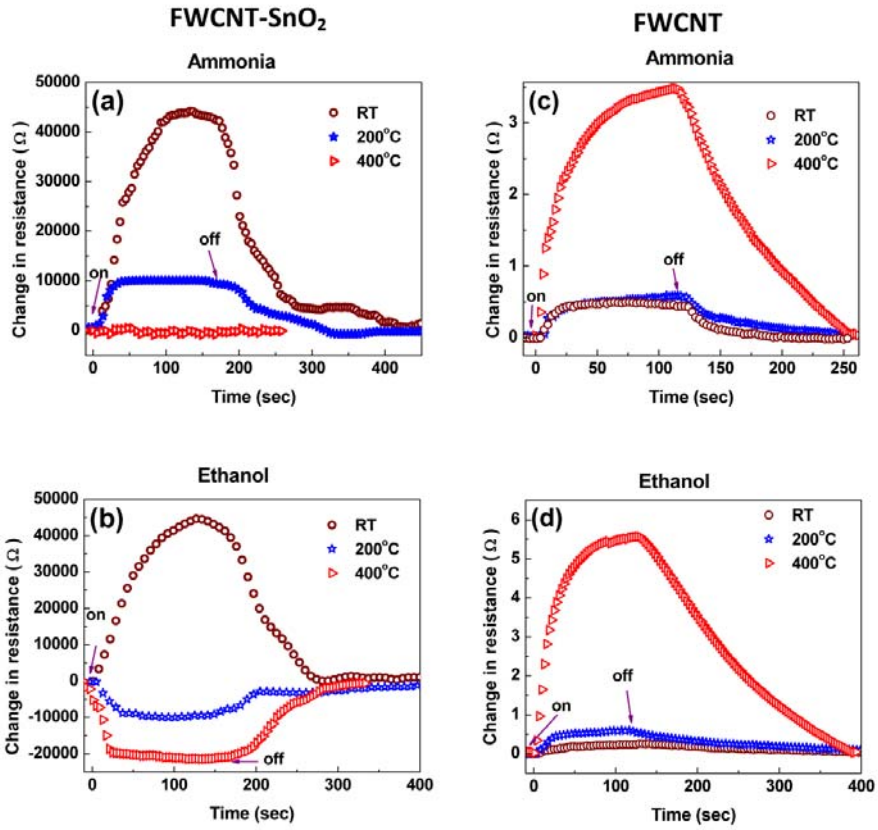

Figure 6.14: Sensing characteristics of SnO_2 decorated FWCNTs for (a) ammonia (b) ethanol and for pure FWCNTs with (c) ammonia and (d) ethanol respectively at RT, 200 and 400 ^oC

The resistance of the random network at RT, 200 ^{o}C and 400 ^{o}C are 1.5549, 0.9052 and 0.6873 MΩ respectively. The electrical conductivity in the present system can be visualized as the flow of current through the highly conducting FWCNTs modulated by the decorated semiconducting nanoparticles.

Figures 6.14a&b show the changes in resistance of the hybrid sensors for ammonia and ethanol at RT, 200 and 400 ^{o}C. For a typical dose of 500 ppm of ethanol or ammonia at RT, the change in resistance ($R-R_i$) is observed to be in the range of 34 kΩ in 1 min. The sensor response is expected to depend on the combined properties of n-type SnO_2 and p-type FWCNTs for the analyte gas. The pronounced effect of the SnO_2 as *n*-type semiconductor can be seen only at elevated temperatures as discussed earlier. Hence, at RT the hybrid material behaves as a *p*-type semiconductor due to the dominant role of FWCNTs. Since, ethanol and NH_3 both are electron donors; exposure of these gases to the FWCNTs will increase the resistance by virtue of their *p*-type nature. In the present case, both FWCNTs and SnO_2 have similar work functions and the Schottky barrier width between them is very small [24]. This enables easy electron transfer between FWCNTs and SnO_2 and the direction of transfer is determined by the prevailing analyte atmosphere. The direction of charge transfer is predominantly determined by SnO_2, when it becomes active at typical operating temperature of 200 ^{o}C and above.

At 200 ^{o}C the sensor exhibits a distinct behavior for the analyte gases. For 500 ppm of ethanol, the resistance decreases by 10.1 kΩ from the reference value whereas; it shows an increase in resistance of about 9.8 kΩ for ammonia. This indicates a remarkable difference in the sensing behavior of the sensor as *n*-type for ethanol and *p*-type for ammonia. However, the sensor exhibit *p*-type for both gases at RT. Such switching from *p*-type to *n*-type at elevated temperature distinctly exhibits

the dominant role of SnO_2. Similar ambipolar behavior has been also observed in large-diameter tubes due to charge transfer [12, 26]. In addition, the observed difference in sensitivity for ammonia and ethanol confirms the significant influence of SnO_2 at high temperatures. The enhancement in sensitivity is attributed to the nano grains of SnO_2 having size (4 nm) comparable to the thickness of the space charge layer (L_d) [21]. At 400 ^oC the resistance further decreases for ethanol and exhibiting a enhanced response (fig.-6.14b). In the case of ammonia, due to the enhanced activity of SnO_2 at elevated temperatures, the sensor shows a small variation in the resistance (fig-6.14a). This difference in electrical transport mechanism of the sensor material with respect to temperature can be effectively exploited for detection of ammonia and ethanol.

Further, to delineate the response of pure FWCNTs to analyte gases, experiments are performed under similar conditions (fig.-6.14c&d). The initial resistance of the random networks at RT, 200 and 400 ^oC are 1029, 759 and 517 Ω respectively. For both analyte, the pure FWCNTs are acting as a *p* type semiconductor with a small change in the resistance (~4 -6 ohms) between RT and 400 ^oC. Thus the response of pure FWCNTs in the gas detection is found to be poor when compared to FWCNTs-SnO_2.This clearly shows the FWCNT-SnO_2 hybrid material posses superior quality in the detection of gases.

To understand these results, a brief review on the nature of these constituent materials becomes necessary. It is well known that SnO_2 is a wide band gap semiconductor and act passive to analyte gases at RT. Inherent oxygen vacancy and interstitial tin in the SnO_2 make it to behave as an *n*-type semiconductor at elevated temperatures, i.e., above 200 ^oC. When SnO_2 is exposed to analyte, it adsorbs the gas molecules and catalytically decomposes it and injects electrons which in turn enhance

the conductivity. On the other hand, the conduction in the ideal CNT is ballistic at RT and exposure to gas atmospheres and acid purification makes it to behave like a *p*-type semiconductor due to oxidation of the surface [13]. Enhancement of electron concentration at elevated temperatures in SnO_2 reduces the hole current in the CNTs, which makes the Fermi level of the FWCNT shift near to the band center. Hence, any small charge transfer between SnO_2 and FWCNTs can make the Fermi level drift away from the charge neutrality point either towards conduction band (*n*-type) or to the valence band (*p*-type). Such charge transfer is dictated by the interaction of analyte with SnO_2 and the FWCNTs. At elevated temperatures ethanol decomposes in the presence of SnO_2 and injects electrons to enable the hybrid system to behave like an *n*-type semiconductor [27]. In the case of ammonia, no appreciable decomposition takes place and hence only a small change in the resistance is observed in both temperature regimes [28].

From the above discussion, the temperature dependent conduction behavior of discretely decorated SnO_2 gives the handle to construct a sensor capable of identifying both ammonia and ethanol. The observed results give conclusive evidence of the switching of the conduction mechanism between '*n*' and '*p*' type dictated by the nature of the analyte gases. The narrow band gap of the FWCNTs aids significant changes in the resistance values in combination with SnO_2, whose conductivity is influenced by the analyte gases. This helps in the identification of the different gases.

6.4 Field emission from CNTs

Field emission is the emission of electrons from the surface of a condensed phase into another phase due to the presence of high electric fields. CNTs are consider as a exceptional cathode material for electron emission due to this high aspect ratio,

this sharp tip to reduce the threshold voltage for extracting electrons, their high current carrying capacity and mechanical stability to avoid degradation of the material during long term usage. In view of this, CNT field emitters are expected to make a breakthrough in the development of field emission related applications. These include their use as a coherent source for electron microscopy, field emission display and ionization chamber.

6.4.1. CNTs in field emission based gas sensor

The field emission property of CNTs can be exploited to fabricate a selective gas sensor. This gas sensor is based on the fingerprinting ionization characteristics of the detected gases. The ionization of gas molecules takes place when it colloid with accelerated electrons. In this process, there is no adsorption and chemical interaction between the sensor material and the molecules. Therefore, as found in chemiresistors the process is not limited to identify gases with low adsorption energy and poor charge transfer. Hence, sensing of inert gases or gas mixtures can easily be achieved in an ionization chamber. However, the issues related to conventional ionization gas sensors are their bulky architectures, considerable high power consumption, and breakdown voltage, which is inefficient and risky in operation. CNTs, due to their extremely sharp tip structure, can induce a large field enhancement factor and thereby increase the electric field around the tips to initiate corona discharge at a very low voltage. Therefore, the effect of gas adsorption on the field emission properties of CNT enhanced ionization gas sensors has attracted a great amount of research interest [1, 10]. Hence, it is very important to study the field emission properties of CNTs for use in ionization based gas sensors. Moreover the field emission properties of CNTs depend on their diameter, morphology and density. In this work, two different morphological featured CNTs (straight & helical) were grown by Fe and modified Fe

with Mo catalysts and also their field emission properties are studied. The details of the synthesis methods were given in chapter-3.

The family of CNTs shows a variety of shapes such as curved, planar- spiral, and helical simply because of the existence of hexagon, pentagon, and heptagon carbon rings as a result of its unique hybridization sp^1, sp^2, and sp^3 bonding possibilities of carbon. A combination of these three types of configurations can make any desired geometrical shape. Helical CNT was predicted in the 1993 by Itho et al., [29] and were first experimentally observed by Zhang et al., [30] in 1994. The CVD technique is used to produce straight CNTs. However, in order to synthesize helical CNTs, the active catalyst requires modification to cause anisotropic carbon extrusion, inducing helical growth of carbon from the catalyst surface [31-33]. The helical CNTs have excellent field emission properties compared to straight CNTs. The intrinsic availability of the non sp^2 structure on the helical CNT walls also participates in the field emission. The screening effect during the field emission was reduced due to isolation of the tubes by the helical morphology of the nanotubes [34-35].

6.4.2. Structural characterization of the grown CNT mats

The cross sectional SEM micrographs of the as-grown CNT samples are shown in fig.-6.15. CNTs grown on a Fe catalyst has straight morphology with few microns lengths. Due to the low number density and the few microns in length, the grown carbon nanotubes are bent and randomly arranged on the substrate. CNTs grown on Fe/Mo catalysts have lengths of tens of microns and are more crowded and helical in nature with different pitch.

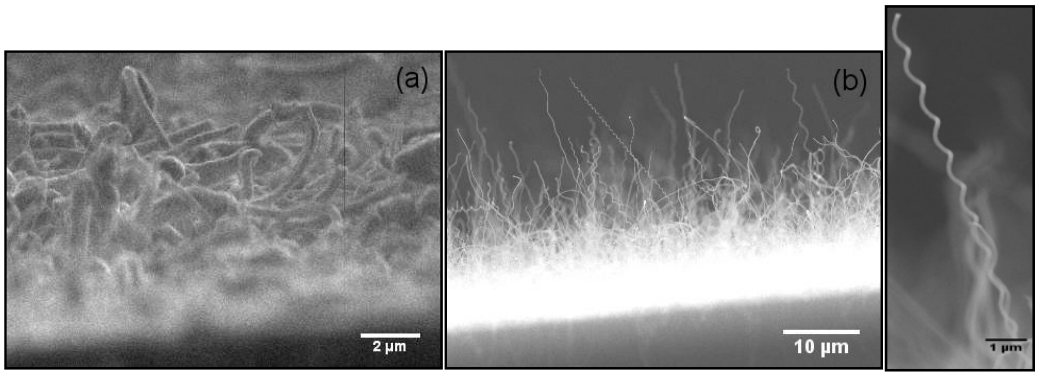

Figure 6.15: Cross section SEM micrographs of the as grown CNTs on (a) Fe, (b) Fe/Mo catalyst and (c) the magnified spot of a helical CNT.

The Raman spectra of the two samples are shown in fig.-6.16a&b. The characteristic peaks of first order D, G and D' bands appear at 1349 cm^{-1}, 1577 cm^{-1}, 1612 cm^{-1} and 1348 cm^{-1}, 1575 cm^{-1} 1608 cm^{-1} for the Fe and Fe/Mo catalyst grown CNTs respectively. The I_D/I_G ratios of straight and helical CNTs are 0.33 and 0.44 respectively which reveals that the defect level is higher in the helical CNTs. The increase in the defect concentration is due to the presence of non sp^2 carbon in the helical CNTs [36-37].

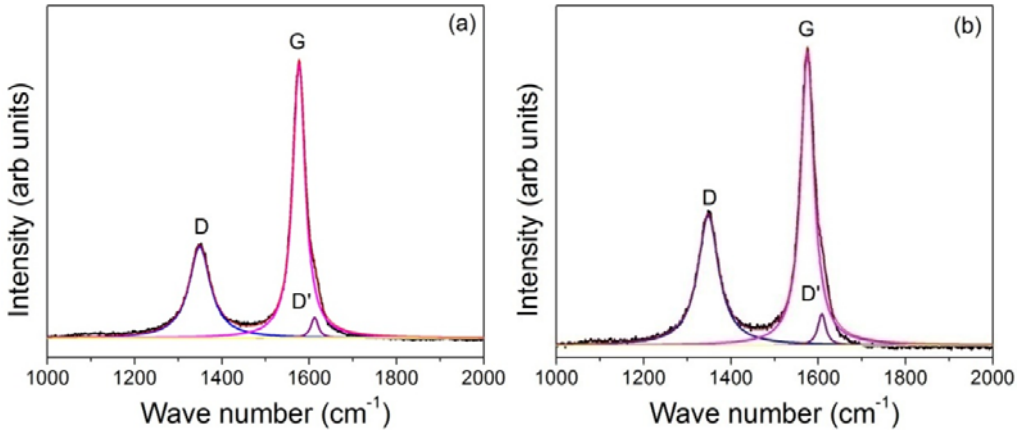

Figure 6.16: Raman spectra of the CNTs grown on (a) Fe and (b) Fe/Mo catalysts.

It is well known that the growth and structure of the CNTs depends on several factors including the homogeneity of the catalytic activity of the particle, the supply of the carbon source and the distribution of carbon atoms in the catalytic particle. If any of these factors are changed, then the growth condition is altered and irregular CNTs will form. Hence, in this present work, all the experimental conditions were maintained identical and only the catalyst was varied.

To understand the effect of the catalyst morphology, the catalyst films were loaded in quartz reactor and the experimental sequences were followed up to ammonia treatment. The topography of the catalyst before and after ammonia treatment was determined by AFM.

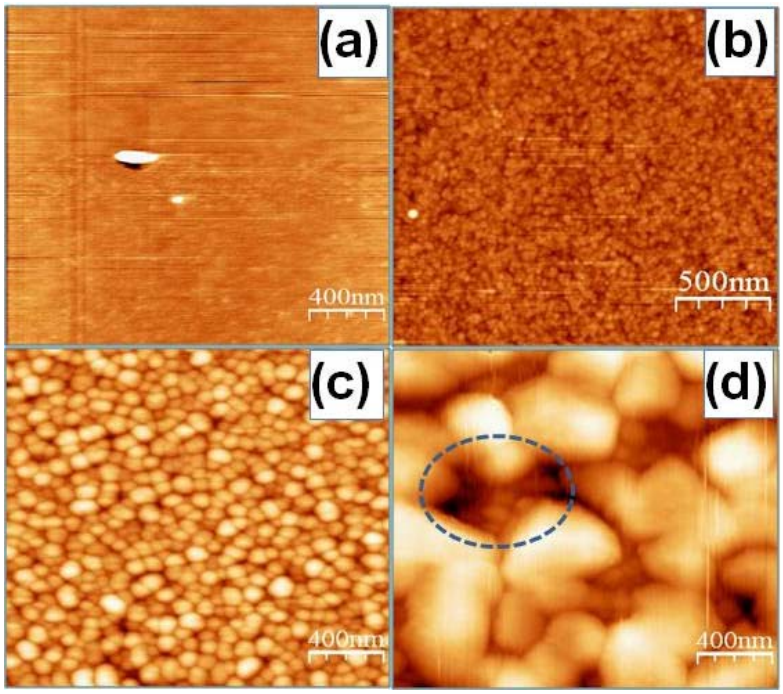

Figure 6.17: (a) & (b) AFM topography of the as coated Fe and Fe/Mo catalyst on Si/SiO_2 (c) & (d) After ammonia treatment at 700^{o}C. The area inside the circle shows the nanoparticles in the bottom layer.

Fig.-6.17-a&b shows the topography of the as coated Fe and Fe/Mo films respectively. Fig.-6.17-c&d shows the film morphology after ammonia treatment. After the ammonia treatment, the smooth Fe film has collapsed and formed a uniform distribution of larger sized particles. In the Fe/Mo film, two layers of particle distribution are seen. Here, the morphology of the bottom layer is similar to a Fe particle and the top layer consists of bigger particles. Although the detailed growth mechanism for the helical carbon nanotubes formation is not fully understood, these catalyst morphologies suggest that the non catalytic Mo clusters modify the catalytic activity of Fe catalyst and supply the feed carbon in a highly inhomogeneous way. Such an inhomogeneous carbon supply can lead to the formation of helical or other non-sp^2 bond carbon nanostructures.

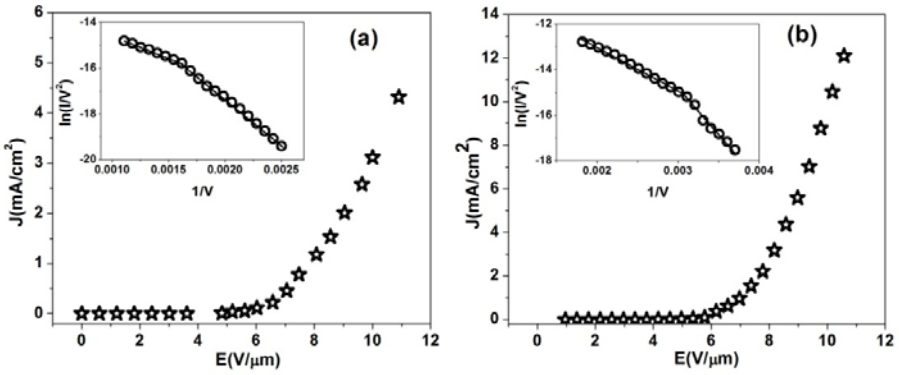

Figure 6.19: The current density vs. electric field curves for CNTs grown on (a) Fe and (b) Fe/Mo catalysts. The insets show the corresponding F-N plots

6.4.3 Field emission measurements

In order to study the field emission properties of the CNTs, they were placed in a vacuum chamber with a base pressure of $5x10^{-7}$ mbar. Fig.-6.19a&b shows the variation of current density (J) versus electric field (E) for Fe-CNT and Fe/Mo-CNTs respectively. As can be seen from the plots, the Fe/Mo-CNTs sample shows similar

threshold voltage and higher current density compared to the Fe-CNTs sample. This is due to the variation in morphology, length and diameter of the CNTs [38]. The CNTs grown on Fe/Mo has the helical morphology which has the electron emission sites not only on the tips but also on the walls of the tubes. These field emission characteristics were analyzed using the Fowler–Nordheim (F-N) tunneling mechanism. The F-N tunneling can be expressed as [39]

$$I = S * a\frac{{E_s}^2}{\phi} * exp\left\{-b\frac{\phi^{3/2}}{E_s}\right\} \qquad (6.3)$$

where, S (cm) is the emitting surface, E_s (V/cm) is the electric field at the nanotube apex, ϕ is the work function, a = 1.54×10^{-6} A V^{-2} eV and b = 6.83×10^{7} V cm $eV^{-2/3}$ respectively. The electric field at the nanotube tip E_s is related to the applied voltage V via $E_s = \beta V/d$, where, β is the field enhancement factor at the sharp tip of the nanotube and d (μm) is the CNT tip-anode separation. According to the F-N model, a plot of $\ln(I/V^2)$ vs. 1/V has a linear behavior. But in the present study the analysis showed two slopes in the low and high fields as depicted in inset of the fig.-6.19 a & b.

In recent years the appearances of two slopes have been investigated by many researchers [40-42]. The observation of two slopes in a F-N plot over the electric field range 0-12V/μm is due to the presence of two barriers of 'SiO_2 substrate – CNT – vacuum' structure in between electrodes. Two different mechanisms are involved in the tunneling of an electron from the substrate – CNTs barrier and CNT – vacuum barrier. These mechanisms are also dependent on the applied voltage. While the mechanism that operates at the CNT-vacuum barrier is F-N tunneling, it can be a combination of direct tunneling and F-N tunneling at the substrate-CNT barrier

depending on the voltage. At low field the electron emission is influenced by the presence of the oxide potential barrier, so that the field enhancement factor is evaluated at higher field using the formula[43],

$$\beta = -B\left[\frac{\phi^{3}/_{2}}{S_{F-N}}\right]d \qquad (6.4)$$

where, B = 6.83 x 10^7 $eV^{-3/2}$ V cm^{-1}, ϕ is the work function of CNTs (5 eV), d is the emitting distance and $S_{F\text{-}N}$ the slope of the F-N plot. The calculated values of the field enhancement factor for the Fe-CNTs and Fe/Mo-CNTs are 603 and 1541. Thus the helical CNTs give a field enhancement factor more than two times that of the straight CNTs.

From the above discussion, one can understand that carbon morphology plays a crucial role in deciding field emission properties. The observed results also confirm that the helical CNTs grown on Fe/Mo-catalysts are better field emitters than the straight CNTs grown on Fe catalysts.

6.5 Summary

Gas sensing properties of FWCNT random networks were studied. It was shown that FWCNTs are sensitive to various gases and it behaves like a 'p' type semiconductor. The sensitivity of the FWCNTs for the electron acceptor gas NO_2 and electron donor gases such as NH_3, N_2O, CH_4 and H_2 were studied. From the experimental results it was found that the sensitivity of NH_3 is the highest and H_2 as the lowest, as given in order NH_3, N_2O, CH_4 and H_2. It is also shown that a FWCNT device is sensitive for ppm levels of NH_3 gas.

Further to enhance the sensitivity and selectivity of the FWCNTs, Pd and SnO_2 nanoparticles were decorated on to the FWCNTs. By comparing the FWCNTs

with the hybrid Pd-FWCNTs network a higher conductivity and multifold enhanced sensitivity for H_2 was observed for the Pd-FWCNTs. The temperature dependent transport mechanisms in Pd-FWCNT networks were studied and found to show that the presence of a combined conduction mechanism of FIT and VRH similar to bare FWCNTs. Further, these mechanisms have potential to activate more charge carriers to modify the sensitivity of the sensor devices with a higher applied voltage. The phenomenon is substantiated by the nonlinear behavior of the I-V curve and enhanced sensitivity of FWCNTs and Pd-FWCNTs for NH_3 and H_2, respectively.

A temperature dependent sensing behavior of discretely decorated SnO_2 on FWCNTs gives a method to construct a sensor capable of identifying both ammonia and ethanol. The narrow band gap of FWCNTs aids the significant changes in the resistance values in combination with SnO_2, whose conductivity is influenced by the analyte gases. Switching of the conduction mechanism between 'n' and 'p' type is dictated by the nature of the analyte gases. This helps in the identification of the different gases.

Field emission studies were carried out on straight and helical CNT mats. The helical CNTs grown on Fe/Mo catalysts give better field emission than the Fe grown CNTs. Such high field emitting CNTs can be effectively employed as ionization gas sensors.

6.5 References

[1] Y. Wang and J. T. W. Yeow, "A Review of Carbon Nanotubes-Based Gas Sensors," *Journal of Sensors,* vol. 2009, p. 1, 2009.

[2] T. Zhang*, et al.*, "Recent progress in carbon nanotube-based gas sensors," *Nanotechnology,* vol. 19, p. 332001, 2008.

[3] O. K. Varghese*, et al.*, "Gas sensing characteristics of multi-wall carbon nanotubes," *Sensors and Actuators B: Chemical,* vol. 81, p. 32, 2001.

[4] J. Zhao*, et al.*, "Gas molecule adsorption in carbon nanotubes and nanotube bundles," *Nanotechnology,* vol. 13, p. 195, 2002.

[5] H. Xiao*, et al.*, "First-principles study of Pd-decorated carbon nanotube for hydrogen storage," *Chemical Physics Letters,* vol. 483, p. 111, 2009.

[6] D. W. H. Fam*, et al.*, "Selective sensing of hydrogen sulphide using silver nanoparticle decorated carbon nanotubes," *Sensors and Actuators B: Chemical,* vol. 138, p. 189, 2009.

[7] A. Ruiz*, et al.*, "Surface activation by Pt-nanoclusters on titania for gas sensing applications," *Materials Science and Engineering: C,* vol. 19, p. 105, 2002.

[8] W. D. Zhang and W. H. Zhang, "Carbon nanotubes as active components for gas sensors," *Journal of Sensors,* vol. 2009, p. 1, 2009.

[9] E. Comini, "Metal oxide nano-crystals for gas sensing," *Analytica Chimica Acta,* vol. 568, p. 28, 2006.

[10] A. Modi*, et al.*, "Miniaturized gas ionization sensors using carbon nanotubes," *Nature,* vol. 424, p. 171, 2003.

[11] J. Li, *et al.*, "Carbon nanotube sensors for gas and vapor detection," *Nano Lett.,* vol. 3, p. 929, 2003.

[12] M. Penza, *et al.*, "Functional characterization of carbon nanotube networked films functionalized with tuned loading of Au nanoclusters for gas sensing applications," *Sensors and Actuators B: Chemical,* vol. 140, p. 176, 2009.

[13] J. Kong, *et al.*, "Nanotube molecular wires as chemical sensors," *Science,* vol. 287, p. 622, 2000.

[14] M. Penza, *et al.*, "Enhancement of sensitivity in gas chemiresistors based on carbon nanotube surface functionalized with noble metal (Au, Pt) nanoclusters," *Applied physics letters,* vol. 90, p. 173123, 2007.

[15] A. Kaiser, *et al.*, "Comparison of current-voltage characteristics of nanofibres and nanotubes," *AIP Conference Proceedings,* vol. 723, p. 99, 2004.

[16] D. Wang, *et al.*, "Hopping conduction in disordered carbon nanotubes," *Solid state communications,* vol. 142, p. 287, 2007.

[17] G. T. Kim, *et al.*, "Non-ohmic current–voltage characteristics in single-wall carbon nanotube network," *Synthetic Metals,* vol. 117, p. 123, 2001.

[18] T. Hübert, *et al.*, "Hydrogen sensors – A review," *Sensors and Actuators B: Chemical,* vol. 157, p. 329, 2011.

[19] R. Ghasempour, *et al.*, "Hydrogen sensing properties of multi-walled carbon nanotube films sputtered by Pd," *International Journal of Hydrogen Energy,* vol. 35, p. 4445, 2010.

[20] M. Batzill and U. Diebold, "The surface and materials science of tin oxide," *Progress in Surface Science,* vol. 79, p. 47, 2005.

[21] Y. Chen, *et al.*, "The enhanced ethanol sensing properties of multi-walled carbon nanotubes/SnO_2 core/shell nanostructures," *Nanotechnology* vol. 17, p. 3012, 2006.

[22] C. Wongchoosuk, *et al.*, "Portable electronic nose based on carbon nanotube-SnO_2 gas sensors and its application for detection of methanol contamination in whiskeys," *Sensors and Actuators B: Chemical,* vol. 147, p. 392, 2010.

[23] N. Van Hieu, *et al.*, "Highly sensitive thin film NH_3 gas sensor operating at room temperature based on SnO_2/MWCNTs composite," *Sensors and Actuators B: Chemical,* vol. 129, p. 888, 2008.

[24] G. Lu, *et al.*, "Room-Temperature Gas Sensing Based on Electron Transfer between Discrete Tin Oxide Nanocrystals and Multiwalled Carbon Nanotubes," *Advanced Materials,* vol. 21, p. 2487, 2009.

[25] B. I. Schlovskii and A. L. Efros, *Electronics Properties of Doped Semiconductors* Berlin: Springer-Verlag, 1984.

[26] P. Chiu, *et al.*, "Temperature dependence of conductance character in nanotube peapods," *Applied Physics A: Materials Science & Processing,* vol. 76, p. 463, 2003.

[27] T. Jinkawa, *et al.*, "Relationship between ethanol gas sensitivity and surface catalytic property of tin oxide sensors modified with acidic or basic oxides," *Journal of Molecular Catalysis A: Chemical,* vol. 155, pp. 193-200, 2000.

[28] S. F. Yin, *et al.*, "A mini-review on ammonia decomposition catalysts for on-site generation of hydrogen for fuel cell applications," *Applied Catalysis A: General,* vol. 277, p. 1, 2004.

[29] S. Itoh, *et al.*, "Toroidal form of carbon C_{360}," *Physical Review B,* vol. 47, p. 1703, 1993.

[30] X. Zhang, *et al.*, "The texture of catalytically grown coil-shaped carbon nanotubules," *Europhysics Letters,* vol. 27, p. 141, 1994.

[31] S. Motojima, *et al.*, "Preparation of coiled carbon fibers by catalytic pyrolysis of acetylene, and its morphology and extension characteristics," *Carbon,* vol. 29, p. 379, 1991.

[32] Y. Wen and Z. Shen, "Synthesis of regular coiled carbon nanotubes by Ni-catalyzed pyrolysis of acetylene and a growth mechanism analysis," *Carbon,* vol. 39, p. 2369, 2001.

[33] J. Xie, *et al.*, "Catalytic chemical vapor deposition synthesis and electron microscopy observation of coiled carbon nanotubes," *Smart materials and structures,* vol. 12, p. 744, 2003.

[34] L. Pan, *et al.*, "Field emission properties of carbon tubule nanocoils," *Japanese Journal of Applied Physics,* vol. 40, p. 235, 2001.

[35] L. Pan, *et al.*, "Effect of morphology on field emission properties of carbon nanocoils and carbon nanotubes," *Japanese journal of applied physics,* vol. 44, p. 1652, 2005.

[36] H. Hou, *et al.*, "Large-scale synthesis and characterization of helically coiled carbon nanotubes by use of Fe (CO) 5 as floating catalyst precursor," *Chemistry of materials,* vol. 15, p. 3170, 2003.

[37] J. N. Wang, *et al.*, "Growth of highly compressed and regular coiled carbon nanotubes by a spray-pyrolysis method," *Crystal Growth and Design,* vol. 8, p. 1741, 2008.

[38] Y. Cheng and O. Zhou, "Electron field emission from carbon nanotubes," *Comptes Rendus Physique,* vol. 4, p. 1021, 2003.

[39] J. Gadzuk and E. Plummer, "Field emission energy distribution (FEED)," *Reviews of Modern Physics,* vol. 45, p. 487, 1973.

[40] J. Zhang, *et al.*, "Appearance of a knee on the Fowler–Nordheim plot of carbon nanotubes on a substrate," *Solid State Communications,* vol. 138, p. 13, 2006.

[41] R. Angelucci, *et al.*, "Honeycomb arrays of carbon nanotubes in alumina templates for field emission based devices and electron sources," *Physica E: Low-dimensional Systems and Nanostructures,* vol. 42, p. 1469, 2010.

[42] L. Chen, *et al.*, "Nonlinear characteristics of the Fowler–Nordheim plots of carbon nanotube field emission," *Physica Scripta,* vol. 82, p. 035602, 2010.

[43] R. Lv, *et al.*, "Enhanced field emission of open-ended, thin-walled carbon nanotubes filled with ferromagnetic nanowires," *Carbon,* vol. 47, p. 2709, 2009.

Chapter-7 Conclusion and Future perspective

7.1 Conclusion

CNT based research have come a long way since its celebrated discovery by Iijima in 1991. Subsequent to this event, with the advent of sweeping technological innovations in electron microscopy and atomic force microscopy, various aspects of CNTs have been studied extensively and reported in literature by various research groups across the world. Applications based on CNTs have been demonstrated in the field of sensors, solar cells, thin film transistors and medicine. However, still it is too far for this material to reach in the hands of common man as a utility material in our day to day life. In this context the study of this material comes into prominence when issues pertaining to mass production, characterization and implementation in technological applications.

This thesis attempts to address some of the important issues related to synthesis of FWCNTs, purification, characterization and applications thereof. Among many methods to synthesis CNTs, CVD is found to be the most appropriate and popular method reported in literature to make CNTs. However, the nature of the product formed in this process is significantly influenced by many parameters. Proper combinations of catalyst, catalyst support material, carbon source and thermal conditions are some of the necessary parameters that require careful optimization. Deviation of process parameters from optimized values may seriously affect the CNT yield, tube diameter and its crystalline purity. Among these parameters, catalyst and catalyst support material plays an important role in determining the distribution of the tube diameter and number of tube walls. In view of these aspects, the method used in

this thesis was based on methane as carbon source with MgO and Zeolite-13X as catalytic support material and Fe & Mo as catalyst for inducing carbon cracking.

The systematic observations on the *in-situ* growth process of CNTs in a home-made TGA-MS set up has revealed a few interesting results. While a significant CNT yield is obtained using MgO, surprisingly, the growth process over zeolite was found to be impeded. Analysis of the DTA thermal curves and XRD spectra clearly attributed reasons to the inferior thermal stability of the zeolite-13X and its structural collapse through crystalline transformations. Hence, in spite of the abundant availability of carbon by thermal cracking, zeolite loses its porous nature at high temperatures and thereby hinders CNT growth. Even in a low temperature regime, a deposit of carboneous materials on the surface poisons the catalyst and consequently inhibits carbon cracking. On the other hand, MgO showed excellent structural stability throughout the process thermal window and thereby increased carbon production both by catalytic and thermal cracking. As a result the copious amount of carbon aids in the enhanced yield. Thus *in-situ* monitoring of the growth process by TGA-MS brings in new understanding and answers the question as to why zeolite-13X, a popularly known template has proven to be a poor support when methane is used as carbon source. Though, this problem was later circumvented by altering the pH value of the zeolite-13X, the growth process needs to be restricted to temperature below which the zeolite is stable and its structure is intact. CNT growth in zeolite within this thermal window solely depends on the carbon supplied by the catalytic cracking and hence gives a low yield when compared to MgO.

Having ensured the optimal conditions for a good yield in the CNT synthesis, a Fe-Mo catalyst combination was used to bring down the distribution in tube diameter that eventually lead to the formation of FWCNTs. The sustained catalytic

property of Fe-Mo combinations in FWCNTs growth has been analyzed through in situ TGA-MS analysis. It is found that the growth rate was sustained by ensuring Fe catalyst availability throughout the growth process by the addition of Mo. This observation shows that the addition of Mo to a Fe catalyst enhances the yield as well as gives a method to tune the diameter of FWCNTs. The use of other bimetallic catalysts such as Co-Mo and Co-Ni only produced CNTs with a bamboo structure. From the above studies, it is well established that apart from the porous nature of the catalyst support, considerations of pH value of a catalyst is also an important factor. Tuning the pH value during impregnation of a catalyst in the support material introduces Lewis base sites and found to be a crucial parameter in deciding the formation of aromatic rings of carbon by polymerization. In essence, this thesis elucidates, TGA-MS set up can be effectively used to address a variety of issues pertaining to the CNT growth process. The temperature profiles along with the weight loss/gain and the gas species evolved during the growth process provides a wealth of information to understand the growth kinetics.

Generally the CVD process not only yields nanotubes, but also a variety of carbonaceous impurities. The physical properties of CNT's invariably rely on the purity of the CNT. Hence, it is extremely important to investigate the purification methods to isolate CNTs of choice by rejecting unwanted impurities. Because of their large aspect ratio, CNTs are subject to large van der Waals forces, which cause them to stick together, forming large bundles. Therefore, one of the major challenges in fabricating a CNT film is to separate the tubes, without using covalent chemistry or other harsh conditions, which could lower their electrical conductivity. In this thesis a soft chemistry approach was used for this purpose and purified samples (FWCNTs) were evaluated for their purity by TGA and Raman spectroscopy. Raman

spectroscopy provides information on G, D, D' and G' bands that helps to identify the nature of impurities. A number of mild acid solutions in combination with sonication were employed to achieve high purity. While sonication is important as a means to separate the tubes, a prolonged sonication can damage the tube wall. Hence, an optimal condition is arrived through a trial and error method and purity as high as 99.5% was achieved with minimum structural defects (I_D/I_G ~ 0.1). Raman spectra recorded on these samples using lasers with different excitation energies revealed the intrinsic structural and electronic properties of the FWCNTs. Herein, it is important to note that although mild acid treatment and subsequent use of H_2O_2 is widely reported in the literature, the underlying mechanism is usually not discussed in detail. An investigation of this multi-step purification process using Raman spectroscopy helps in understanding this microscopic phenomenon. An initial acid reflux with HNO_3 and occasional sonication eliminated metal and catalytic oxide support impurities. Consequently, CNTs with purity as high as 98-99% have been achieved. The subsequent treatment with H_2O_2 helped in removing the fullerene caps, oxidization of the other carbonaceous materials and intercalations. Further, the structural integrity was ascertained by weight loss measurements in a TGA where the sample was allowed to decompose over a temperature range up to 600 ^oC in air. Impurities like amorphous carbon (300 ^oC) and damaged CNTs (450 ^oC) were thermally decomposed leaving pure CNTs with superior structural integrity. Evidence of these facts from TGA curves ensured the purity of the samples obtained after H_2O_2 treatment in the multistep process.

From a applications perspective, there is tremendous interest in the development of sensors using nanotubes, especially in chemical and biological sensing applications. The major advantages of nanotube based sensors lie in their size

compatibility, high sensitivity and use of electronic sensing that eases the signal processing. However, to exploit this potential, high purity CNTs with structural integrity is essential. Herein, it is important to note that the CVD process inherently introduces defects into the tube walls. This provides motivation for the study of the role of defects in determining the electrical and functionalization properties of CNTs that may result change in their physical properties. This thesis makes a detailed investigation of the role of structural defects in the electrical transport mechanism. A temperature dependent transport measurement was carried out using a spin coated CNT network on interdigtated electrodes. The ensuing results were analyzed using a VRH and FIT mechanism. The analysis showed that the conductivity mechanism cannot be explained with a unique mechanism, but with a combination of these two. The dominant contribution of the VRH and FIT is shown to be structure dependent. A detailed knowledge on this subject is required to technological applications.

The exotic features of CNTs have attracted innovative applications in the field of gas sensors as CNTs are sensitive to a wide range of gas molecules. This may appear as a great advantage in the first place but nevertheless also restrict its usability. Hence, functionalization of CNTs with different nanoparticles/molecules becomes an important aspect to achieve the desired physical properties. This thesis demonstrates FWCNT based hybrid material for use as gas sensors with high selectivity and sensitivity using nanoparticles of Pd and SnO_2. While the former was used for detecting H_2 at room temperature, the later is used in the detection of ethanol and ammonia at elevated temperatures. Both sensors show enhanced sensitivity when compared to bare CNTs.

The sensor for these sensing applications is devised as a simple two-terminal resistor with the hybrid surface exposed to the gaseous environment. The resistance

signal was monitored in real time to probe the dynamics of the sensing process. In a CNT, charge transfer occurs due to adsorption of gas molecule and therefore the threshold voltage is found to shift due to electron withdrawal (positive voltage shift) or electron donation (negative voltage shift). The adsorption of sensing species causes an overall drop in conductance due to scattering of the charge carrier. The randomly oriented CNT network can statistically average out the variations in individual CNTs, leading to device performance with excellent reproducibility, and adequate sensitivity. As mentioned earlier the nature of the charge transfer makes changes in the resistance either by increasing or decreasing from an initial reference value obtained at an operating temperature. Hence selectivity among molecules of similar charge transfer capabilities and adsorption kinetics are challenging. Further, aging and agglomeration due to high operating temperature of the metal oxide lead to degradation in performance and life time. The temperature dependent response of a sensor based on FWCNT-SnO_2 is shown as an illustrative application for selective gas sensing. This can be considered as a significant step in CNT based gas sensor applications.

7.2 Scope for future work

While the present work has made investigations on the three stages of CNTs viz., synthesis, characterization and application and contributed to the existing understanding, there exist many riddles yet to be solved.

- Large scale applications based on CNTs rely on synthesis methods that can yield CNTs of a specific choice in abundance and with high purity. The existing methods yield a mixture of CNTs of a varying nature. While purification methods are available to separate them, it is yet to be established whether these methods can be scaled up for industrial applications.

- The *in-situ* growth of CNTs in a TGA-MS set up can be extended to study the kinetics involved in CNT growth. This will give direct evidence on the temperature dependent catalytic activity and yield in the entire growth process.
- CNT growth on different substrates needs to be investigated by properly tuning their acid-base nature. This study can give further understanding of the growth mechanism and knowhow of CNT growth on any substrate.
- Till now FET based devices use only SWCNTs for sensor application. This can be taken to the next stage by replacing SWCNTs with metal oxide decorated CNTs. This can provide a detailed understanding and pave the way to tailor the band gap of CNTs by decoration with nanoparticles. These experiments require the dispersion of decorated CNTs and making contacts with lithography techniques.
- A random network of CNTs needs to be studied in detail both theoretically and experimentally. A temperature dependent Hall effect, thermopower and Magneto-Resistance can effectively address the issues of charge transport and n to p type switching behavior of hybrid CNTs.
- Di-electrophoresis can be a potential technique to disperse CNTs between electrodes for these studies. By optimizing parameters like voltage, frequency and time one can fine tune the density and alignment of CNTs between electrodes. Further this technique can be used to selectively decompose metallic tubes by passage of a high current to enrich the abundance of semiconducting tubes.

Though some of the above suggestion seems to be very ambitious, the evolution of research on CNTs has proved that there are always twists and turns and of course, a lot of surprises too!

Publications

Peer reviewed Journals

1. **R. Kamalakannan**, K. Ganesan, S. Ilango, N. Thirumurugan, V. N. Singh, M. Kamruddin, B. R. Mehta, and A. K. Tyagi. The role of structural defects on the transport properties of a few-walled carbon nanotube networks, Appl. Phys. Lett. **98**, 192105 (2011).
2. **R. Kamalakannan**, K. Ganesan, M. Kamruddin, and A. K. Tyagi. Temperature Dependent Transport Properties of a Few-walled Carbon Nanotubes Network, AIP Conf. Proc. **1313**, 215 (2010).
3. **R. Kamalakannan**, S. Ilango, M.Kamruddin and A.K. Tyagi. The Effect of Catalyst on Synthesis of Carbon Nanotubes: An In Situ TGA Study, AIP Conf. Proc. **1447**, 303 (2012).
4. **R. Kamalakannan**, S. Karthika, M. Kamruddin and A. K. Tyagi. Pd decorated few walled carbon nanotube networks for room temperature hydrogen sensor applications, IEEE Conf Proc. **559**, (2011).
5. **R. Kamala kannan**, P. Jeyaraman, P.K. Ajikumar, S. Ilango, M. Kamruddin and A.K. Tyagi. Effect of catalyst supports in the synthesis of carbon nanotube using methane by chemical vapor deposition (communicated).
6. **R. Kamalakannan**, S. Ilango, S. Amirthapandian, M. Kamruddin and A. K. Tyagi. Incorporation of selectivity in Discrete SnO_2 decorated few walled CNTs for gas sensing applications (communicated).
7. **R. Kamala Kannan**, George Joseph, P. Shankar, R.V. Subba Rao, A.K. Tyagi, P.R. Vasudeva Rao. Neutron absorber coatings for criticality control in annular tanks employed in spent fuel reprocessing, Annals of Nuclear Energy **36**, 1211 (2009).

8. **R. Kamalakannan et al.,** Raman spectroscopy on evaluation of FWCNTs during purification (Under preparation)**.**

Conferences

1. **R. Kamalakannan**, Kalpataru Panda, B.Sundaravel, V.Thomas Paul, M.Kamruddin, A.K.Tyagi. Synthesis of helical carbon nanotubes and their field emission characteristics, International Conference on Carbon Nanotechnology-2010, IITK, India.
2. **R. Kamalakannan**, K. Aruna, S. Ilango, M.Kamruddin, and A.K.Tyagi. A novel method of cap removal to enhance structural perfection in few walled carbon nanotubes, International Conference on Electron Nanoscopy-2011, Hyderabad, India.
3. **R. Kamalakannan**, M. Kamruddin and A.K. Tyagi. Synthesis of Metal Filled Carbon nanotube towards sensor applications, Nano Sensors 2008- National workshop on Nano Sensors & Devices, IIT Delhi, India.
4. **R. Kamalakannan**, P. Jeyaraman, Priyadharsini, P. K. Ajikumar, Chittaranjan Das, M. Kamruddin and A. K. Tyagi. Effect of zeolite and MgO template for CNT growth using CH_4 feed stock by TCVD, India-Brazil-South Africa (IBSA) Nanotechnology School on Advanced Materials-2010, Kalpakkam, India.
5. **R. Kamala kannan**, M. Kamruddin and A. K. Tyagi. Effect of support and catalyst on CNT growth using CH_4 feed stock by TCVD, ICONSAT-2010, IITB, India.
6. M. Kamruddin, Sathya Priya, **R Kamalakannan**, P K Ajikumar and A K Tyagi. Effect of synthesis method and conditions on ZnO nanostructures, ICONSAT-2010,IITB, India.